EXPERIMENTAL ANALYSIS OF MULTIPHASE FLOWS. DESIGN AND SETUP OF AN EXPERIMENTAL FACILITY

Paolo Juan Sassi Arobba

UNIVERSITAT
ROVIRA i VIRGILI

Experimental analysis of multiphase flows

Design and setup of an experimental facility

Doctoral Thesis

Paolo Sassi Arobba

DOCTORAL THESIS 2021

UNIVERSITAT ROVIRA I VIRGILI
EXPERIMENTAL ANALYSIS OF MULTIPHASE FLOWS. DESIGN AND SETUP OF AN EXPERIMENTAL FACILITY
Paolo Juan Sassi Arobba

UNIVERSITAT ROVIRA I VIRGILI
EXPERIMENTAL ANALYSIS OF MULTIPHASE FLOWS. DESIGN AND SETUP OF AN EXPERIMENTAL FACILITY
Paolo Juan Sassi Arobba

UNIVERSITAT ROVIRA I VIRGILI
EXPERIMENTAL ANALYSIS OF MULTIPHASE FLOWS. DESIGN AND SETUP OF AN EXPERIMENTAL FACILITY
Paolo Juan Sassi Arobba

Paolo Sassi Arobba

Experimental analysis of multiphase flows

Design and setup of an experimental facility

Doctoral Thesis

Supervised by:

Dr. Jordi Pallarès Curto

Dr. Youssef Stiriba

UNIVERSITAT ROVIRA i VIRGILI

Department of Mechanical Engineering

Tarragona – Spain
March 2021

UNIVERSITAT ROVIRA I VIRGILI
EXPERIMENTAL ANALYSIS OF MULTIPHASE FLOWS. DESIGN AND SETUP OF AN EXPERIMENTAL FACILITY
Paolo Juan Sassi Arobba

MEMBERS OF THE THESIS COMMITTEE

President: Ph.D. Prof. Josep Anton Ferré Vidal

Secretary: Ph.D. Prof Mariana Mendina

Chair: Ph.D. Prof. Mouldi Ben Meftah

Tarragona – Spain
March 2021

UNIVERSITAT ROVIRA I VIRGILI
EXPERIMENTAL ANALYSIS OF MULTIPHASE FLOWS. DESIGN AND SETUP OF AN EXPERIMENTAL FACILITY
Paolo Juan Sassi Arobba

UNIVERSITAT
ROVIRA i VIRGILI

Dr. Jordi Pallarès Curto and Dr. Youssef Stiriba, Professors of the Department of Mechanical Engineering of Universitat Rovira i Virgili,

CERTIFY:

That the present study, entitled:

Experimental analysis of multiphase flows. Design and setup of an experimental facility

presented by Paolo Sassi Arobba for the award of the degree of Doctor, has been carried out under our supervision at the Department of Mechanical Engineering of this university and that it fulfils all the requirements to be eligible for the Onternational Distinction Award.

And, to inform you of that and in order for it to have the needed effects, we sign this certification.

Dr. Jordi Pallarès Curto

Dr. Youssef Stiriba

Department of Mechanical Engineering
Escola Tècnica Superior d'Enginyeria Química

Tarragona – Spain
March 2021

A María

Aknowledgements

First of all, I would like to thank Prof. Jordi Pallarès and Prof. Youssef Stiriba, not only for accepting to foster and guide my research, but also for encouraging me to accomplish my Doctoral degree and for introducing me in the field of multiphase flows. I also extend my gratitude to the European Union's Horizon 2020 research and innovation programme under the Marie Skłodowska-Curie grant and the Universitat Rovira i Virgili for all the confidence that they placed in me when they granted me a scholarship. I appreciate the continuous and relentless support that Maria, my family and loved ones have given me along the way, which helped me to stay focused on achieving my goal.

Throughout this research process, I had the great fortune of having shared conversations with very good professors who provided me the necessary tools to tackle the issues addressed in this thesis. I am deeply indebted to all the members of the ECoMMFiT for being always eager to answer my questions and more importantly to discuss the results; to Jordi Iglesias for his vital assistance and hard work on the construction of the experimental facility; and to Sylvana, Alex and Lluis for all those coffee breaks that are so important to recharge and stay focused on the long-term goal. I am also very grateful to the researchers form the department of fluid dynamics at HZDR for opening their doors and including me in the research group, that helped me through the six months to expand my horizons as fluid dynamics engineering.

I would also like to highlight the enormous effort of the coordinators of the doctoral programme on Nanoscience, Materials and Chemical Engineering, and especially to Nuria for always being willing to answer my questions. In like manner, I am very grateful to all the support from the administration team of the URV.

I met numerous fellow students with whom I had the privilege of sharing hours of study and research, and who shaped my understanding of the matter

to no lesser extent than the bibliography or the formal academic training. And, last but not least, I would like to acknowledge the fertile environment of the Department of Mechanical Engineering from URV, in which the constructive atmosphere of cooperation imbues professors, staff and students in the same enthusiastic way.

A process cannot be understood
by stopping it. Understanding
must move with the flow of the
process, must join it and flow
with it.

Frank Herbert

ABSTRACT

The dynamics of three-phase flows involve phenomena of high complexity, whose characterization is of great interest to different sectors of the industry worldwide. A deep understanding and an enhanced prediction capacity of fluid dynamics in multi-phase flow systems is crucial for the design and construction of facilities meant for a wide range of industries. Numerical studies are a very useful tool to assist in the design process for facilities that involve the flow of fluids through pipes. But, in order to obtain reliable models and truly predictable results it is necessary to validate purely numerical models with actual experimental trials in the lab, since they are an essential and very helpful tool for a more thorough understanding of the dynamics and interactions of the different phases involved.

This works presents the design and set up of LESLIE, a low pressure multiphase flow loop for the experimental analysis of two and three-phase flows through pipelines and their accessories. It is designed to measure key parameters, so as to characterise the behaviour of multiphase flows involving gas, liquid and solid phases both in horizontal and vertical pipelines. In this sense, the superficial velocities (or rates) of the individual phases can be properly manipulated so as to reproduce different flow settings in order to measure and characterise (i) the flow regime, (ii) the frictional pressure gradient, (iii) the void fraction (or liquid hold-up); and (iv) the deposition velocity.

New experimental data obtained at LESLIE flow loop is presented in this study for intermittent two and three-phase flows in horizontal pipelines involving air, water and polypropylene pellets of sizes ranging between 1 and 2 millimetres. Flow visualization, pressure and void fraction measurements were performed and are explored in this work for the case of intermittent flows. Furthermore, during a research stay at the Fluid dynamics group of the Helmholtz Zentrum Dresden-Rossendorf (HZDR) in Germany, annular two-phase flows were analysed with image processing techniques from experimental data collected in the lab at the HZDR's facilities.

The influence of solid particles over the frictional pressure drop, flow regime

and slug frequency of a variety of flow settings is analysed and reported in this research work. For two-phase flows, the transition from plug to slug flow matches the ones presented in the flow regime maps in the available literature. However, for three phase flows, a progressive displacement of the transition boundary towards higher gas superficial velocities is consistently found as the solid concentration is increased. Also, the effect of the solid phase over the slug frequency is analysed with visualization techniques. Image processing is then used to determine the slug frequency of the different settings, where a decrease on the slug frequency is found when increasing solid concentrations. Finally, size distributions of the droplets travelling in the core of annular flows have also been measured with image processing techniques. Results are presented and discussed for horizontal pipelines in the presence of accessories.

Frictional pressure gradients (FPG) were calculated for intermittent flows at LESLIE flow loop. The Lockhart-Martinelli correlation was successful in predicting the two-phase FPG. A modified Lockhart-Martinelli correlation was tested then for predicting frictional pressure gradient of three-phase flows with concentrations of 5 and 10 % of polypropylene particles (less dense than the liquid phase). There is no great impact on the FPG, which is consistent with the theory, which indicates that to obtain significant increases in the gradient it is necessary to use concentrations in the order of 30 %.

As a final consideration, it is expected that the data presented in this work will also serve to contrast and validate numerical models.

Keywords:
Multiphase flows, Gas, liquid and solid mixtures, Experimental analysis, Experimental facility setup, Horizontal pipelines.

RESUMEN

La dinámica de los flujos trifásicos implica fenómenos de alta complejidad, tanto en lo que refiere a la cuantificación de variables como a su interpretación conceptual y matemática. Una mejor comprensión y caracterización de esos fenómenos, así como un incremento en la capacidad de predicción de su dinámica, son cruciales para el diseño y montaje de instalaciones que resultan de interés para una amplia gama de industrias. Los estudios numéricos son una herramienta muy útil para ayudar en el proceso de diseño de instalaciones que involucren el flujo de fluidos a través de tuberías. Pero para obtener modelos confiables y resultados verdaderamente predecibles es necesario validar estos modelos puramente numéricos con ensayos experimentales reales realizados en laboratorio, ya que son una herramienta esencial y muy útil para comprender en mayor detalle la dinámica e interacciones de las diferentes fases involucradas en un contexto material.

Este trabajo de investigación presenta el diseño y montaje de LESLIE, un circuito cerrado de baja presión destinado a la reproducción, ensayo e investigación experimental de la dinámica de flujos bifásicos y trifásicos a través de tuberías y sus accesorios. LESLIE está concebido con la intención de obtener medidas de parámetros clave y caracterizar flujos multifásicos con fases gaseosas, líquidas y sólidas, tanto en tuberías horizontales como verticales. En este sentido, las velocidades superficiales de las fases individuales pueden manipularse adecuadamente para reproducir distintas configuraciones de flujo de tal forma que permita medir y caracterizar (i) el régimen de flujo, (ii) el gradiente de presión de fricción, (iii) la fracción de vacío; y (iv) la velocidad de deposición.

Presentamos en esta tesis nuevos datos experimentales, obtenidos mediante el circuito cerrado LESLIE, para regímenes intermitentes en flujos bifásicos y trifásicos en configuración horizontal usando aire, agua y partículas de polipropileno con tamaños de entre 1 y 2 milímetros. Se han obtenido visualizaciones del flujo, medidas de presión y fracción de vacío para diferentes condiciones de operación de flujos intermitentes. Además, durante una estancia de investigación del autor en el grupo de dinámica de fluidos del Helmholtz

Zentrum Dresden-Rossendorf (HZDR) en Alemania, se analizaron flujos anulares bifásicos con técnicas de procesamiento de imágenes a partir de datos experimentales recopilados en el laboratorio de las instalaciones del HZDR.

En este trabajo investigamos el impacto de la presencia de partículas sólidas sobre la caída de presión, el régimen de flujo y la frecuencia del "slug". Para los flujos de dos fases, la transición entre regímenes de flujo de "plugz "slugçoincide con los presentados en los mapas de régimen de flujo en la literatura disponible. Sin embargo, para flujos trifásicos, a medida que aumenta la concentración de sólidos se observa un desplazamiento progresivo de esta transición hacia velocidades superficiales de gas más altas. Además, el efecto de la fase sólida sobre la frecuencia de "slug"se analiza con técnicas de visualización usando captura de imágenes con cámaras de alta velocidad. Luego, el procesamiento de esas imágenes se utiliza para determinar la frecuencia de slug de las diferentes configuraciones, donde se encuentra una disminución en la frecuencia de slug al aumentar las concentraciones de sólidos. Asimismo, el análisis del comportamiento de flujos bifásicos anulares mediante técnicas de procesado de imágenes ha permitido obtener resultados sobre la distribución del tamaño de las gotas, las cuales también se presentan en este trabajo.

Se han calculado los gradientes de presión por fricción para los flujos intermitentes en el circuito cerrado de flujo LESLIE. La correlación Lockhart-Martinelli se aplicó con éxito en la predicción del gradiente de dos fases. Se probó entonces, una correlación Lockhart-Martinelli modificada para predecir el gradiente de presión por fricción de flujos trifásicos con concentraciones de 5 % y 10 % de partículas de polipropileno (menos densas que la fase líquida). No se observó un gran impacto en los gradientes, un resultado consistente con la teoría, que indica que para obtener incrementos significativos en el gradiente es necesario usar concentraciones del órden de 30 %.

Como consideración final, se espera que los datos presentados en este trabajo de investigación también sirvan para contrastar y validar modelos numéricos en estudios futuros.

Palabras claves:
Flujos multifase, Mezclas de gas-líquido-sólido, Análisis experimental, Montaje de instalación experimental, Tuberías horizontales.

Research stay mobility programme

Helmhotz Zentrum Dresden Rossendorf - Dresden, Germany

24^{th} September 2019 to 12^{th} March 2020

Advisor: Dr. Dirk Lucas

Generation of validation data for the modeling of disperse two-phase flows in Computational Fluid Dynamics. Development of computational algorithms, based on image processing techniques, to determine droplet size distribution of annular flows in presence of different accessories in the pipeline.

List of Publications and Conferences

Publications in Journals

Sassi, P., Pallarès, J. & Stiriba, Y. Visualization and measurement of two-phase flows in horizontal pipelines. Exp. Comput. Multiph. Flow 2, 41–51 (2020). https://doi.org/10.1007/s42757-019-0022-1

Paolo Sassi, Youssef Stiriba, Julia Lobera, Virginia Palero & Jordi Pallarès. Experimental Analysis of Gas–Liquid–Solid Three-Phase Flows in Horizontal Pipelines. Flow Turbulence Combust 105, 1035–1054 (2020). https://doi.org/10.1007/s10494-020-00141-1

Contribution to Conferences

Sassi, P., Pallarès, J. & Stiriba, Y. Frictional pressure drop of three-phase flows in horizontal pipelines. Multiphase Flow Conference, Dresden, Germany, November 13 – 16, 2018

Sassi, P., Pallarès, J. & Stiriba, Y. Experimental analysis of three-phase flows in horizontal pipelines, the effect of solid phase on flow regime. International Conference on Multiphase Flows, Rio de Janeiro, Brazil, May 19 – 24, 2019

Sassi, P., Pallarès, J. & Stiriba, Y. Experimental analysis of three-phase flows in horizontal pipelines. Spanish Workshop on Fluid Mechanics, Granada,

July 22 – 23, 2019

Sassi, P., Pallarès, J. & Stiriba, Y. On the plug to slug transition in gas-liquid-solid three-phase flows. Beijing, China, March 4 – 6, 2021, postoned to March 2 – 5, 2021.

List of figures

List of tables

List of variables

List of the relevant variables

A	Cross sectional area $[m^2]$
C_{max}	Maximum packing density [-]
C	Concentration [-]
Q	Volumetric flow rate $[m^3/s]$
G	Mass flow rate $[kg/s]$
P	Pressure $[Pa]$
Re	Reynolds number $Re = U \cdot D/\nu$ [-]
St	Strouhal number $St = f \cdot D/U$ [-]
T	Temperature $[C]$
U	Velocity $[m/s]$
X	Lockhart-Martinelli parameter [-]
f	Frequency $[Hz]$
f	Darcy friction factor [-]
g	Acceleration of gravity $[m/s^2]$
D	Internal diameter $[m]$
j	Superficial velocity $[m/s]$
z	Axial coordinate of the pipeline $[m]$

List of Greek symbols

List of the relevant Greek symbols

Φ	L-M multiphase multiplier
α	Void fraction
∂	Derivarive
λ	Input fraction
μ	Dynamic viscosity $[Pa \cdot s]$
ν	Kinematic viscosity $[m^2/s]$
ρ	Density
τ	Stress tensor

List of sub-indices

List of the relevant subscripts

atm	Atmospheric conditions
b	Bubble
g	Gas phase indicator
f	Liquid phase indicator
lp	Liquid pocket
M	Mixture indicator
mod	Modified
S	Slug unit
s	Solid phase indicator
std	Standard conditions
TS	Test section

List of acronyms

List of Acronyms

ESD equivalent sphere diameter xxxv, 30, 34

FPG frictional pressure gradient xxxv, 6, 9, 47, 48, 53, 54, 91, 92, 100

FPS frames per second xxxv, 15

GL gas-liquid xxxv, 3, 4, 5, 63, 91

GLS gas-liquid-solid xxxv, 2, 3, 4, 5, 92

HZDR Helmholtz Zentrum Dresden Rossendorf xxxv, 6, 17

ID internal diameter xxxv, 10, 13, 30, 39

LESLIE Low prESsure muLtIphasE xxxv, 5, 6, 9, 17, 55, 91, 97

LM Lockhart-Martinelli xxxv

LS liquid-solid xxxv

MSE mean squared error xxxv, 80

SCFM standard cubic feet per minute xxxv, 10

TSI time series image xxxv, 72, 74, 75

UdelaR Universidad de la República xxxv

VFD variable frequency drive xxxv, 11, 12

VMD volume median diameter xxxv, 33

psi pound per squared inch xxxv, 13

Table of contents

Chapter 1

Introduction

1.1. Motivation

Multiphase flows can be defined as any kind of flow that involves relative motion of different fluids delimited by an interface. This comprises a wide spectrum of flows, e.g. liquid-liquid immiscible flows, gas-liquid, gas-solid and liquid-solid are some examples of two-phase flows and the spectrum gets wider when more phases are involved.

The analysis and characterisation of multiphase flows travelling in pipes are vital for some sectors of the industry worldwide, specially the oil, nuclear and chemical industries. In order to cater for those needs, numerous authors have studied multiphase flows from different angles. A complete analysis of multiphase flows can be addressed by formulating a set of conservation equations for each fluid, governing the momentum, energy and mass balance eqs. (1.1) to (1.3) respectively. Where k stands for the phase number, α_k is the fraction of phase k, ρ is the density, U the velocity, P the pressure, δ the perimeter, τ the stress tensor, g the gravity field, E the energy and q is the heat.

$$\frac{\partial\left(\alpha_k\rho_k U_k^i\right)}{\partial t}+\frac{\partial\left(\rho_k\alpha_k U_k^j U_k^i\right)}{\partial x^j}=-\alpha_k\frac{\partial P}{\partial x^i}-\frac{\partial\left(\alpha_k\tau_k^{ij}\right)}{\partial x^j}+\alpha_k\rho_k g^i+D_k^i \tag{1.1}$$

$$\frac{\partial(\alpha_k\rho_k E_k)}{\partial t}=-\alpha_k\frac{\partial}{\partial x^j}\left(\rho_k U_k^j E_k+q_k^j+\left(\tau_k^{ij}+P\delta_k^{ij}\right)U_k^i\right)+\alpha_k\rho_k g^i U_k^i \tag{1.2}$$

$$\frac{\partial\left(\alpha_k\rho_k\right)}{\partial t}+\frac{\partial\left(\alpha_k\rho_k U_k^i\right)}{\partial x^i}=0 \tag{1.3}$$

However, the determination of the interfacial interaction term, D_k^i in the momentum equation, is considerably difficult due to the uncertainties of the interaction between the phases themselves and also due to the complexities of the mathematical methods involved.

Even more challenging difficulties are added to the problem described above by including solids in gas-liquid flow. The interfacial interaction term (eq. (1.1)) should also include more interfacial forces (e.g. drag, turbulent dispersion, lift, wall lubrication, virtual mass and solid particle collisions). Due to the great difficulties involved in calculating all these interactions, these types of flows have been approached with models that intend to simplify the equations. Numerical studies are often a very useful tool to assist in the design process Akhlaghi et al. [2019], Pineda-Pérez et al. [2018]. But it is well known that in order to obtain reliable results it is necessary to validate the purely numerical models with actual experimental trials in the lab, since they are an essential and very helpful tool so as to thoroughly understand the dynamics and interaction of the different phases involved.

So far, the study of multiphase flows has been mainly focused on gas-liquid two-phase flows, which have been the subject of numerous studies, mostly related to the oil and chemical industries for almost a century. However, gas-liquid-solid (GLS) three-phase flows, which can also be found in these production fields, have not been studied as extensively as two-phase flows, and so there are outstanding questions to be addressed on the field. Although some authors have already studied GLS mixtures, most available literature on GLS flows focuses on the transport of solids, without further analysis on the influence of solids on flow dynamics, despite the fact that three-phase flows are present in a wide range of industrial processes, from the production stages of oil and gas Bello et al. [2005], where fragments of sand or rock are often present in the pipes, to the different phases of refinement and production of petroleum products. GLS flows are also involved, among many other processes, in the transport of biomass Miao et al. [2013], in chemical reactors Scott and Rao [1971], nuclear waste decommissioning Mao et al. [1997], pulp and paper production, and in many applications that involved air injections Orell [2007]. Furthermore, many products on the chemical industry are comprised of solid particles that will eventually be formed from chemical reactions involving gas and liquid phases, where GLS phases coexist along the process.

Comprehensive understanding of multiphase flows is important not only in

terms of their respective applications in the industry, but also because of the influence that these regimes have on the structural integrity of the materials involved. For instance, the constant presence of intermittent flows can be destructive in the long term, due to the impact that it exerts on the momentum and frictional pressure gradient, especially for long piping systems, where flow rates can fluctuate significantly both in space and time. Moreover, the slug frequency (the number of slug unit cells that pass through a specific cross section in the pipe per time unit), which can also vary for different settings, could eventually lead to resonance problems Thaker and Banerjee [2016].

When dealing with annular flows, such as the ones that can be found in cooling systems, the presence of the liquid film in the pipeline wall is crucial to keep it cooled. High heat rates can lead to "dryout" (Silvi et al. [2020]), a term commonly used to define the condition of zero liquid film. In those cases, due to the evaporation of the liquid phase, the heat transfer is significantly reduced, and therefore the absence of cooling, allows the pipeline to reach very high temperatures that may damage its composing materials. On the other hand, the dispersed drops that travel in the core of the pipeline move at very high velocities. The size and velocity of drops and solid particles (when applicable) can significantly influence erosion and corrosion, especially in the presence of accessories and joints in the pipeline (e.g. elbows, bends, valves, orifices and expansions). Thus, it is essential to relay on methodologically sound conceptual tools in order to properly design multiphase flows facilities, an ever growing area in which there is still plenty of room for improvement.

A deep understanding and prediction of fluid dynamics in multi-phase flow systems is crucial for the design and construction of facilities meant for those industries. The key parameters for facility design of processes comprising gas-liquid (GL) or GLS mixture flows are:

- *Frictional pressure gradient,* which allows to make predictions of power consumption during operation.
- *Flow regime,* the spatial distribution of the phases over the pipe volume, which is important to establish precisely, because specific regimes may be necessary for different processes.
- *Void fraction,* which together with the regime determines the interfacial area concentration.
- *Deposition velocity,* is the minimum operational velocity required to

avoid accumulation of particles at the bottom of the pipeline, which may eventually result in obstructions.

In general, these are governed by more basic characteristics such as the physical properties of fluids and solids Bhagwat and Ghajar [2014], flow orientation Lu et al. [2018], superficial velocities and slippage Kong et al. [2018]. Superficial velocity is the mean velocity that a single phase would have if only one and the same flow rate travelled along the pipe. The slippage, refers to the relative motion between two or more phases. In section 1.1 a simplified scheme of a three-phase flow inside an horizontal pipeline is presented.

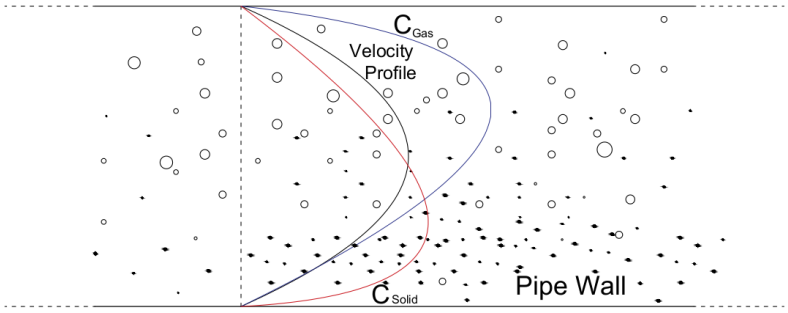

Figure 1.1: Scheme of three-phase flow

Considering a cross section of the pipe (black dashed line in section 1.1), the black curve represents a typical symmetric velocity profile of a liquid flowing in a pipeline. However, when gas and solid phases are also present, the gravitational forces produce non symmetric concentration profiles. In this sense, the blue line corresponds to the concentration of the gas phase, which due to its buoyancy is more concentrated in the top of the pipe. The red line represents the concentration profile of the solid phase, that, if the solid density is larger than the liquid density (as in section 1.1), higher concentration would be found in the bottom of the pipe, where it accumulates due to gravitational forces.

Enclosed in this study there is a description of an experimental facility, that was especially designed and implemented to run experiments on measured performances of two GL and three-phase GLS flows, where air, water and polypropylene pellets were used as gas, liquid and solid phases, respectively. Flow characterization arising from such experiments is then presented in this study, as well as the measured influence of solid phases on the most relevant parameters of multiphase flows.

1.2. Aims and objectives

The main objective of this work is to study in a reliable way the main design parameters listed in the previous section, in order to provide design support and conceptual tools to work with three-phase flows. In order to achieve those objectives, the process entails the design and construction of an experimental facility that allows both visual, and mathematical analysis of the behavior of multiphase flows as they move along pipelines, measuring the interaction of air, water and solid particles as working fluids. The facility will be used to study the different capabilities of three phase flows, evaluating the results obtained under each set of variables and comparing them, as far as possible, with results obtained by other researchers.

The repeated use of the experimental rig, under a variety of conditions, will seek to identify the extent to which the key parameters are affected by including solid particles in GL two-phase flows, which have already been extensively studied, and to what measure two phase flow studies can be safely extrapolated when applied to three phase conditions.

Finally, the spectrum of results is expected to generate a wealth of reliable experimental data that will serve as validation for testing and benchmark reference for numerical models, as well as to be compared to other measurement techniques.

1.3. Research flow

In this study a Low prESsure muLtIphasE (LESLIE) flow loop is introduced. An experimental facility for the analysis of GL and GLS mixtures in horizontal and vertical pipelines and accessories. During the three years of the PhD, the facility has been designed and built. It has also been used to obtain experimental data data on different phenomena with different characteristics, with the intention of testing all the elements that the installation has, leaving room for further study of the matter.

This research will be presented in seven chapters in which multiphase flows are covered. The design a construction of LESLIE is included, together with experimental data obtained at the facility and its analysis. Some of the previous works of other authors, that are consider relevant are referenced, including measuring techniques, and correlations to predict key parameters

of multiphase flows. Also, a section dedicated to annular two-phase flows is included. It corresponds to the studies performed during a research stay at Helmholtz Zentrum Dresden Rossendorf (HZDR), Germany.

A brief description of every chapter is given here:

- Chapter 1. Lists the motivations for studying multiphase flows, including the difficulties faced by the subject. Outlines the purpose of the research with the main applications and why it is important to overcome the adversities. Finally, accounts for the objectives of the research.
- Chapter 2. Introduces LESLIE flow loop. The experimental facility that has been designed and construction in the first stage of the research. The fluids involved, the instrumentation and test sections are fully described.
- Chapter 3. Presents detailed characterization from visual techniques of intermittent two and three-phase flows the effect of the solid particles on the transition from plug to slug flow is reported. Also, droplet size measurements of annular two-phase flows are presented, with a brief description of the facility and measuring technique used for its analysis during the research stay at HZDR.
- Chapter 4. This chapter introduce some of the available correlations to predict the frictional pressure gradient (FPG) on two and three-phase flows. These are then tested and compared against experimental data collected at LESLIE flow loop. The influence of the solid phase is evaluated, and a modified correlation for predicting the FPG of three-phase flows is tested.
- Chapter 5. Here, measurements of void fraction for plug and slug two-phase flows are presented and compared with correlations from the literature.
- Chapter 6. Fully describes the analysis of slug frequency in intermittent flows. Measurements are compared both for two and three-phase flows.
- Chapter 7. The final chapter contains the conclusions reached in the research process and suggest some directions for further studies with LESLIE flow loop.
- Appendix A. The experimental campaigns are detailed, where summaries of the experimental data are presented.
- Appendiz B. The image processing algorithm for determining the droplet size distribution in annular flows is fully described.

1.4. Bibliography

Mohammad Akhlaghi, Vahid Mohammadi, Nowrouz Mohammad Nouri, Morteza Taherkhani, and Mehdi Karimi. Multi-Fluid VoF model assessment to simulate the horizontal air–water intermittent flow. *Chemical Engineering Research and Design*, 152:48–59, 2019. ISSN 02638762. doi: 10.1016/j.cherd.2019.09.031. URL https://doi.org/10.1016/j.cherd.2019.09.031.

H. Pineda-Pérez, T. Kim, E. Pereyra, and N. Ratkovich. CFD modeling of air and highly viscous liquid two-phase slug flow in horizontal pipes. *Chemical Engineering Research and Design*, 136:638–653, 2018. ISSN 02638762. doi: 10.1016/j.cherd.2018.06.023. URL https://doi.org/10.1016/j.cherd.2018.06.023.

Oladele O. Bello, Kurt M. Reinicke, and Catalin Teodoriu. Particle holdup profiles in horizontal gas-liquid-solid multiphase flow pipeline. *Chemical Engineering and Technology*, 28(12):1546–1553, 2005. ISSN 09307516. doi: 10.1002/ceat.200500195.

Zewei Miao, Tony E Grift, Alan C Hansen, and KC Ting. An overview of lignocellulosic biomass feedstock harvest, processing and supply for biofuel production. *Biofuels*, 4(1):5–8, 2013. ISSN 1759-7269. doi: 10.4155/bfs.12.76. URL https://www.tandfonline.com/doi/full/10.4155/bfs.12.76.

D. S. Scott and P. K. Rao. Transport of Solids by Gas-Liquid Mixtures in Horizontal Pipes. *Canadian Journal of Chemical Engineering*, 49:302–309, 1971. ISSN 0722-1819.

F. Mao, F. K. Desir, and M. A. Ebadian. Pressure drop measurment and correlation for three-phase flow of simulated nuclear waste in a horizontal pipe. *International Journal of Multiphase Flow*, 23(2):397–402, 1997.

Aluf Orell. The effect of gas injection on the hydraulic transport of slurries in horizontal pipes. *Chemical Engineering Science*, 62(23):6659–6676, 2007. ISSN 00092509. doi: 10.1016/j.ces.2007.07.067.

Jignesh Thaker and Jyotirmay Banerjee. On intermittent flow characteristics of gas–liquid two-phase flow. *Nuclear Engineering and Design*, 310:363–377, 2016. ISSN 00295493. doi: 10.1016/j.nucengdes.2016.10.020. URL http://dx.doi.org/10.1016/j.nucengdes.2016.10.020.

Liril D. Silvi, Avik Saha, Dinesh K. Chandraker, Sumana Ghosh, and Arup K. Das. Numerical analysis of pre-dryout sequences through the route of interfacial evolution in annular gas-liquid two-phase flow with phase change. *Chemical Engineering Science*, 212:115356, 2020. ISSN 00092509. doi: 10.1016/j.ces.2019.115356. URL https://doi.org/10.1016/j.ces.2019.115356.

Swanand M. Bhagwat and Afshin J. Ghajar. A flow pattern independent drift flux model based void fraction correlation for a wide range of gas-liquid two phase flow. *International Journal of Multiphase Flow*, 59:186–205, 2014. ISSN 03019322. doi: 10.1016/j.ijmultiphaseflow.2013.11.001. URL http://dx.doi.org/10.1016/j.ijmultiphaseflow.2013.11.001.

Cihang Lu, Ran Kong, Shouxu Qiao, Joshua Larimer, Seungjin Kim, Stephen Bajorek, Kirk Tien, and Chris Hoxie. Frictional pressure drop analysis for horizontal and vertical air-water two-phase flows in different pipe sizes. *Nuclear Engineering and Design*, 332(September 2017):147–161, 2018. ISSN 00295493. doi: 10.1016/j.nucengdes.2018.03.036. URL https://doi.org/10.1016/j.nucengdes.2018.03.036.

Ran Kong, Qingzi Zhu, Seungjin Kim, Mamoru Ishii, Stephen Bajorek, Kirk Tien, and Chris Hoxie. Void fraction prediction and one-dimensional drift-flux analysis for horizontal two-phase flow in different pipe sizes. *Experimental Thermal and Fluid Science*, 99(May):433–445, 2018. ISSN 08941777. doi: 10.1016/j.expthermflusci.2018.08.019.

Chapter 2

Experimental Facility

An experimental facility, LESLIE flow loop, for the analysis of two and three-phase flows was designed and set up. In order to study the main parameters for design of industrial facilities the following instrumentation is included in LESLIE:

- Transparent pipes with visualization bridges stations, for determination of the flow regimes and flow characterization. Also, allows to determine the deposition velocity.
- Pressure transducers, for the analysis of the FPG. Both differential and absolute transducers are used for horizontal and vertical sections respectively.
- Quick-closing valves with actuators controlled remotely, for the analysis of the void fraction.

LESLIE flow loop was designed and constructed during the year 2018. In January of 2020, the facility was significantly updated, where new instruments and accessories were incorporated. Therefore, some of the measurements reported in this work have been made with different instruments, which will be indicated where appropriate. The facility is schematically represented in fig. 2.1. The flow loop has two horizontal and two vertical pipe sections, including a vertical upwards (V1) and a vertical downwards (V2) test section. It is specifically designed to reproduce intermittent flows regimes (plug and slug flow) in the horizontal test section and bubbly, slug, churn and annular flow regimes in the vertical test sections.

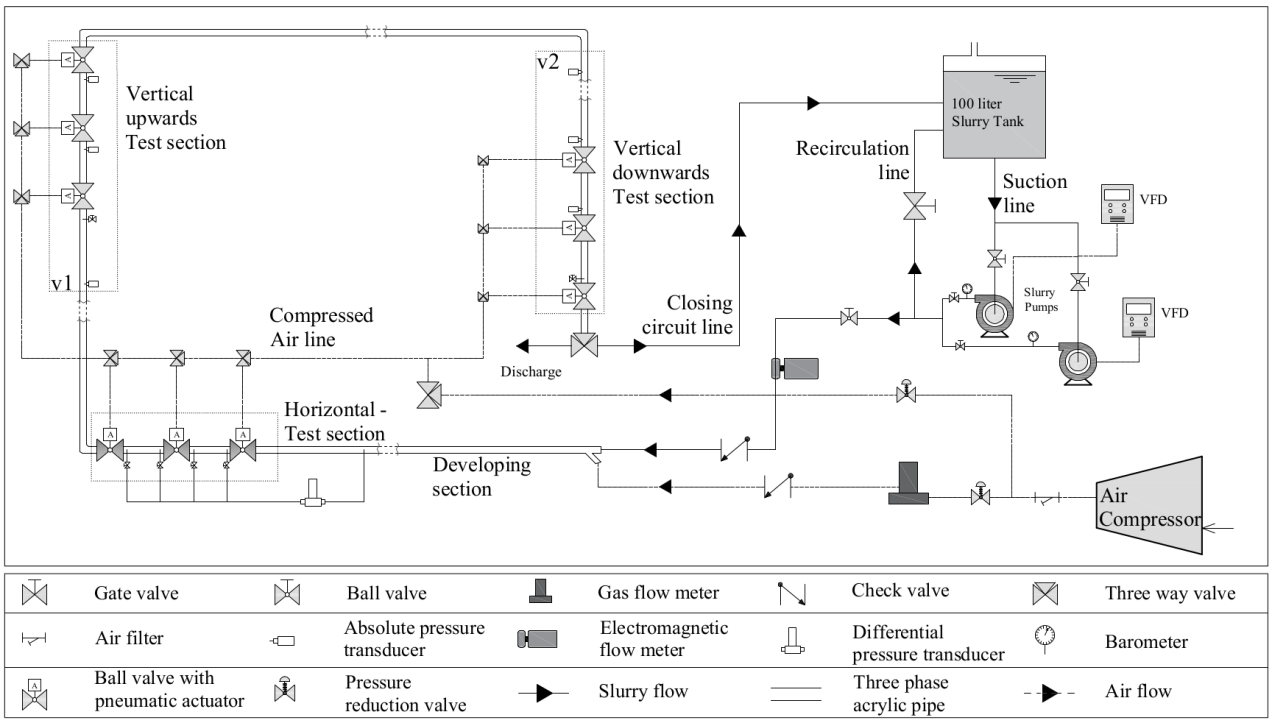

Figure 2.1: Schematic of the updated experimental facility (not to scale).

2.1. Working fluids

2.1.1. Gas phase

The gas phase is compressed air, taken from the lab manifold at a pressure of eight bar, previously filtered and dried. The air flows inside 8 mm internal diameter (ID) plastic pipes.

- *Initial facility:* the flow rate was measured using two Omega rotameters with scales ranging from 0.4 up to 2.0 standard cubic feet per minute (SCFM) and from 1.0 up to 5.0 SCFM with accuracies of 2% and 3% respectively. Where low rates were measured with the low scale rotameter, and high rates with the high scale rotameter. The reading of the rotameters must be corrected by the formula provided by Omega, eq. (2.1), in order to convert the metered flow to an equivalent flow of air in SCFM at 21^{o}C and 14.7 psia.

$$\mathrm{SCFM}_{reading} = \mathrm{SCFM}_{true}\sqrt{\frac{(\mathrm{SG})(T_{rot})(14.7)}{(1.0)(530)(P_{rot})}} \tag{2.1}$$

where SG is the specific gravity of the metered gas as STP, T_{rot} and P_{rot} are the gas temperature in Rankine degrees and pressure in psia at the rotameters respectively. Then, the gas superficial velocity (j_g) is calculated at the test section with the isothermal relation:

$$j_g = \frac{Q_{STD}}{A}\frac{P_{std}}{P_{TS}} \tag{2.2}$$

where Q_{STD} is the flow rate in standard conditions, A the area of the cross section, P_0 the standard atmospheric pressure and P_{TS} the absolute pressure at the test section.

- *Updated facility:* an Omega mass flow controller is used to measure mass air rate. It uses the principle of differential pressure within a laminar flow field to determine and control mass flow rate. It has an accuracy of $\pm$ 0.8 % of the reading and better control over the flow set point. The gas superficial velocity is calculated locally, at the test section, with eq. (2.3), where G_g is the mass flow rate reading, A is the cross section area and ρ_g is the gas density. The latter is calculated using the ideal gas equation in eq. (2.4) with the measured local pressure P and the mixture temperature T (in Kelvin degrees).

$$j_g = \frac{G_g}{\rho_g \cdot A} \tag{2.3}$$

$$\rho_g = \frac{P}{R_{air} \cdot T} \tag{2.4}$$

Then, a one-way check valve is located just before the air is delivered to the test section, to avoid the entrance of water in the air system. After passing through the test section, the mixture is delivered through the closing circuit line, back to the slurry tank where the air is vented to the environment.

2.1.2. Liquid phase

Generic tap water is used as the liquid phase, and it is stored in a 100 litres tank located at 1.2 meters above the ground level.

- *Initial facility:* water was pumped with a 5.5 kW Weir model AB80 centrifugal slurry pump with open impeller. A WEG CFW 500 variable frequency drive (VFD) is used to controll the water pump.

- *Updated facility:* an Ebara 7.5 kW centrifugal pump with a 224 mm (AISI316L) closed impeller was installed in parallel. This water pump allows to reach higher flow rates. In the updated facility it can be choose wich water pump to use.

The main flow is measured with an Isoil MS2500 electromagnetic flow meter with an accuracy of ±0.8%, and then delivered to the test section through the "Y" junction, where the gas and liquid phases get mixed. A secondary flow is recirculated to the slurry tank with two purposes, (i) to ensure the mixing of the slurry inside the tank, and (ii) to be able to measure a wider spectrum of slurry flow rates together with the VFD, which controls the slurry pump.

The main flow, flows through the test section and back to the slurry tank were is recirculated.

2.1.3. Solid phase

The solid phase consists of irregular polypropylene pellets, with density $\rho_s = 866 kg/m^3$. The particle diameters are between 1 and 2 mm according to the sieves used for the diameter separation. fig. 2.2 shows some measurements of the pellets size, it can be noted tha irregularity of the pellets.

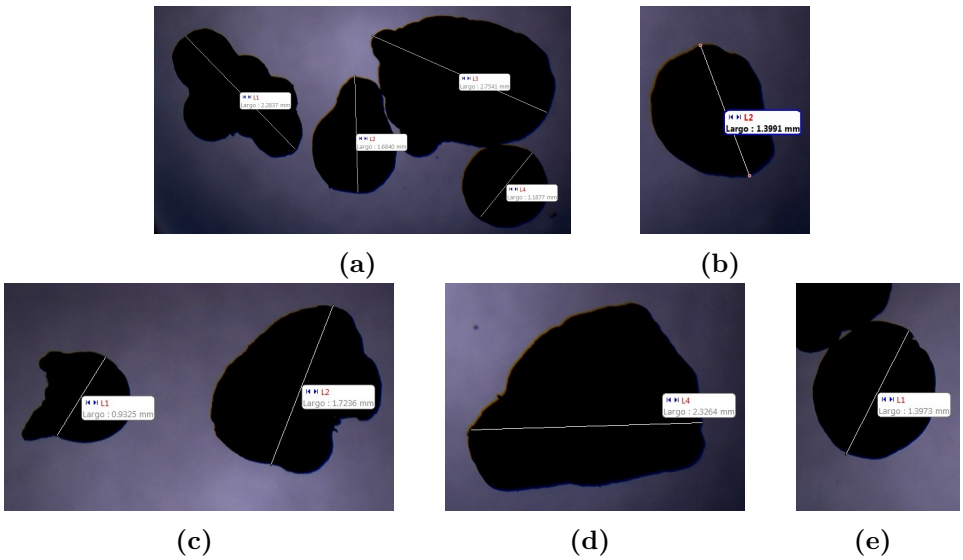

Figure 2.2: Microscopic pictures of the polypropylene pellets.

The pellets are added in the slurry tank with a specific concentration. In order to reach the required volumetric concentration of solids, the measured maximum packing density was calculated and is C_{max}= 0.585.

The slurry mixture is composed of water and the solid particles, and it is homogenized due to the turbulence in the tank. However, as particles float in the water, solid percentage measurements have been made within the test section. For this, the slurry mixture is circulated through the facility and the fast-closing valves (see fig. 2.3) are closed simultaneously. The fractions of liquid and solid phases, trapped in between the valves, are measured. For a mixture of 5% of solid concentrations several measurements were performed for different flow rates and the solid percentage is $5.0 \pm 0.5\%$. For mixtures of 10% the mean value is $10 \pm 1\%$.

2.2. Test sections and instrumentation

2.2.1. Horizontal test section

The three-phase horizontal test section consist of 30 mm ID straight transparent acrylic pipes with a total length of 60 diameters and a previous segment of 110 diameters in order to ensure the complete development of the flow. A more detailed scheme of the horizontal test section is presented in creffig:H1.

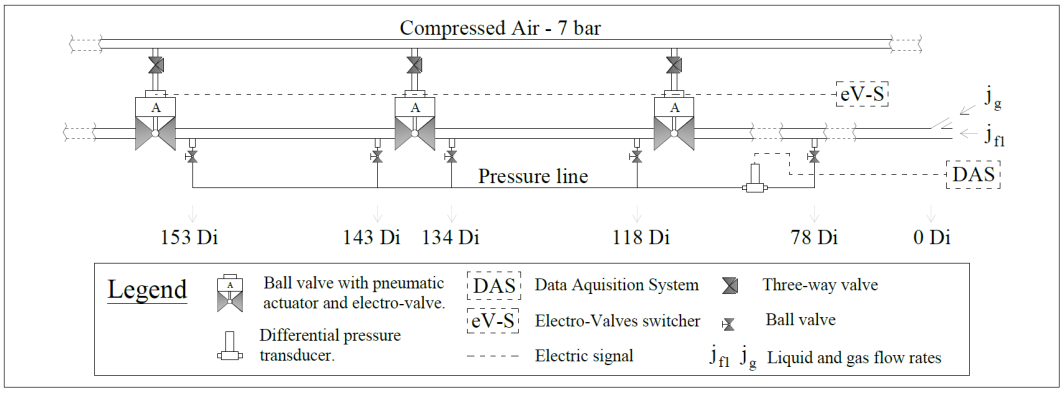

Figure 2.3: Schematic of the horizontal test section (not to scale).

Pressure measurements An Omega differential pressure transducer with a range from 0 to 5 pound per squared inch (psi) (0.345 bar) is connected to the horizontal test section in order to measure the frictional pressure drop. A second differential pressure transducer of 15 psi (1.03 bar) is used to obtain the gauge pressure inside the pipeline, measuring between the atmosphere and the

selected pressure tap. The pressure lines are connected to 5 points of the acrylic pipes, as detailed in fig. 2.3 by coupling an acrylic "bridge" with a threaded hole where a ball valve is placed. Different segments can be measured by selecting the corresponding combination of valves. Caution is important in order to avoid air in the pressure lines, as it would certainly distort the measurements. An Agilent 34970A multiplexor data acquisition system is used to collect the data from the pressure transducers. The multiplexor allows to collect data with a maximum sampling rate of 50 measurements per second.

Temporal pressure fluctuations on intermittent flow regimes are relatively large. In the present study the pressure drop per unit length is calculated by averaging the temporal signal of pressure drop between different test sections. For each test condition the differential pressure is measured during 120 seconds between four different distances, together with the gauge pressure. As an example, fig. 2.4 shows the signals from the pressure transducers of two flow regimes, corresponding to three-phase flows with 10% concentration of solids by volume, at two axial positions, $z/D = 118$ (blue) and $z/D = 153$ (red). The measurements in fig. 2.4a correspond to plug flow, with rms fluctuations of 8%, while the gauge pressure from fig. 2.4b, corresponds to slug flow, with rms fluctuations of 15%. Despite the large fluctuations, specially in slug flows, it can be seen that, for both flow regimes, the signals range around the mean value.

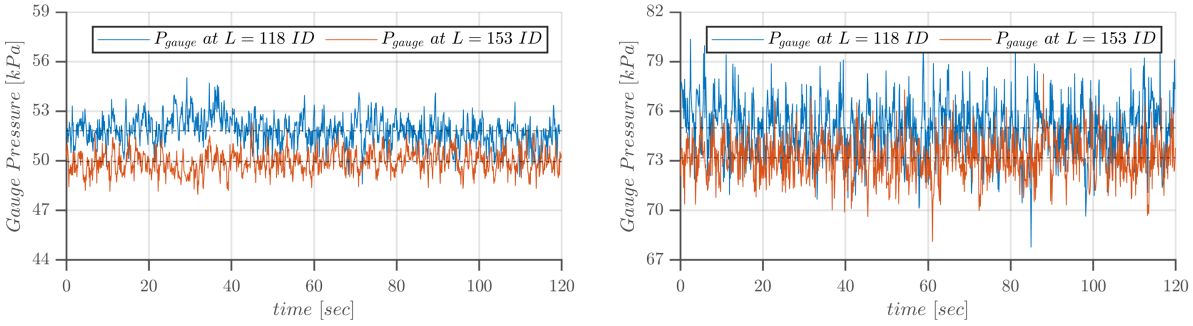

(a) Plug flow, $j_{fs} = 1.70m/s$ and $j_g = 0.43m/s$. **(b)** Slug flow, $j_{fs} = 1.70m/s$ and $j_g = 2.17m/s$.

Figure 2.4: Temporal fluctuations on the gauge pressure measurements for three-phase flow, 10% loading of solids.

Void fraction measurements The hold-up or void fraction is measured by closing simultaneously three quick-closing ball valves with API pneumatic rotary actuators, activated with solenoid valves. The volumetric percentage

of each phase trapped between the valves can be measured several times for the same test condition. The valves are full-opening ball valves, with ID equal to the pipe ID, so that the flow is not disturbed by the valves. A secondary facility provides compressed air at 7 bar to the pneumatic rotary actuators, being capable to fully close the valves simultaneously in 120 ms.

Flow visualization The flow visualization is performed with a Photron Mini UX100 fast camera. Images are taken at 3200 frames per second (FPS) and two lenses are used. A 50 mm lens is used for wide images to capture the large scale characteristics of the flow. A 22 mm lens is used for capturing closer images in order to identify smaller scale attributes. Backlight illumination is used with led lights and a white diffusive screen in order to homogenize the light in the focus plane. Two acrylic bridges with glycerin are used to counteract the distortion effect due to the curved pipe walls. fig. 2.5 shows the arrangements for the image acquisition together with a detailed scheme of the pressure taps.

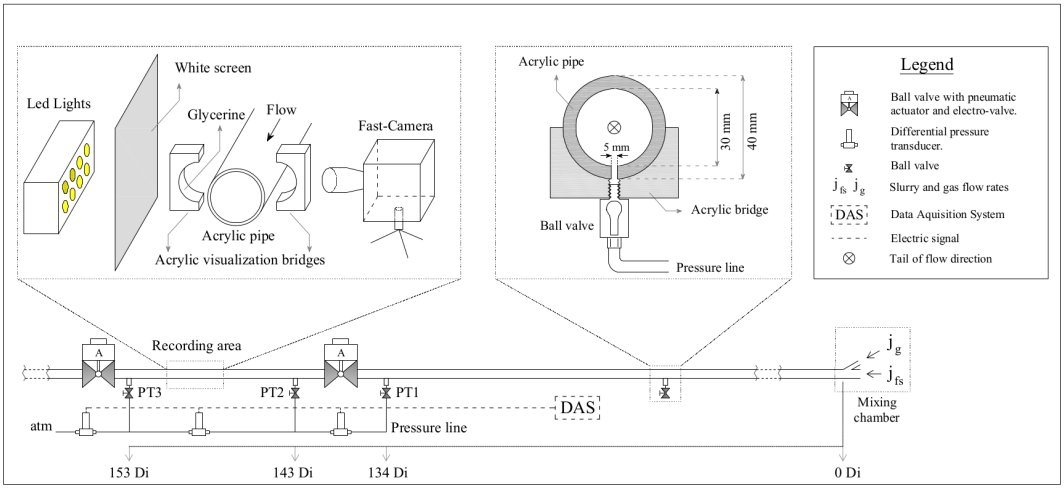

Figure 2.5: Schematic of the horizontal test section, with details (not to scale).

2.2.2. Vertical test sections

The vertical test section also consist of transparent plexiglass pipes, with a developing section of 2 meters. The pressure is measured in three points with absolute pressure transducers with a range from 0 to 60 psi, which are installed with care not to disturb the flow, but not to accumulate air between the fluid

and the transducer. It is not possible to use differential pressure transducers in the vertical test sections, because of the presence of air in the pressure lines.

V1 and V2 are also equiped with three quick-closing ball valves with pneumatic rotary actuator in each test section, in order to measure the hold-up or void fraction.

The elbows used between the horizontal and vertical sections were designed to avoid major distortions on the flow. These are also made of transparent plexiglass to visualize the flow in the inside. In fig. 2.6 an axial plane of the elbows and their dimensions are shown.

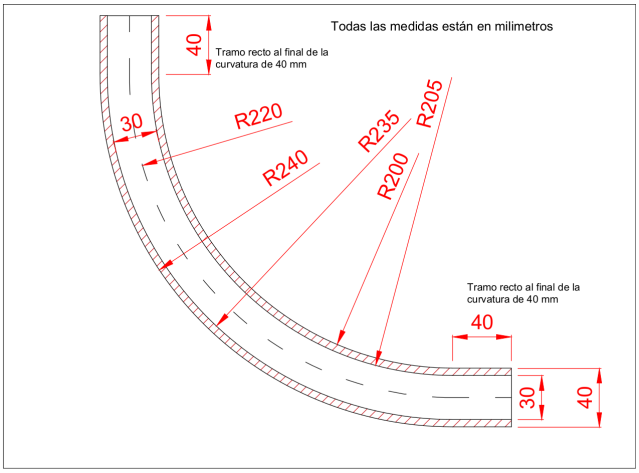

Figure 2.6: Axial plane of the elbows.

Chapter 3

Flow visualization

In this chapter two and three-phase flows are characterized with visualization techniques. In section section 3.1, images of two and three phase intermittent flows obtained at LESLIE flow loop are presented. As the pipes in LESLIE are made of transparent plexiglass, it is possible to capture images from the outside with the configuration presented in chapter 2.

In 3.2, two-phase annular flows are analysed, which cannot be reproduced in LESLIE (due to not having sufficient air flow rates as required). Even if it is possible to reproduce them, given their topology, the images from the outside would not be useful to characterize this type of flows for reasons that will be discussed in the corresponding section. With that said, the results obtained from annular flows correspond to the work carried out during the research stay at HZDR. There, image processing techniques were used to characterize these types of flows. The images were obtained in a two-phase flow loop in the facilities of HZDR, which is briefly introduced in section 3.2.2.

Finally in section section 3.3 the flow regimes are analysed in a flow regimen map. In particular, the effect of adding solid particles and how it affects the transition from plug to slug is studied.

3.1. Intermittent flows

Intermittent two-phase flow regimes, such as plug and slug flows, are characterized by having two clear differentiated structures, which move intermittently within the pipe, both in space and time. These are: (i) a liquid pocket filling the cross section of the pipe, which might contain dispersed

bubbles in the case of slug flows and very few or even none bubbles in plug flows, followed by (ii) an elongated bubble (Taylor bubble) at the top of the pipe travelling over a film of liquid that lays at the bottom. Both structures, considered together, conform the slug unit cell. fig. 3.1 shows schematic slug units both for plug (left) and slug (right) flows.

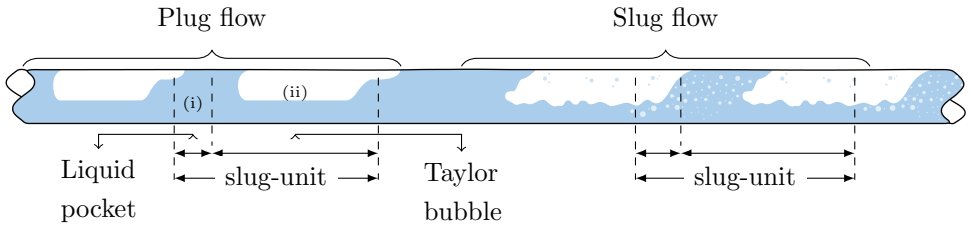

Figure 3.1: Scheme of plug and slug flow regimes

The fast camera is used to visualize the flow inside the pipelines. Recording are used to identify and characterize the flow regimes. Videos are recorded at an axial location of $z/D = 150$ from the inlet to analyse fully developed flow conditions. Videos are taken for several runs within plug, plug-to-slug transition and slug flows in order to identify the transition boundaries.

Three different flow regimes of two-phase flow are presented in fig. 3.2. In fig. 3.2a a plug flow elongated bubble is shown. It can be seen that this flow regime is characterized by elongated gas plugs that move along the top of the pipe, which generally presents a round nose. Gas plugs displace the liquid phase towards the wall of the pipe producing a very thin film of liquid in between. From the figure it can be inferred an important shear force between the two phases, as evidenced by the slight stripes in the thin film, and the waves produced at the bottom of the main body of the plug bubble. Finally, plug bubbles show elongated tails in the very upper portion of the pipe followed by liquid regions with few bubbles that detached from the tail. Some of these observations, among some other characteristics on plug flows, can also be found in Talley et al. [2015].

In fig. 3.2b a plug-to-slug transition bubble is shown. It can be seen how the shear force between the two phases is increased as more stripes are found in the thin film and the bottom interface, which appears more wavy, even producing the detachment of small droplets inside the gas bubble. Also as a result of the increase in the shear force, the tail breaks into smaller bubbles that travel behind.

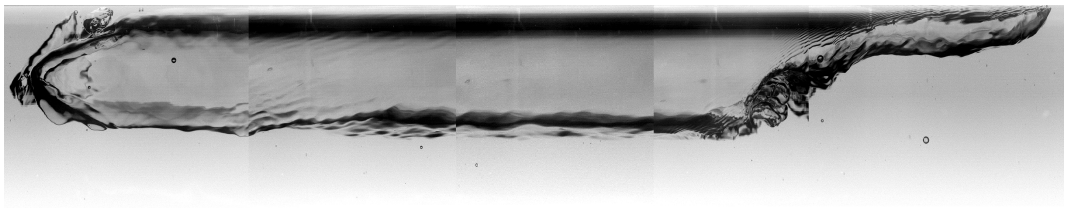

(a) Plug flow elongated bubble; $j_g = 0.40\,m/s$, $j_{fs} = 1.0\,m/s$.

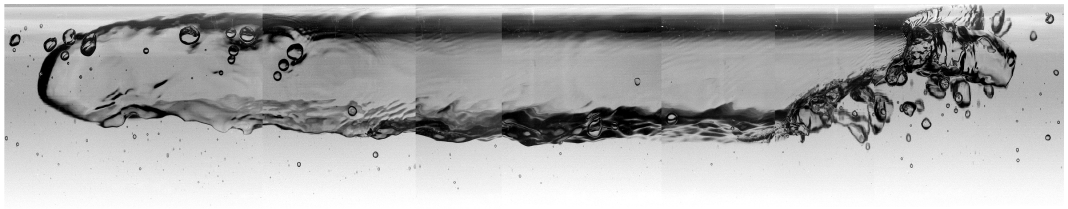

(b) Plug to Slug Transition elongated bubble; $j_g = 1.0\,m/s$, $j_{fs} = 1.0\,m/s$.

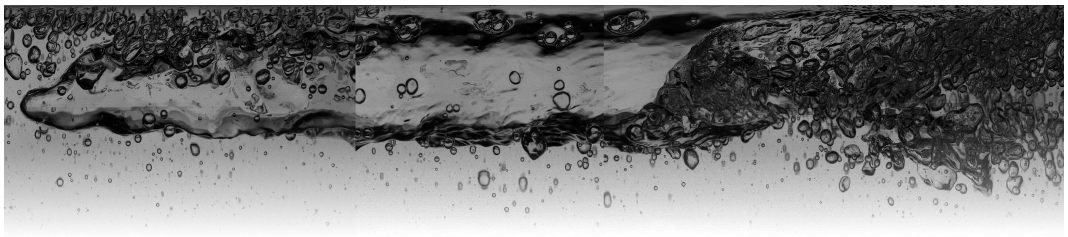

(c) Slug flow elongated bubble; $j_g = 1.0\,m/s$, $j_{fs} = 2.0\,m/s$.

Figure 3.2: Plug, transition and slug flow reconstructed bubbles for two-phase flow (flowing from right to left).

Finally, in slug flows (see fig. 3.2c) the elongated bubbles move forward faster than the liquid phase, and they are followed by bubble clusters. The increase of the relative velocity yields higher shear forces, and consequently, these bubbles show a sharper nose compared with plug bubbles and a chaotic tail with continuous detachment of small bubbles. Following the tail, bubble clusters are spread within the volume of the pipe due to the higher turbulence of the flow that suspends the bubbles in the flow. The presence of the bubble clusters is the main characteristic that distinguish slug from plug flows, as highlighted in Talley et al. [2015]. Because these bubbles are dispersed in a turbulent flow, there is a relative motion between the air bubble and the water. This relative velocity between the phases induces even more turbulence in the liquid phase, specifically in the wake of the bubble. This phenomenon is known as the bubble-induced turbulence. More details on the phenomena

can be found in Rzehak and Krepper [2013]. Further, the existence of a vortex following slug bubbles is observed while in plug flows these are not found. The result is a very large interface between the phases with high turbulence in slug flows. Therefore, this regime is more appropriate for heat and mass transfer applications.

The same identification criterion is used for three-phase flows. In fig. 3.3, three images for three-phase flows with 5 % of solid concentration are shown. fig. 3.3a corresponds to plug flow, fig. 3.3b to plug-to-slug transition, and fig. 3.3c to slug flow.

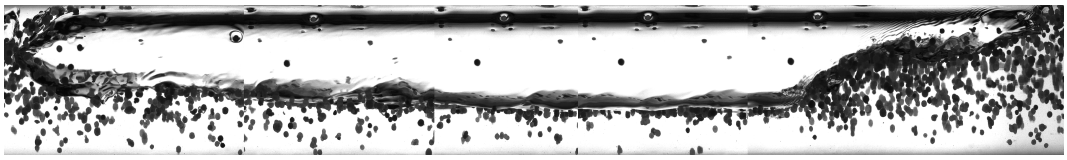

(a) Plug flow elongated bubble; $j_g = 0.40\,m/s$, $j_{fs} = 1.0\,m/s$.

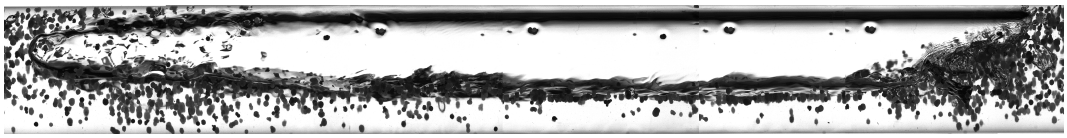

(b) Plug-to-Slug Transition elongated bubble; $j_g = 1.0\,m/s$, $j_{fs} = 1.0\,m/s$.

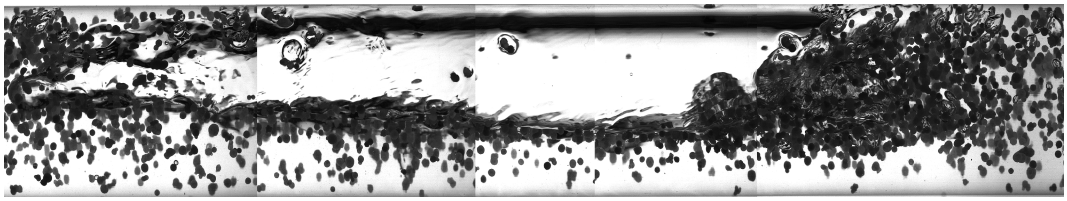

(c) Slug flow elongated bubble; $j_g = 1.0\,m/s$, $j_{fs} = 2.0\,m/s$.

Figure 3.3: Plug, transition and slug flow reconstructed bubbles for three-phase flows with 5 % of solid concentration (flowing from right to left).

Again, the main difference stands in the liquid plugs or slugs between the elongated bubbles. In plug flows there are barely air bubbles between the plug bubbles and mostly there are only solid particles. On the contrary, in slug flows there are many air bubbles among the solid particles. Plug flows also show a higher concentration of particles at the top of the pipeline in comparison to slug flows. This is mainly because of the higher turbulence on the latter flows, with higher transverse velocities, that effectively suspend the solid particles in the core of the liquid phase.

In plug flows, there are large slurry regions between the plug bubbles. However, collision and eventually coalescence of the gas bubbles is observed frequently. Regular plug bubbles are wider in the nose region. This widening induces an acceleration in the slurry that, at the same time, produces a wave. While this wave is propagating towards the tail of the bubble, it may grow larger than the depth of the plug tail. If so, the tail is cut off and a smaller bubble stands between the two large plug bubbles. As the solid particles remain in the liquid phase (they do not cross the liquid-gas interface) after the detachment is completed an accumulation of particles is observed around the detached bubbles, and these smaller bubbles generally coalesce with the next plug bubble. This mechanism is known as drag induced coalescence, where larger bubbles overtakes the smaller ones due to relative motion (Talley et al. [2015]). In fig. 3.4 a sequence of the coalescence process of a plug bubble with a smaller bubble is shown for a three-phase, 5% loading plug regime flow, with $j_{fs} = 1.06\,m/s$ and $j_g = 0.4\,m/s$. In fig. 3.4a the plug bubble on the right is reaching a smaller one, previously detached from the large plug bubble on the very left of the image. In figs. 3.4b and 3.4c an interface between the two bubbles is developed. An accumulation of solid particles between the two interfaces is observed (white dots). The solid particles are displaced around the nose of the plug bubble and some of them get attached to the pipe wall. Later in fig. 3.4d the interface gets thinner, while the solid particles are still being displaced, until the interface breaks in fig. 3.4e. Finally, (fig. 3.4f) the large bubble formed from the coalescence moves forward reshaping into the plug bubble shape and the solid particles attached to the pipe wall are dragged by the slurry.

In slug flows, the presence of the small bubbles in the slurry regions between the slug (large) bubbles, can be explained by the same mechanism as in plug bubbles. This is by the break up of the tail region induced by the waves, but another break up process is observed. This other process is linked with the relative velocity between the gas and slurry phases. As the relative velocity increases higher shear stresses are generated and detachment of several small bubbles is observed. These phenomena are illustrated in figs. 3.2 and 3.3. It can be seen that as the relative velocity increases the number of bubbles also increase until the density of small bubbles is so high that the bubbles became indistinguishable. Finally, it is also appreciable from the videos, that a clockwise vortex follows the slug elongated bubbles, fig. 3.5. These vortices

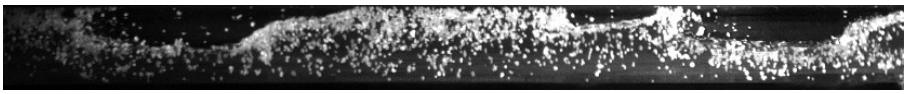

(a) $t = 0\,ms$ - plug bubble (right) reaching detached small bubble.

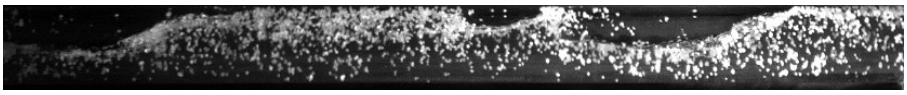

(b) $t = 37.5\,ms$ - accumulation of solid phase (white dots) between the bubbles.

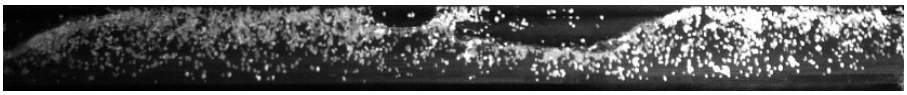

(c) $t = 71.3\,ms$ - displacement of solid phase around the nose of plug bubble.

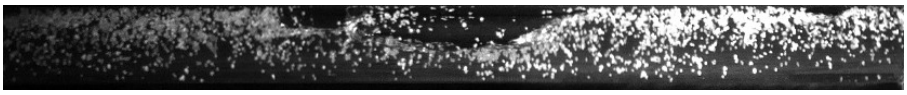

(d) $t = 101.5\,ms$ - the interface between bubbles gets thinner.

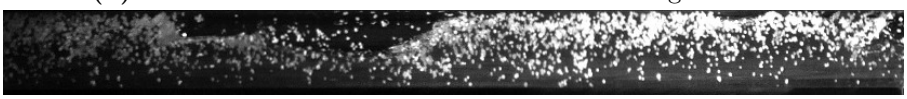

(e) $t = 138.1\,ms$ - coalescence, the interface collapses.

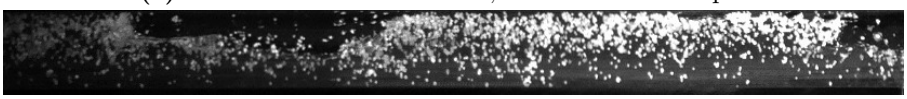

(f) $t = 153.8\,ms$ - reshape of the bubble after coalescence.

Figure 3.4: Coalescence sequence of a plug bubble and a smaller one, $j_{fs} = 1.06\,m/s$, $j_g = 0.4\,m/s$ and $C_s = 0.05$, flow from right to left.

produce a continuous bubble detachment from the lower tip of the slug bubble, and they also contribute to break the upper part of the tail, observing the effect of a breaking wave in the tail of the bubble. During the breakage some droplets are ejected into the air bubble and several small bubbles are detached from it. It also appreciable that the breaking wave goes through the bottom interface producing a vertical downward velocity in the tail of the bubble, and helps the mixing of the phases.

3.2. Annular flow

Annular gas-liquid two-phase flows are characterized by having a portion of the liquid phase flowing as a film along the wall of the pipe, while the other portion does so in in the form of drops. The latter travel dispersed in a gas core flow in the center of the pipe, at relatively high velocities. Droplets dispersed

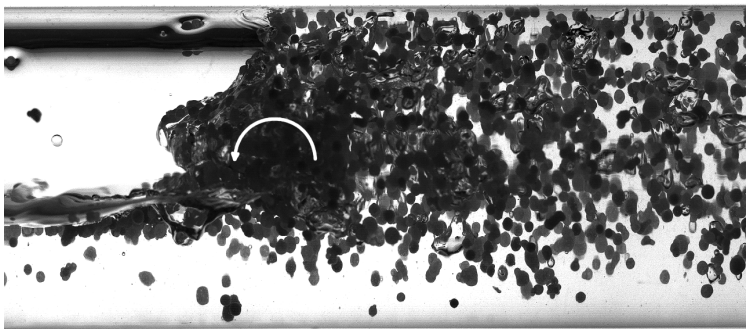

Figure 3.5: Animation of a vortex located next-to the tail of a slug elongated bubble, $j_{fs} = 1\,m/s$, $j_g = 1\,m/s$ and $C_s = 0.1$

in the continuous gas phase are often referred to as the entrained fraction of annular flows. Due to the high velocities of the gas phase, the shear force in the interface is enough to produce instability waves in the liquid film, which lead to liquid entrainment in the gas phase. A detailed description of droplets entrainment and break-up processes can be found in Azzopardi [1997]. As the drops travel in the gas flow, eventually, they are deposited again in the liquid film. These two processes, entrainment and deposition, occur constantly, and the flow is said to be fully developed when both processes reach the equilibrium.

Figure 3.6: Scheme of annular flow inside a pipeline.

Annular flows are present in both horizontal and vertical pipelines, and can be found in industrial equipment for a wide variety of applications, mainly related to heat and mass transfer. Heat exchangers and boiler tubes are examples of commonly used industrial equipment (Azzopardi [1997]), nuclear reactors are cooled with water where a portion of it evaporates in the core of the pipes (Azzopardi [1985]). Annular flows are also used in smaller scale equipment as evaporators or condensers (Ambrosini et al. [1991]), where the mass flow distribution has a significant impact on its performance (Winkler and Peters [2002]). Further applications are found in the chemical industry where reactions are also governed by heat, but mainly due to mass transfer, and because annular flows are stable regimes, these are often desired in two-phase flow processes (Steimes and Hendrick [2017]).

Comprehensive understanding of annular flows is very important. In

particular, in chemical reactions it is essential to predict the amount of interface between the phases, since it is through this that the heat and mass transfer occur, which govern the reactions. Accordingly, the dispersed drops, that travel in the core of the pipeline at very high velocities, have a very important role. Numerical simulations are a great tool when it comes to predicting such characteristics. But it is well known that to obtain reliable results it is necessary to validate the models with experimental results.

3.2.1. Previous studies

Because of the waves on the liquid film travelling in the walls of the pipeline, it is not possible to use common visualization techniques with transparent pipes on annular flows. Hence, alternative techniques have been developed in order to measure drop size or entrainment rates with optical approaches. Despite the fact that annular flows have been studied frequently since the 1960s, most of the studies on droplet size measurements found in the literature correspond to vertical upward flows. In a review made by Azzopardi [1997], only 5 out of a total of 28 experimental studies collected correspond to horizontal flow, including data taken with unreliable techniques of measurement according to the review author. Furthermore, in a more recent review by Berna et al. [2015] only 3 studies were reported on droplet size measurements for horizontal annular two-phase flow. Other authors focused their studies on the entrainment rate, where the majority of these works did not calculate droplet size neither size distributions. A compilation of experimental data on entrainment rates can be found in Pan and Hanratty [2002].

Most of the studies on the available literature are based on optical measurement techniques. Within these, laser diffraction systems in horizontal flows were used by Ribeiro et al. [2001], Zaidi et al. [1998], Al-Sarkhi and Hanratty [2002], Simmons and Hanratty [2001], Steimes and Hendrick [2017], Azzopardi and Zaidi [1997], among several others in vertical flows (Azzopardi [1997]). Laser diffraction techniques became very popular for measuring droplet sizes. It is an integrative technique, that can measure large samples, however the measurement is indirect. With this technique an energy distribution of scattered light, diffracted by spherical drops, is obtained. In the post-processing a droplet size distribution is presumed and an energy distribution is calculated, finally parameters of the size distribution

are adjusted to best fit the measured and calculated energy. For this purpose several distributions have been proposed or taken from other fields. In older studies the Rosin-Rammler (1933) equation was well accepted, but later it has been proven that log-normal distributions best fit the droplet size distribution in annular flows. Within these is the "upper limit log normal" (ULLN) distribution, proposed by Mugele and Evans [1951] to describe droplet size distributions in atomising jets. A comparison of different distribution functions with experimental data can be found in Simmons and Hanratty [2001]. In a critical review, Azzopardi [1997] compares data from different techniques, concluding that older diffraction data analyzed with the Rosin-Rammler approach should be reanalysed using the model-independent approach (used in Azzopardi and Zaidi [1997]), although it is useful to identify parametric trends.

Photography techniques, which are mostly localized due to the narrow depth of field, have also been widely used, mostly in vertical upwards flows, Hay et al. [1996]. The main advantage of this approach is that it allows to individually examine the drops, resulting in accurate measurements of large drops. Due to resolution limitations, accuracy is lost for small droplets. Also, a large number of images are required in order to obtain conclusive results, what leads to extensive post processing. In older studies, enlarged printings were used, however some of the reported data were later judged to miss the small drops or having too small sample sizes (Azzopardi [1997]), which leads to large deviations on the measurements. Bowen and Davies [1951] have estimated (within 95% confidence limits) that an accuracy of 10% is reached with at least 1400 samples, moreover, for obtaining accuracies of 5% and 2%, sample sizes of 5500 and 35000 particles are required respectively.

In relatively more recent works, thanks to the improvement in photography resolution and also the increase on computing capacity, photography techniques have been used together with image processing algorithms. Hurlburt and Hanratty [2002] used the Immersion method, developed by Fujimatsu et al. [1997], where samples of droplets from horizontal annular flows are captured in small bins filled with high-viscosity oil. The bins are photographed, and the images are then processed to determine individual drop diameters. Later, Lee et al. [2010] applied a freezing technique for extracting and photograph the droplets. They used a camera-magnification arrangement leading to very good resolutions, however the image processing was performed

manually and hence the sample sizes are quite small, less than 1000 for each operation condition, which results in important inaccuracies. While these last two in-situ techniques might produce good results in the laboratory, they could hardly be applied to operating facilities. Whereas optical methods can potentially be used for inline metering.

Other measuring techniques that have been used for determining drop sizes in vertical annular flows are the Phase Doppler Anemometry Zaidi et al. [1998] and laser grating Fore and Dukler [1995]. Also charge removal was used by Tatterson et al. [1977] and needle bridge by Wicks and Dukler [1966], but both methods have been labeled as unreliable techniques for measuring droplet size distributions (Azzopardi [1997]).

To reach the droplets in the core of the pipe, several techniques have been proposed. The film extraction is one of the most used routines, within these, the use of porous walls is the most repeated approach (Azzopardi [1985], Simmons and Hanratty [2001], Al-Sarkhi and Hanratty [2002]), also film deviation was used by Hay et al. [1996]. Other authors, dealing with higher liquid flow rates, have chosen to extract a part of the droplet flow before the measuring zone (Steimes and Hendrick [2017]). Fore and Dukler [1995] have devised a measurement station to access the gas-droplet core without removal of the liquid film. For this, two smaller tubes (facing each other) cut across the main pipe, penetrating the liquid film orthogonally. In this way the laser could enter through one of the small tubes, cross the droplet flow without interacting with the liquid film, and exit through the opposite tube. table 3.1 lists most of the published measurements of droplet size distribution for annular two-phase flows in horizontal pipelines. Furthermore, Fore and Dukler's vertical study has been included because the proposed measurement station has not been found in horizontal flow studies.

Finally, it is worth mentioning that Fore & Dukler's measurement station is closer to the drop creation, because there is no liquid film extraction. This has been pointed by Azzopardi [1997] while comparing data obtained with different techniques. As an example, the Sauter mean diameters measured by Fore and Dukler with the laser grating technique are significantly larger than those calculated by Azzopardi and Zaidi [1997] with laser diffraction technique analyzed using a model independent approach. Also, the data from Zaidi et al. [1998] with the PDA technique, on the same test section used by Azzopardi and Zaidi [1997], is closer to the obtained by Fore and Dukler, but still smaller

Table 3.1: Summary of previous studies on Droplet size distribution

Author	Orientation	Pipe diameter [mm]	Superficial velocity range [m/s]		Technique	Film / Droplet handling
			gas	**liquid**		
Fore and Dukler [1995]	Vertical	50	16 - 33	0.015 - 0.067	Laser grating	Visualization window through liquid film
Azzopardi and Zaidi [1997]	Horizontal to Vertical	38	15 - 30	0.02 - 0.16	Diffraction (Malvern)	Film extraction (porous wall)
Zaidi et al. [1998]	Horizontal to Vertical	38	15 - 30	0.02 - 0.16	Phase Doppler Diffraction	Film extraction (porous wall)
Ribeiro et al. [2001]	Horizontal	32	25 - 45	0.03 - 0.11	Diffraction	
Simmons and Hanratty [2001]	Horizontal	95.3	30 - 50	0.01 - 0.1	Diffraction (Malvern)	Film extraction (porous wall)
Al-Sarkhi and Hanratty [2002]	Horizontal	25.4	25 - 50	0.01 - 0.11	Diffraction (Malvern)	Film extraction (porous wall)
Hurlburt and Hanratty [2002]	Horizontal	95.3	20, 30 & 36	0.015, 0.04 & 0.07	Immersion method (Photographic)	Drops captured
Lee et al. [2010]	Horizontal	37.1	40 & 50	0.025	Freezing technique (Photographic)	Drops freezed
Steimes and Hendrick [2017][a]	Horizontal	38	14.7 - 30	0.039 - 0.15	Laser diffraction (Sympatec)	Droplet extraction

[a] Air-oil two-phase flow

sizes are presented. This suggest two outcomes, first that the large, short-living drops are not captured with film extraction handling procedures. And second that the data obtained with the laser diffraction technique should be contrasted with other measurements techniques to evaluate its effectiveness.

3.2.2. Experimental facility

Flow Loop

- The experiments have been conducted at a two-phase flow loop for investigation of air-water flow at ambient conditions in horizontal test sections. The flow loop is fully described in Porombka et al. [2021] so that only a brief description is presented here.
- A flow schematic of the experimental facility is given in fig. 3.7 which consists of an open air-loop and a closed water-loop. The dryed and cleaned compressed air mass flow rate is controlled by one of two mass flow rate controllers and flows to the air-water mixer. Deionized water is pumped at from the vented separator tank by a frequency controlled gear pump to the mixer and radially injected into the air stream by eight hollow-cone spray nozzles.
- The dispersed water and air mixture develops downstream of the mixer

in the horizontal test section. From the test section outlet the two-phase mixture is fed to a separator tank through a flexible hose. From the separator tank, air is vented to the ambiance and water is recycled to the test section.

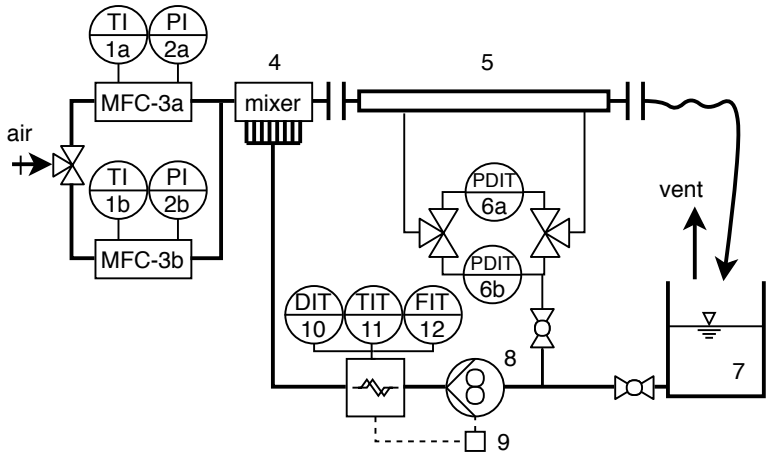

Figure 3.7: Schematic of air-water flow loop. 1 – temperature sensor, 2 – pressure transducer, 3 – mass flow controller, 4 – mixer, 5 – test section, 6 – differential pressure transducer, 7 – separator tank, 8 – geared pump, 9 – frequency controller, 10 – density sensor, 11 – temperature sensor, 12 – Coriolis-type mass flow meter. *Reprinted from "Horizontal annular flow through orifce studied by X-ray microtomography" by Porombka P. et. al., 2021, Experiments in Fluids, 62:5*, license

Test Section

- The transparent pipe test section is composed of flanged acrylic glas (PMMA) modules which can be arranged arbitrarily. Three different test section geometries have been investigated in this study:

  1. straight pipe with $L/D = 223$
  2. straight pipe with $L/D = 196$ and a circular orifice with a diameter ratio $d/D = 0.775$ positioned at $z/D = 116.4$ downstream of the mixer.
  3. straight pipe with $L/D = 221$ with an sudden expansion by $D'/D = 1.71$ positioned at $z/D = 116.4$ downstream of the mixer.

Measurement Technique

flow microscope

- As described in section 3.2.1 droplet size measurement in annular flow with optical methods requires access to the core flow through the liquid film attached to the wall. This is achieved either by extracting the liquid film through slits or porous walls or by inserting a device that acts as fence to the liquid film. Here, the latter approach outlined by Fore and Dukler [1995] is followed and a flow microscopy module was developed according to fig. 3.8.
- The flow microscope allows the radial positioning of two small acrylic tubes into the test section. The insertion depth of the tubes may be adjusted so that they penetrate the annular liquid film. To prevent liquid droplets from depositing on the sight glass, air is purged through radial drillings in the insertion tubes.
- In the application of this measurement module, it is assumed that the blockage by the insertion tubes and the purge air does not affect the upstream droplet size distribution.
- A Photron Mini AX 100 High-Speed Camera adapted to a long-distance microscope lens is positioned on one side of the flow microscopy module and the white cluster LED light source is positioned on the opposing side. The camera is mounted on a two-axis precision stage so that the optical axis and the focus position can be adjusted. The light source is continuously operated and focussed on the viewing window by a lens arrangement. Different apertures in the focussing optics allow to adjust the light intensity as needed.

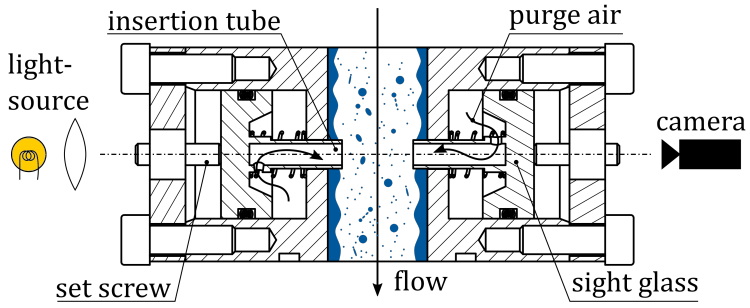

Figure 3.8: Sectional view of flow microscopy module applied in droplet size measurements, not to scale.

For each recording, a batch of 8000 images are captured with a low sample rate, so that two consecutive frames do not capture the same drop. Also,

the flow microscope module is setted at several axial positions for each test section (three or four). A summary of the test sections and axial positions where images are taken is provided in table 3.2. In addition, three focus planes are used in each axial position by moving the precision stage (α, β and γ). Then, there are images focused on three axial planes, including the middle plane and two planes ± 0.09 ID away from the middle. This results in a total of 30 batches of image.

Table 3.2: Summary of test sections and axial positions.

Test Section	Name	Axial Position	z/D	z^*/D
Straight Pipe	TS1A	b	4.6	-
		c	11.8	-
		d	36.8	-
Orifice	TS1B	b	114.6	-1.8
		c	117.5	1.1
		d	121.1	4.6
Expansion	TS1C[a]	b	114.6	-1.8
		c	117.5	1.1
		d	121.1	4.6
		e	135.4	18.9

For each axial position, three focus planes are used (α, β and γ).
z^* Measured relative to orifice or expansion (downstream edge) position.
[a] In the axial position z/D the small diameter is used.

An image processing algorithm was developed to analyze the obtained images. The algorithm is capable of identifying the droplets in the images, measure the equivalent sphere diameter (ESD). The full algorithm together with the corresponding calibration and validation are described in appendix C.

3.2.3. Experimental results

3.2.3.1. Droplet size distributions

The image processing algorithm, fully described and validated in appendix C, was applied to all the test sections, axial positions and focus

planes from table 3.2. For every batch of images a PDF of the quivalent sphere diamters is calculated, fig. 3.9 shows an example of a calculated PDF for case TS1A–d–β. The blue bars correspond to the histogram of the measured droplet sizes. It can be seen that, although a small size threshold is used (drops with an area smaller than 24 pixels are discarded, see appendix C), a very steep slope can be identified at the beginning of the distribution. This denotes that the smallest droplets have been captured by the camera and identified by the algorithm.

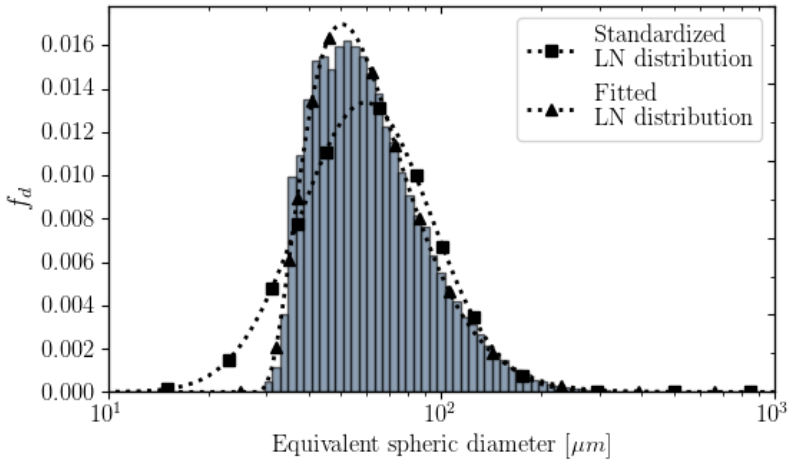

Figure 3.9: Histogram and probability density function of droplet size distribution for TS1A–d–β

The dotted line with the square markers from fig. 3.9 correspond to the log-normal PDF. Which is defined in the standardized form with eq. (3.1),

$$f_d(x) = \frac{1}{\sqrt{2\pi} \cdot x \cdot \sigma} \cdot \exp\left[-\frac{1}{2}\left(\frac{log(x) - \log(d_\mu)}{\sigma}\right)^2\right] \tag{3.1}$$

where d_μ is the median diameter of the log-normal distribution function, and is calculated as $d_\mu = \exp(\mu)$. μ is the mean and σ is the standard deviation of the normally distributed logarithm of the measured data. However, the logarithm of the data is not perfectly normally distributed, and so the fitting is not so accurate. The PDF with the triangle markers in fig. 3.9 is obtained by introducing a location parameter, δ, to shift the distribution in the x-axis, and fitting the values of the mean μ' and the standard deviation σ'. The fitted PDF is calculated with the fitted parameters in eq. (3.2).

$$f'_d(x) = \frac{1}{\sqrt{2\pi}\cdot(x-\delta)\cdot\sigma'}\cdot\exp\left[-\frac{1}{2}\left(\frac{log(x-\delta)-\log(d'_\mu-\delta)}{\sigma'}\right)^2\right] \tag{3.2}$$

The characterization of the droplet size distribution finish by calculating the mean, or expected value ($\bar{d}$). Also, the standard deviation (S) and skewness (Γ) of the log-normally distributed data can be calculated. These parameters are defined for a log-normal distribution with eqs. (3.3) to (3.5).

$$\bar{d} = \exp\left(\mu + \sigma^2/2\right) \tag{3.3}$$

$$S = \sqrt{\exp\left(\sigma^2+2\mu\right)\cdot\left[\exp(\sigma^2)-1\right]} \tag{3.4}$$

$$\Gamma = \sqrt{e^{\sigma^2}-1}\cdot\left(2+\exp(\sigma^2)\right) \tag{3.5}$$

3.2.3.2. Droplet volume distributions

The droplet diameter distribution from fig. 3.9 is suitable for comparison with CFD data for validation. However, the diameter distribution is not log-normally distributed and has to be shifted (eq. (3.2)). Moreover, the difference in mass of liquid contained on drops of different sizes can be very meaningful, and therefore a volume distribution is more suitable for its representation. fig. 3.10 shows an example of the droplet volume distribution for the batch of images of run TS1A–d–β.

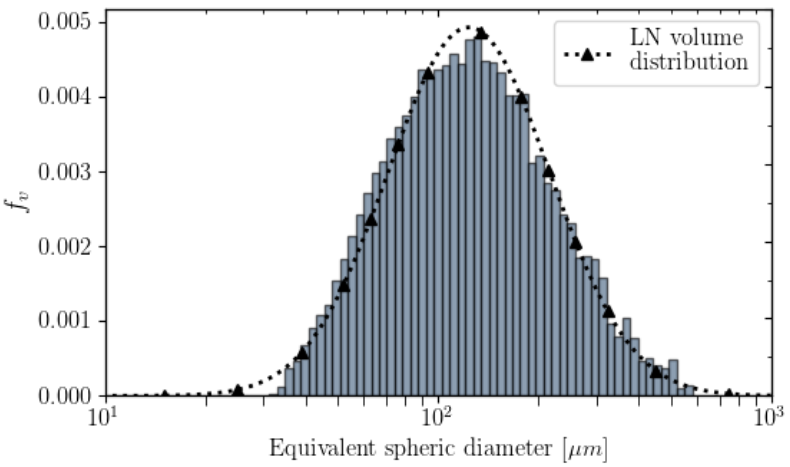

Figure 3.10: Histogram and probability density function of volume distribution for TS1A–d–β

The log-normal volume distribution from fig. 3.10 is calculated with eq. (3.6). The mean and standard deviation of the logarithm of the drops diameters (vector d), weighted with the volume of the drops (vector v) are used, which are calculated with eqs. (3.7) and (3.8).

$$f_{\mathrm{v}}(x) = \frac{1}{\sqrt{2\pi}\cdot x\cdot \sigma_{\mathrm{v}}}\cdot \exp\left[-\frac{1}{2}\left(\frac{log(x)-\log(d_{\mathrm{v}\mu})}{\sigma_{\mathrm{v}}}\right)^2\right] \tag{3.6}$$

$$\mu_{\mathrm{v}} = \frac{\sum v\cdot\log(d)}{\sum v} \tag{3.7}$$

$$\sigma_{\mathrm{v}} = \sqrt{\frac{\sum v\cdot(\log(d)-\mu_{\mathrm{v}})^2}{\sum v}} \tag{3.8}$$

Note that $d_{\mathrm{v}\mu} = \exp(\mu_{\mathrm{v}})$ is the volume median diameter (VMD), this represents the midpoint size where half of the volume is in drops smaller than the VMD, and the other half in drops larger than the VMD. Finally, a commonly used value to represent drop size data is the Sauter mean diameter (d_{32}), which represent the diameter of a particle whose ratio of volume to surface area is the same as that of the complete sample. It is defined in eq. (3.9) and for a log normal distribution can be calculated with d_{vm} and σ_v in eq. (3.10)

$$d_{32} = \frac{\int_0^{d_{\max}} d^3 n(d)\mathrm{d}d}{\int_0^{d_{\max}} d^2 n(d)\mathrm{d}d} \tag{3.9}$$

$$d_{32} = \frac{d_{v\mu}}{\exp\left(\sigma^2/2\right)} \tag{3.10}$$

3.2.3.3. Axial development

In this section the axial development of the annular flow for the three configurations is analysed. The total amount of droplets identified by the algorithm, the volume they contain and the mean diameter of the droplets are reported in section 3.2.3.3 for a straight pipe, a pipe with an orifice and an expansion respectively.

Straight pipe

The bar charts from fig. 3.11 are used to analyse the axial development of an annular flow in a 14 mm diameter straight pipe. Measurements are reported for axial positions b, c and d corresponding to 4.6, 11.8 and 36.8 diameters from the outlet of the mixing chamber respectively (see table 3.2). There is a set of 3 bars for each axial position (b, c, and d), in which the color of the bar indicates the focus plane of the camera used during the shooting. The chart on the left shows the number of drops recognized by the algorithm, the one in the middle gives magnitude to the total volume carried in the drops, and the chart on the right shows the average size of the drops (ESD).

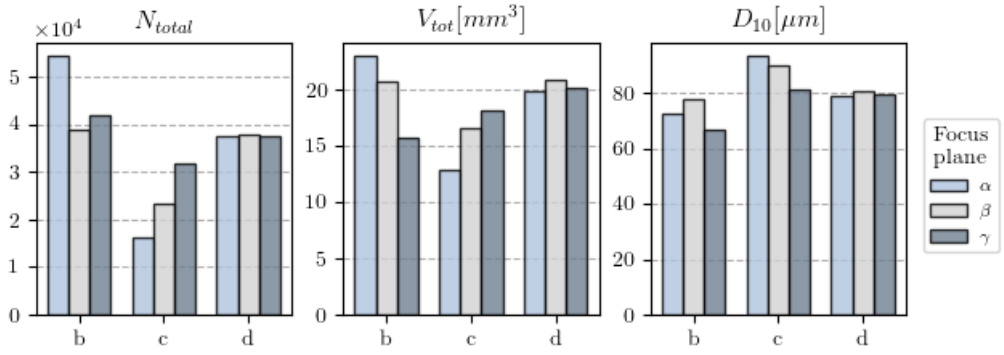

Figure 3.11: Number, total volume and mean diameter of droplets for annular flow in a 14 mm diameter straight pipe.

Several observations can be done by analysing the bar charts from fig. 3.11. First of all, it can be notice that at axial position 'b' the number of identified droplets is greater, presenting a smaller size and an imbalance in the cross sectional population towards α-plane ($x = +0.1D$). While at position c, fewer drops have been identified, with a slightly larger size, and with an imbalance towards the γ-plane ($x = -0.1D$).

To explain this phenomena, it is helpful to analyze the development of the liquid film. fig. 3.12 shows the thickness of the liquid film along the z-axis of pipe, obtained from a x-ray tomography. Further details on the construction of the image and discussion can be found in Porombka et al. [2021]. From fig. 3.12, it can be seen that during the first 25 diameters of the pipe the liquid film is not fully developed.

In the mixing chamber, very small droplets are injected by 8 nozzles in the gas flow. The entrance in the test section is at position $z/D = 0$ in fig. 3.12. The liquid film is then gradually formed by the droplets that reach the pipe

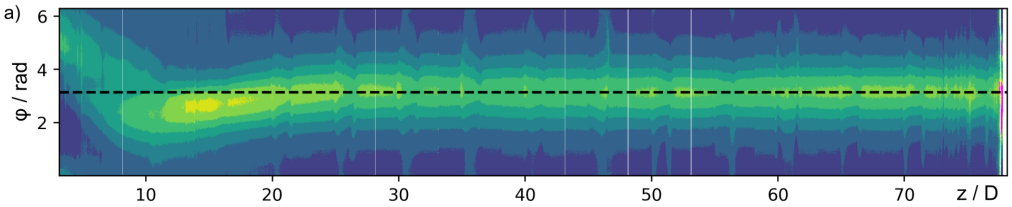

Figure 3.12: Liquid film thickness distribution for the straight pipe arrangement (TS1A). *Reprinted from "Horizontal annular flow through orifce studied by X-ray microtomography" by Porombka P. et. al., 2021, Experiments in Fluids, 62:5,* license

wall. The liquid fraction in the film (fig. 3.12), grows during the first 15 diameters in the z-axis of the pipe. The peak is reached and then it decreases again, until it gets stationary at about 25 diameters from the mixing chamber. This explains the largest number of drops in section b (fig. 3.11), where the liquid fraction in the film is at mid values; and the smaller size of the drops in section b ($z/D = 4.6$), which are, for the most part, those formed by the nozzles. Also, the least amount of droplets (and total volume) in section c ($z/D = 11.8$), coincides with high values of the overall liquid film thickness. In other words, part of the liquid fraction has passed from the dispersed phase to the liquid film.

Moreover, the thickness of the film is not evenly distributed along the perimeter of the cross section. Of course, the film is expected to be thicker at the bottom of the pipe due to gravitational effects, but there is also a deviation towards positive values of the x-coordinate during the first 8 diameters and then in the opposite direction (fig. 3.12). This indicates that the flow, probably influenced by the last nozzle of the mixing chamber, has a positive velocity in the x direction (refer to Porombka et al. [2021] for more details of the mixing chamber). The unstable film produced in the first stage then accelerates towards the bottom due to gravitational effects, and overcomes the lower bound line of the pipe towards x- by the inertia gained from the movement. Once again, the previous description is in concordance with the unbalance in the population of droplets in the cross section, towards α-plane and γ-plane at axial positions b and c respectively.

Finally, at axial position d ($z/D = 36.8$), where the film is fully developed, the droplet population is balanced in the cross section. Additionally, the total volume is greater than at axial position c, indicating that a fraction of the liquid that was in the film at position c moved to the dispersed fraction at

position d. This suggests that the dispersed liquid fraction is also developed at position d, with droplet detachment and deposition from and towards the liquid film.

Orifice

The same axial analysis has been performed for the annular flow straight pipe with an orifice. The bar charts from fig. 3.13, also shows the population of droplets, the total volume they contain and the mean diameter. The axial positions b, c and d refers to 114.6, 117.5 and 121.1 diameter downstream the mixing chamber. The orifice is located at 116.4 diameters, between sections b and c.

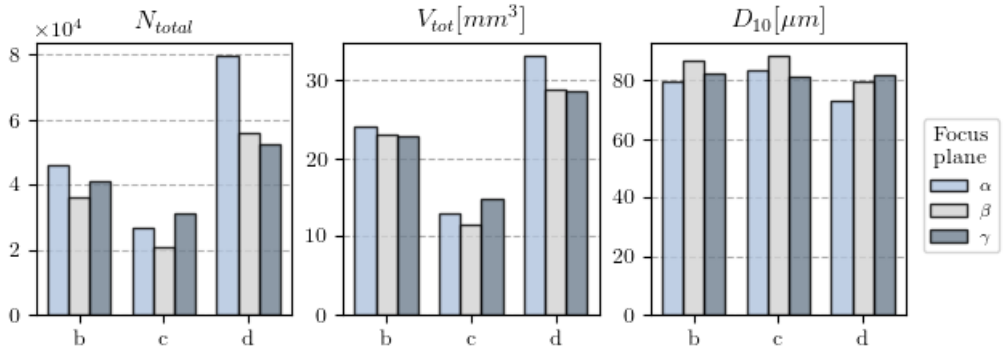

Figure 3.13: Number, total volume and mean diameter of droplets for an orifice in a straight pipe, annular flow.

As expected, the population, distribution and size of droplets at axial position b, correspond to that of a developed flow, very similar to axial position d in the straight pipe arrangement (fig. 3.11). At position c, 1.1 diameters after the orifice, a significant reduction in the population is observed. When the flow passes through the orifice, the fraction of liquid that travels in the film moves towards the center of the pipe. Also, since the cross section is smaller, the flow experiences an increase in velocity, which generates higher shear forces. As a result, liquid structures of many sizes and shapes are shed, and the fraction of liquid travelling in the center of the tube is much greater than that of a developed flow. Therefore, the images obtained present a high density of complex structures, both in the focus plane and outside it, many of which are discarded by the algorithm, since they are not drops.

Finally, 4.7 diameters downstream of the orifice, at axial position d, the droplet population increases significantly (left panel in fig. 3.13). Some liquid

structures still exist, but the vast majority have fragmented into smaller structures and droplets (due to high shear forces and collisions) or have fallen by gravity joining the liquid film. Accordingly, the density of liquid structures is reduced again, which favors the detection of isolated drops. Beyond the increase in the number of drops, a deviation towards the α-plane is also observed. However, this deviation is not as significant in volume (middle panel), because the mean droplet size (right panel) is modestly smaller in α, which compensates for the population increase with a ratio of three to one.

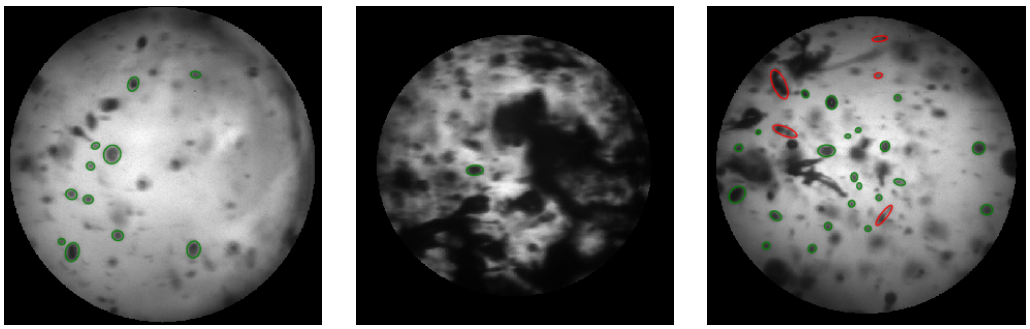

(b) (c) (d)

Figure 3.14: Example of images for sections b, c and d

Three examples of typical figures obtained at axial position b, c and d are presented in fig. 3.14. The identified drops are surrounded by colored ellipses, the green ones are kept as drops and the red ones are discarded as they might be out of focus or correspond to long filaments. The increase on liquid structures from axial position b to c is easily identified by the large dark areas in the middle image, and in the same way a reduction in density of structures is observed in the figure on the right. It can also be seen in the image on the right that many drops were detached from larger structures.

Expansion

Finally, the same results are presented for the expansion in fig. 3.15. At axial position b ($z^*/D = -1.8$ from the expansion) an increase on population is seen at focus planes α and γ (away from the middle plane). Then, at axial positions c and d, there is a reduction and a increase on the population respectively. This is explained for the same reasons as for the orifice, the presence of many fluid structures on section c that eventually breaks in smaller droplets in section d. Finally, at axial position e the amount of droplets

decrease significantly, due to the deposition of dorplets and structures in the liquid film. The population of droplets at section e is in the order of that of a developed flow. However, an unbalance is present towards the focus plane α, which is not compared to a developed flow. To determine why this effect occurs, it should be analysed in more detail with other measurement techniques, such as a X-ray tomography, as in fig. 3.12.

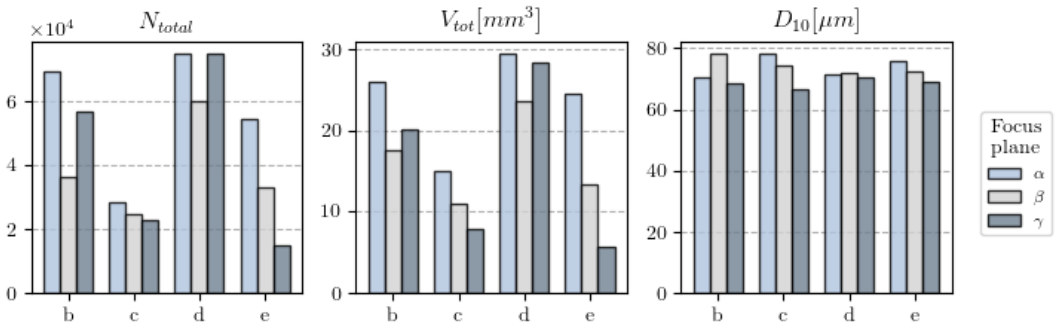

Figure 3.15: Number, total volume and mean diameter of droplets for an expansion in a straight pipe annular flow.

3.3. Flow regime map

3.3.1. Previous studies

Two-phase flow regime maps indicate the flow regime of two-phase flows in a plane where the vertical axes represent the superficial liquid velocity and the horizontal axis represents the gas superficial velocity. It is helpful to predict the flow regime of a two-phase setting, only by knowing the input flow rates of liquid and gas in the pipe. Several flow regime maps for horizontal flows have been proposed by different authors Baker [1953], Hoogendoorn [1959], Govier and Omer [1962], however there are mainly two flow maps that are generally used. The first one developed by Mandhane et al. [1974] with experimental data obtained from a data base with a wide range of flow regimes and physical properties. However, no influence on the pipe size was reported until the works of Taitel and Dukler [1976]. They have suggested that for large pipe diameters, the bubbly to plug and the plug/slug to stratified boundaries move to larger values of liquid superficial velocities, and that the stratified to annular transition boundary, is displaced towards a larger gas superficial velocity. Taitel and Dukler [1976] developed the map from a theoretical model

analysis. In fig. 3.16 the regimes maps of Mandhane et al. [1974] and Taitel and Dukler [1976] (for a 2.5 cm ID) are plotted together for comparison.

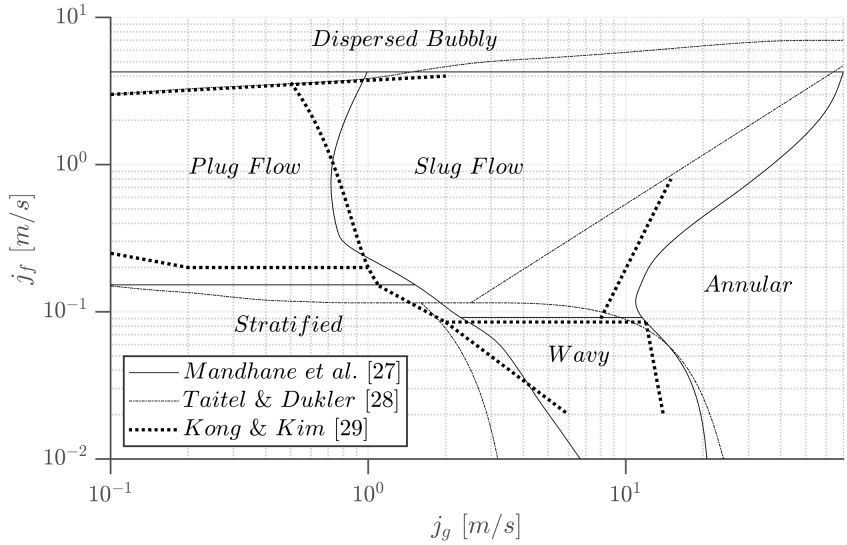

Figure 3.16: Regime maps for two-phase flows in horizontal pipelines

The main differences between the two maps are (1) the transition from bubbly to intermittent flow proposed by Mandhane et al. [1974] occurs at superficial velocities of the liquid phase of 4.20 m/s independently of the gas superficial velocity, while Taitel and Dukler [1976] state that for higher flow rates of gas the transition occurs at higher rates of liquid. Furthermore, (2) the transition from stratified to intermittent flows in Taitel and Dukler's map requires higher liquid superficial velocities than Mandhane et al.'s map. Finally, (3) Taitel and Dukler [1976] refers to intermittent flows without a distinction between Plug and Slug flows. On the other hand, Mandhane et al. [1974] sets a transition boundary between elongated bubble (plug) and slug flows.

Recently, Kong and Kim [2017] have studied the transition boundaries by classifying 263 flow conditions from a detailed flow visualization study using a high-speed video camera. The study includes bubbly, plug, slug, stratified, stratified-wavy and annular flows with their respective transitions. They concluded that the transition from bubbly to intermittent depends on j_g, as proposed by Taitel and Dukler [1976]. In this case they also observed that more gas is required for the transition from plug to slug at j_f less than 1 m/s, and less gas is required for j_f above 1 m/s. The map proposed by Kong and Kim is also included in fig. 3.16.

Other authors prefer using flow regime maps based on the superficial Reynolds numbers, Re_f and Re_g calculated with the corresponding superficial velocities. Such is the case of Vaze and Banerjee [2012] whose authors proposed a Reynolds based flow regime map including annular, plug, slug/bubbly/annular, slug, stratified, slug/wavy, wavy and wavy/annular flows. Later, Thaker and Banerjee [2015] slightly modified the regime map based on flow visualization of 406 combinations of volume flow rate of water and mass flow rate of air. The modified map include different regimes nomenclature, including plug, slug and plug, less aerated slug, high aerated slug, slug formation, slug with wavy interface, and stratified flows.

Despite the difference on the nomenclature of the regimes, the maps are quite similar, after all, they refer to the same regimes.

3.3.2. Effect of solid phase

Videos have been recorded for 62 different test conditions including plug, plug-to-slug transition and slug regimes for air-water two-phase flows and air-water-polyethylene three-phase flows with 5 and 10 % of solid concentrations. Each condition was thoroughly visually analysed in order to determine the corresponding regime and unveil the influence of solid concentration on the transition boundaries.

In fig. 3.17 the section of the regime map covered in the present study is displayed. Transition boundaries between plug and slug proposed by Mandhane et al. [1974] and Kong and Kim [2017] for two-phase flows are indicated in the legend, as well as the proposed ones in the current study, for three-phase flows. Each test condition is plotted with a marker in the map, white marks correspond to air-water two-phase runs, grey marks to three-phase runs with 5% loading of solids and black marks to 10% loading; the flow regime visualized for each run is indicated with the shape of the markers, triangles for plug flow, diamonds for plug-to-slug transition and squares for slug flow.

From the visual analysis of the two-phase runs it is observed that transition zones are wide, and they can hardly be expressed with a line. In any case, our measurements agree with the observations of Kong and Kim [2017] regarding the plug-to-slug transition, where they claim that less air is required to reach slug flow at j_f above $1m/s$ and vice versa.

For three-phase flows, it is observed that the accumulation of particles

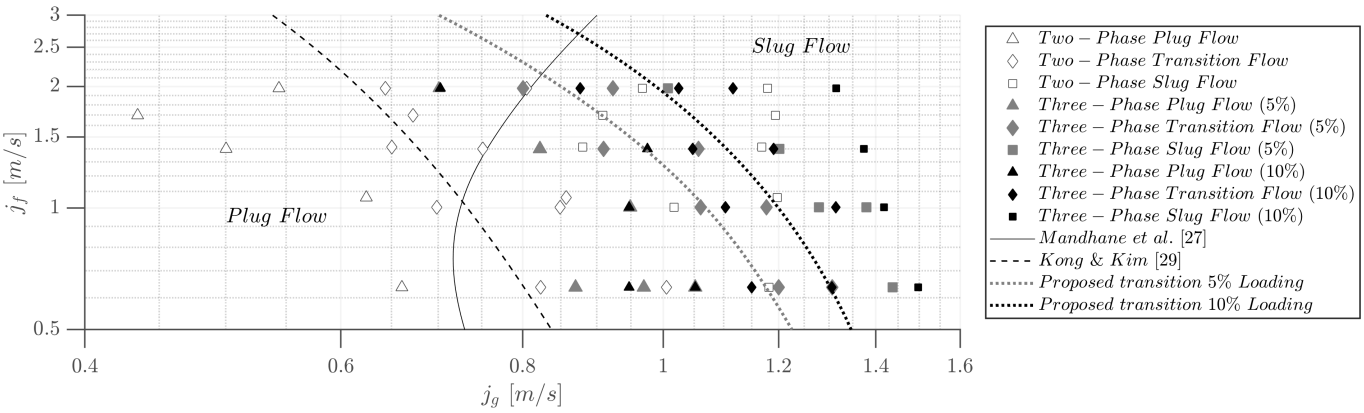

Figure 3.17: Effect of solid phase on plug-to-slug transition.

in the tail of plug flows, retards the small bubble detachment for increasing relative velocities, thus the transition from plug to slug flow is displaced towards higher gas superficial velocities.

3.4. Bibliography

Justin D Talley, Ted Worosz, Seungjin Kim, and John R Buchanan. Characterization of horizontal air – water two-phase flow in a round pipe part I : Flow visualization. *International Journal of Multiphase Flow*, 76:212–222, 2015. ISSN 0301-9322. doi: 10.1016/j.ijmultiphaseflow.2015.06.011. URL http://dx.doi.org/10.1016/j.ijmultiphaseflow.2015.06.011.

Roland Rzehak and Eckhard Krepper. CFD modeling of bubble-induced turbulence. *International Journal of Multiphase Flow*, 55:138–155, 2013. ISSN 03019322. doi: 10.1016/j.ijmultiphaseflow.2013.04.007. URL http://dx.doi.org/10.1016/j.ijmultiphaseflow.2013.04.007.

B. J. Azzopardi. Drops in annular two-phase flow. *International Journal of Multiphase Flow*, 23(7):1–53, 1997. ISSN 03019322. doi: 10.1016/S0301-9322(97)90087-2.

B. J. Azzopardi. Drop sizes in annular two-phase flow. *Experiments in Fluids*, 3(1):53–59, 1985. ISSN 07234864. doi: 10.1007/BF00285271.

W. Ambrosini, P. Andreussi, and B. J. Azzopardi. A Physically Based Correlation for Drop Size in Annular Flow. *International Journal of*

Multiphase Flow, 17(4):497–507, 1991. ISSN 0301-9322. doi: http://dx.doi.org/10.1016/0301-9322(91)90045-5.

Chad M. Winkler and J. E. Peters. Refrigerant droplet size measurements in conjunction with a novel method for improving flow distribution in evaporators. *Aerosol Science and Technology*, 36(6):734–741, 2002. ISSN 02786826. doi: 10.1080/02786820290038429.

J. Steimes and P. Hendrick. Measurement and prediction of droplet size in annular gas–liquid flows in aero-engine oil systems. *International Journal of Multiphase Flow*, 93:84–91, 2017. ISSN 03019322. doi: 10.1016/j.ijmultiphaseflow.2017.03.013.

C. Berna, A. Escrivá, J. L. Muñoz-Cobo, and L. E. Herranz. Review of droplet entrainment in annular flow: Characterization of the entrained droplets. *Progress in Nuclear Energy*, 79:64–86, 2015. ISSN 01491970. doi: 10.1016/j.pnucene.2014.11.011.

Lei Pan and Thomas J. Hanratty. Correlation of entrainment for annular flow in horizontal pipes. *International Journal of Multiphase Flow*, 28(3):385–408, 2002. ISSN 03019322. doi: 10.1016/S0301-9322(01)00074-X.

A. M. Ribeiro, T. R. Bott, and D. M. Jepson. The influence of a bend on drop sizes in horizontal annular two-phase flow. *International Journal of Multiphase Flow*, 27(4):721–728, 2001. ISSN 03019322. doi: 10.1016/S0301-9322(00)00038-0.

Sohail H. Zaidi, A. Altunbas, and B. J. Azzopardi. A comparative study of phase Doppler and laser diffraction techniques to investigate drop sizes in annular two-phase flow. *Chemical Engineering Journal*, 71(2):135–143, 1998. ISSN 13858947. doi: 10.1016/S1385-8947(98)00125-9.

A. Al-Sarkhi and T. J. Hanratty. Effect of pipe diameter on the drop size in a horizontal annular gas-liquid flow. *International Journal of Multiphase Flow*, 28(10):1617–1629, 2002. ISSN 03019322. doi: 10.1016/S0301-9322(02)00048-4.

Mark J.H. Simmons and Thomas J. Hanratty. Droplet size measurements in horizontal annular gas-liquid flow. *International Journal of Multiphase Flow*, 27(5):861–883, 2001. ISSN 03019322. doi: 10.1016/S0301-9322(00)00053-7.

B. J. Azzopardi and S. H. Zaidi. The effect of inclination on drop sizes in annular gas-liquid flow. In *Experimental heat transfer, fluid mechanics and thermodynamics*, volume 2, pages 1169–1176, 1997. ISBN 8846700147.

R. A. Mugele and H. D. Evans. Droplet size distribution in sprays. *Industrial & Engineering Chemistry*, 43(6):1317–1324, 1951. doi: 10.1021/ie50498a023.

K. J. Hay, Zi-Chao Liu, and T. J. Hanratty. Relation of Deposition to Drop Size When the Rate Law is Nonlinear. *International Journal of Multiphase Flow*, 22(5):829–848, 1996.

I. G. Bowen and G. P. Davies. Particle size distribution and the estimation of sauter mean diameter. In *Shell Technical Report No. ICT/28*, 1951.

E. Hurlburt and T. Hanratty. Measurement of drop size in horizontal annular flow with the immersion method. *Experiments in Fluids*, 32(6):692–699, 2002. ISSN 0723-4864. doi: 10.1007/s00348-002-0425-8.

T. Fujimatsu, O. Okada, and Hideomi Fujita. Remarks on extended application of the immersion liquid method for droplet size measurement. *International Journal of Fluid Mechanics Research*, 24(4-6):829–840, 1997. ISSN 2152-5102.

Eo Hwak Lee, Hee Cheon No, Seung Hun Yoo, Kyung Won Lee, and Chul Hwa Song. Freezing technique for measuring and predicting the size of droplets in a horizontal annular flow. *Nuclear Engineering and Design*, 240(7):1795–1802, 2010. ISSN 00295493. doi: 10.1016/j.nucengdes.2010.02.035. URL http://dx.doi.org/10.1016/j.nucengdes.2010.02.035.

Larry B. Fore and Abraham E. Dukler. The distribution of drop size and velocity in gas-liquid annular flow. *International Journal of Multiphase Flow*, 21(2):137–149, 1995. ISSN 03019322. doi: 10.1016/0301-9322(94)00061-N.

David F. Tatterson, John C. Dallman, and Thomas J. Hanratty. Drop sizes in annular gas-liquid flows. *AIChE Journal*, 23(1):68–76, 1977. ISSN 15475905. doi: 10.1002/aic.690230112.

M. Wicks and A. E. Dukler. In situ measurements of drop size distribution in two-phase flow: a new method for electrically conducting liquids. *International Heat Transfer Conference Digital Library*, 3:39–49, 1966. ISSN 2377-424X. doi: 10.1615/IHTC3.400.

Paul Porombka, Stephan Boden, Dirk Lucas, and Uwe Hampel. Horizontal annular flow through orifice studied by X-ray microtomography. *Experiments in Fluids*, 62(1):1–14, 2021. ISSN 14321114. doi: 10.1007/s00348-020-03091-6. URL https://doi.org/10.1007/s00348-020-03091-6.

Ovid Baker. Design of Pipelines for the Simultaneous Flow of Oil and Gas. *Society of Petroleum Engineers*, 1953. doi: https://doi.org/10.2118/323-G. URL https://doi.org/10.2118/323-G.

C.J. Hoogendoorn. Gas-liquid flow in horizontal pipes. *Chemical Engineering Science*, 9(4):205–217, feb 1959. ISSN 0009-2509. doi: 10.1016/0009-2509(59)85003-X. URL https://www.sciencedirect.com/science/article/pii/000925095985003X?via{%}3Dihub.

G W Govier and M M Omer. The horizontal pipeline flow of air-water mixtures. *The Canadian Journal of Chemical Engineering*, 40(3):93–104, 1962. doi: 10.1002/cjce.5450400303. URL https://onlinelibrary.wiley.com/doi/abs/10.1002/cjce.5450400303.

J. M. Mandhane, G. A. Gregory, and K. Aziz. A flow pattern map for gas-liquid flow in horizontal pipes. *International Journal of Multiphase Flow*, 1 (4):537–553, 1974. ISSN 03019322. doi: 10.1016/0301-9322(74)90006-8.

Y. Taitel and A.E. Dukler. A theoretical approach to the Lockhart-Martinelli correlation for stratified flow. *International Journal of Multiphase Flow*, 2(5-6):591–595, apr 1976. ISSN 0301-9322. doi: 10.1016/0301-9322(76)90019-7. URL https://www.sciencedirect.com/science/article/pii/0301932276900197.

Ran Kong and Seungjin Kim. Characterization of horizontal air–water two-phase flow. *Nuclear Engineering and Design*, 312:266–276, 2017. ISSN 00295493. doi: 10.1016/j.nucengdes.2016.06.016. URL http://dx.doi.org/10.1016/j.nucengdes.2016.06.016.

Mahesh J Vaze and Jyotirmay Banerjee. Prediction of Liquid Height for Onset of Slug Flow. *The Canadian Journal of Chemical Engineering*, 90:1295–1303, 2012. doi: 10.1002/cjce.20626.

Jignesh Thaker and Jyotirmay Banerjee. Characterization of two-phase slug flow sub-regimes using flow visualization. *Journal of Petroleum Science and Engineering*, 135:561–576, 2015. ISSN 09204105. doi: 10.1016/j.petrol.2015.10.018. URL http://dx.doi.org/10.1016/j.petrol.2015.10.018.

Chapter 4

Frictional pressure gradient

4.1. Previous studies

4.1.1. Gas-liquid correlations

One of the seminal works regarding multiphase flows was carried out by Lockhart and Martinelli [1949]. They developed a correlation to calculate the FPG of liquid-gas mixtures in horizontal pipelines. The main idea was to determine the FPG of the mixture by calculating it as a single phase, as if each phase was flowing separately in the pipeline, and then apply a correction. The L-M correlation has been used both in the industry and in many research works, mainly because of its simplicity and its ability to predict reliably the value of the pressure drop. Since their study, several authors have validated the correlation Dukler et al. [1964], Mao et al. [1997], Abduvayt et al. [2003]. In particular Beggs and Brill [1973] proposed a more general correlation for pipelines with any inclination angle.

Lockhart-Martinelli Correlation

The main insight in Lockhart and Martinelli [1949] correlation was to determine the FPG of the mixture as if each phase were flowing separately in the pipeline. Then, these values are corrected by the two phase multipliers, Φ_f and Φ_g eq. (4.1). The assumption is that for each phase, there must be a set of hydraulic diameter, phase velocity and friction factor that results in the two-phase frictional pressure gradient. The analysis leads to the postulation that Φ_f and Φ_g are functions of the gas and liquid Reynolds numbers and

the Lockhart-Martinelli (L-M) parameter X, defined in eq. (4.3). Empirical curves, for use in design, were obtained from a wide range of experimental data to calculate the multiphase multiplier.

$$\left(\frac{\delta P}{\delta z}\right)_{TP} = \Phi_f^2 \cdot \left(\frac{\delta P}{\delta z}\right)_f = \Phi_g^2 \cdot \left(\frac{\delta P}{\delta z}\right)_g \tag{4.1}$$

$$\Phi_f^2 = f(Re_f, Re_g, X) \tag{4.2}$$

$$X = \frac{\left(\delta P/\delta z\right)_f}{\left(\delta P/\delta z\right)_g} \tag{4.3}$$

Here $(\delta P/\delta z)_f$ is the frictional pressure drop, calculated with the liquid properties and superficial velocity, the same applies for the sub-index g. Note that in eq. (4.1) the FPG_{TP} can be calculated with any of both FPG liquid or gas, as they are equivalent.

Chisholm simplification

Chisholm [1967] examined deeper Lockhard and Martinelli's work, and proposed a simple equation, for design in engineering, relating the multiphase multipliers with the Lockhart-Martinelli parameter, X eq. (4.4).

$$\Phi_f^2 = 1 + C/X + 1/X^2 \tag{4.4}$$

Here, C is a flow regime indicator, it might adopt four different values regarding the flow mechanism of the phases, as it quantifies to what extent the liquid or gas flow in a turbulent way (t) or in viscous way (v).

$$C = \begin{cases} 5, & \text{if } Re_f < 2000 \text{ and } Re_g < 2000 \ (v-v) \\ 10, & \text{if } Re_f \geq 2000 \text{ and } Re_g < 2000 \ (t-v) \\ 12, & \text{if } Re_f < 2000 \text{ and } Re_g \geq 2000 \ (v-t) \\ 20, & \text{if } Re_f \geq 2000 \text{ and } Re_g \geq 2000 \ (t-t) \end{cases} \tag{4.5}$$

Dukler et al. correlation

Dukler et al. [1964] developed a correlation for predicting the pressure gradient in pipelines. Their study was grounded through the principles of dynamic similarity for two-phase (G/L) flows assuming that kinematic

similarity applies to the single phase velocities as it does to the mixture velocities. They found that if dynamic similarity is to exist, then the mixture properties must be defined for the non-slip homogeneous flow:

$$\rho_{ns} = \rho_f \cdot \lambda + \rho_g \cdot (1 - \lambda) \tag{4.6}$$

$$\mu_{ns} = \mu_f \cdot \lambda + \mu_g \cdot (1 - \lambda) \tag{4.7}$$

With this the Reynolds number for the mixture can be calculated as:

$$Re_{gf} = \frac{\rho_{ns} j_M D}{\mu_{ns}} \cdot \beta \tag{4.8}$$

Where β corrects the properties from the non-slip condition to the actual slippage of the mixture, it is expressed as:

$$\beta = \frac{\rho_f \cdot \lambda^2}{\rho_{ns} \cdot (1 - \bar{\alpha})} + \frac{\rho_g \cdot (1 - \lambda)^2}{\rho_{ns} \cdot \bar{\alpha}} \tag{4.9}$$

The frictional pressure drop is then calculated as:

$$\left(\frac{\delta P}{\delta z}\right)_{gf} = \frac{\rho_{ns} \nu_M^2 f_f}{2D} \cdot \epsilon(\lambda) \cdot \beta \tag{4.10}$$

Where $\epsilon(\lambda)$ is the correlation found by Dukler et al. [1964] that represents the ratio between the multi-phase friction factor and the single-phase friction factor, given by:

$$\epsilon(\lambda) = \frac{f_m}{f_f} = 1 + \frac{z}{1.281 - 0.478 \cdot z + 0.444 \cdot z^2 - 0.094 \cdot z^3 + 0.00843 \cdot z^4} \tag{4.11}$$

where $z = -ln\ \lambda$

Beggs & Brill correlation

Beggs and Brill [1973] developed a correlation for Gas-Liquid mixtures flowing in inclined pipes. They observed a lack of literature to predict the behaviour of gas-liquid mixtures in inclined pipelines together with an increasing number of inclined wells trying to reach for petroleum in unexplored areas. With this in mind they did a large campaign of almost 600 measurements in an experimental rig, studying the effect of 8 parameters:

(1) gas flow rate: 0 – 98 m^3/s; (2) liquid flow rate: 0 – 1.9 lt/s; (3) average system pressure 241- 655 kPa; (4) pipe diameter 25.4 and 38.1 mm; (5) liquid hold up 0 – 0.87 %; (6) pressure gradient 0 – 2.6 Pa/m; (7) inclination angle -90º to +90º; and (8) flow pattern. The equation used to calculate the pressure gradient for any mixture of gas and liquid flowing in a pipeline of internal diameter D and inclination angle θ is:

$$\left(\frac{\delta P}{\delta z}\right)_{gf} = \frac{\rho_{gf}\left[g \cdot sin(\theta) + (f_{gf} \cdot j_M^2/2D)\right]}{1 - \left[(\rho_{gf} \cdot j_M \cdot j_g)/P\right]} \tag{4.12}$$

where ρ_{gf} is the density of the two-phase mixture:

$$\rho_{gf} = \rho_f \cdot H_f + \rho_g \cdot (1 - H_f) \tag{4.13}$$

eq. (4.12) contains two unknowns: H_f the liquid hold-up used to calculate the in-situ mixture density; and f_M the friction factor of the mixture to calculate friction losses. In their study Beggs and Brill proposed correlations for predicting H_f and f_{gf} from fluid and systems properties that are known. First they propose a method to identify the flow pattern between segregated, intermittent and distributed. For this L_1 and L_2 are defined in eqs. (4.14) and (4.15) and from the inequalities 4.17 to 4.19.

$$L_1 = exp(-4.62 - 3.757 \cdot Z - 0.481 \cdot Z^2 - 0.0207 \cdot Z^3) \tag{4.14}$$

$$L_2 = exp(1.061 - 4.602 \cdot Z - 1.609 \cdot Z^2 - 0.179 \cdot Z^3 + 0.635 \times 10^3 \cdot Z^5) \tag{4.15}$$

where Z is a function of the inlet flow rates:

$$Z = ln\left(\frac{Q_{fo}}{Q_{fo} + Q_{go}}\right) \tag{4.16}$$

$$\text{If } Fr < L_1, \text{ the flow is segregated} \tag{4.17}$$

$$\text{If } L_1 < Fr < L_2, \text{ the flow is intermittent} \tag{4.18}$$

$$\text{If } Fr > L_1, \text{ and } Fr > L_2 \text{ the flow is distributed} \tag{4.19}$$

The friction factor of the two-phase mixture was found to be a function of the input hold-up and the in-situ hold-up:

$$\frac{f_{gf}}{f_{ns}} = f\left(\lambda/H_f^2\right) = e^S \tag{4.20}$$

$$S = \left[\frac{ln(y)}{-.0523 + 3.182 \cdot ln(y) - 0.8725 \cdot ln(y)^2 + 0.01853 \cdot ln(y)^4}\right] \tag{4.21}$$

$$y = \frac{\lambda}{H_f^2} \tag{4.22}$$

In section 5.1.2 is detailed the method to calculate H_f.

4.1.2. Liquid-Solid correlations

Regarding liquid-solid mixtures, there is a great deal of experimentation on slurry flows, because this type of flows are very frequent in the chemical industry, including manufacturing of pharmaceuticals, nano-fabrication, and oil refining among others. It is also applicable to long distance transport of materials like coal or waste tailings. In many cases hydrodynamic transport of solids can be both, more energy-efficient and have lower operating and maintenance costs than other handling methods. Most of the insights on slurry flows came from Gillies et al. [1997], Gillies and Shook [2000], Gillies et al. [2004], Wilson and Sellgren [2003] which classified the slurries in two types: (1) homogeneous or non-settling slurries, and (2) heterogeneous or settling slurries. For the scope of the present research, considering the solid particles used in the facility, the focus is set on heterogeneous slurries. Gillies et al. [2004] proposed the "*SRC Two-Layer model*", where the velocity and concentration distributions are approximated by step functions. This is because the particles are assumed to be concentrated mainly in the lower layer with the maximum concentration, while in the upper layer particles are uniformly distributed and suspended by turbulence, with a lower concentration.

The focus of this research is on heterogeneous slurries. These are composed of coarser particles that segregate in the quiescent state and do not flocculate. Also, these slurries usually exhibit approximately a Newtonian behaviour, and so the ratio between the viscosity of the slurry and the viscosity of the fluid can be considered a function of particle shape and solids concentration. Turbulence is the main suspension mechanism of the particles and at low velocities a stationary bed is formed.

In Gillies et al. [2004] heterogeneous slurries flowing at high velocities

were studied using the SRC two-layer model Gillies and Shook [2000], and incorporating improvements from Wilson and Sellgren [2003]. They divide the system into three superimposed layers. Each layer contribute individually to the frictional pressure drop. The three layers are: the finer particles, which together with the liquid form a carrier fluid of higher density and viscosity; coarse particles that are suspended by the flow turbulence; and particles that are not suspended and constitute a sliding bed. In this paper only heterogeneous flows are analysed, which are composed of particles from the second category. Accordingly, the frictional pressure gradient is calculated using eq. (4.23) and the wall shear stress, which is kinematic, is calculated with eq. (4.24)

$$-\left(\frac{dP}{dz}\right)_{fs} = \frac{\tau_w S}{A} = \frac{4\tau_w}{D} \tag{4.23}$$

$$\tau_w = \frac{j_{fs}^2}{8}\left(\rho_f f_f + \rho_s f_s\right) \tag{4.24}$$

In eq. (4.23) D, S and A are the diameter, perimeter and area of the transverse section of the pipeline respectively. In eq. (4.24) j_{fs} is the slurry velocity, ρ_f and ρ_s are the liquid and particle densities, f_f is the Darcy-Weisbach friction factor for the liquid flowing at the slurry velocity. Finally f_s is the particle friction factor, which can be computed using eq. (4.25), is a function of the linear concentration λ, eq. (4.26), and the dimensionless particle diameter d^+, eq. (4.27). The linear concentration can be considered a measure of the ratio of the particle diameter to the shortest distance between neighbouring particles.

$$f_s = 0.00132 \cdot \lambda^{1.25}\left[0.15 + e^{-01.d^+}\right] \tag{4.25}$$

$$\lambda = \left[\left(\frac{C_{max}}{C_s}\right)^{1/3} - 1\right]^{-1} \tag{4.26}$$

$$d^+ = \frac{d \cdot j_{fs}\sqrt{f_f/8}}{\nu_f} \tag{4.27}$$

Several authors studied the frictional pressure gradients of slurries and the SRC two-layer model has shown good accuracy. However, in most of

these studies, the analyzed slurries are composed of particles much denser than the fluid. Stutz et al. [2000] investigated the friction factor for slurries of particles with density close to that of the water, for analysing solid-liquid coolant systems. Later, Edelin et al. [2015] studied the energy optimum for the transport of floating particles in pipelines. To predict the behaviour of slurries with floating particles there are mainly two approaches. The first one is by empirical correlations, based on dimensional analysis where coefficients ($\alpha, \beta, \gamma, \delta$ and ϵ) in eq. (4.28) are determined experimentally.

$$f - f_f = \epsilon \cdot C^{\alpha} \cdot f_w^{\beta} \cdot C_D^{\gamma} \cdot \left(\frac{j_{fs}^2}{D \cdot g \cdot \left(1 - \frac{\rho_s}{\rho_f}\right)} \right)^{\delta} \tag{4.28}$$

The second approach is the use of models of effective liquid where the liquid-solid mixture is modelled by layers in which different effective properties of fluid correspond to each layer. Many researchers have proposed correlations to estimate the effective density and viscosity considering the shape, size and particle arrangements, as well as the fluid in which they are flowing.

4.1.3. Three-phase (G/L/S) correlations

Three-phase flows have been reviewed in Rahman et al. [2013]. These authors present a summary of the most important studies and their insights including the research from Scott and Rao [1971], this study has been the first to propose that the Lockhart-Martinelli correlation can be modified to analyse three-phase flows in horizontal pipelines. This insight is advantageous because with the modified L-M correlation, predictions of the mixture FPG can be obtained even if the flow regime is not known, this was not the case in previous three-phase correlations.

The modified Lockhart-Martinelli correlation proposed in Scott and Rao [1971], and later developed in Hatate et al. [1986], Gillies et al. [1997], estimates the FPG of the three-phase flows by assuming that the slurry FPG can be used instead of the liquid pressure drop in the original correlation. In the work of Scott and Rao [1971] a good correlation performance was obtained using the Durand correlation for calculating the slurry friction gradient. However, the latter correlation is known to provide an accurate prediction only when solid concentration is under 15%. In the study of Hatate et al. [1986] experimental data were correlated within a 30% error but only for small particles ($d <$

$100\mu m$). This denotes the need of an accurate and general estimation of the slurry FPG in order to apply the modified Lockhart-Martinelli correlation.

In summary, in this study, the modified Lockhart-Correlation is used to predict the FPG of three-phase flows where the properties of the slurry are first modified according to the two-layer model Gillies and Shook [2000], assuming that only coarse particles suspended by turbulence are present in the liquid phase. In this way, the LM parameter (X) in eq. (4.3) is calculated with the FPG of the slurry.

$$X^2 = \frac{\left(\delta P/\delta z\right)_{fs}}{\left(\delta P/\delta z\right)_{g}} \tag{4.29}$$

Here $(\delta P/\delta z)_{fs}$ is calculated following Equations (4.23) to (4.27). Then, the multi-phase multiplier (Φ_{fs}) is calculated with eq. (4.4), and finally, the FPG for three phase flows is obtained by modifying eq. (4.1):

$$\left(\frac{\delta P}{\delta z}\right)_{gfs} = \Phi_{fs}^2 \cdot \left(\frac{\delta P}{\delta z}\right)_{fs} \tag{4.30}$$

4.1.4. Summary of correlations

Table 4.1: Available correlations for the FPG in horizontal gas-liquid two phase flow.

Literature	$(\delta P/\delta z)_M$	Flow regime
Lockhart and Martinelli [1949]	$\Phi_i^2 \cdot (\frac{\delta P}{\delta z})_i$	$(v-v)$; $(v-t)$ $(t-v)$; $(t-t)$
Chisholm [1967]	$\Phi_i^2 \cdot (\frac{\delta P}{\delta z})_i$; $\Phi_f^2 = 1 + C/X + 1/X^2$	$(v-v)$; $(v-t)$ $(t-v)$; $(t-t)$
Dukler et al. [1964]	$\frac{\rho_{ns} v_{gf}^2 f_f}{2D} \cdot \epsilon(\lambda) \cdot \beta$	-
Beggs and Brill [1973]	$\frac{\rho_{gf}\left[g \cdot sin(\theta) + \left(f_{gf} \cdot v_{gf}^2/2D\right)\right]}{1 - \left[\left(\rho_{gf} \cdot v_{gf} \cdot j_g\right)/P\right]}$	segregatted, intermittent, distributed

4.2. Experimental Results

In this section, experimental results for two and three-phase flows are presented. The data was collected at LESLIE flow loop in two experimental campaigns. The acquisition process and the summary of both datasets together with the corresponding calibrations and notes are given in appendices A.1 and A.2. So as to focus this section on the presentation and discussion of the results.

4.2.1. Gas-liquid two-phase flow

Here, the data set # 1 is analysed. A summary of the performed measurements during the experimental campaign is listed in table A.1. The data is compared with three correlations, (*i*) Lockhart and Martinelli (L-M), (*ii*) Beggs & Brill (B&B) and (*iii*) Duckler et al. (Dk). In fig. 4.1 the performance of the three correlations are plotted together. By plotting the measured values vs. the predicted values it is notorious how the L-M correlation predicts much better the frictional pressure drop, with an average absolute percent deviation of 10% using the recommended C parameter from the Chisholm simplification, and 6.2% with the fitted value of C. The Dk correlation underestimates the pressure drop with very large differences with respect to LM and B&B, this is in concordance with the studies of Rahman et al. [2013].

The B&B correlation over-estimates the pressure drop, however, for plug flow, the L-M correlations underestimates the frictional pressure drop, while the B&B correlations predicts it within $\pm$ 10%, as it can be seen in fig. 4.1 where the plug flow runs are identified with filled symbols, for both, the Lockhart-Martinelli and Beggs & Brill correlations. The statistical analysis over each correlation is summarized in table 4.2.

When applying the Chisholm simplification to the Lockhart-Martinelli correlation, the correct value of the parameter C, from eq. (4.4), must be chosen according to the gas and liquid Reynolds numbers. Chisholm [1967] proposed a value of $C = 20$ for mixtures flowing in turbulent-turbulent regime. In fig. 4.2 the multi-phase multiplier (Φ_f), calculated with the experimental data, is plotted against the Lockhart and Martinelli parameter (X), together with the curves for predicting the multi-phase multiplier with values of $C = 20$ and $C = 25$, as this last value was suggested by Talley et al. [2015], Kong et al.

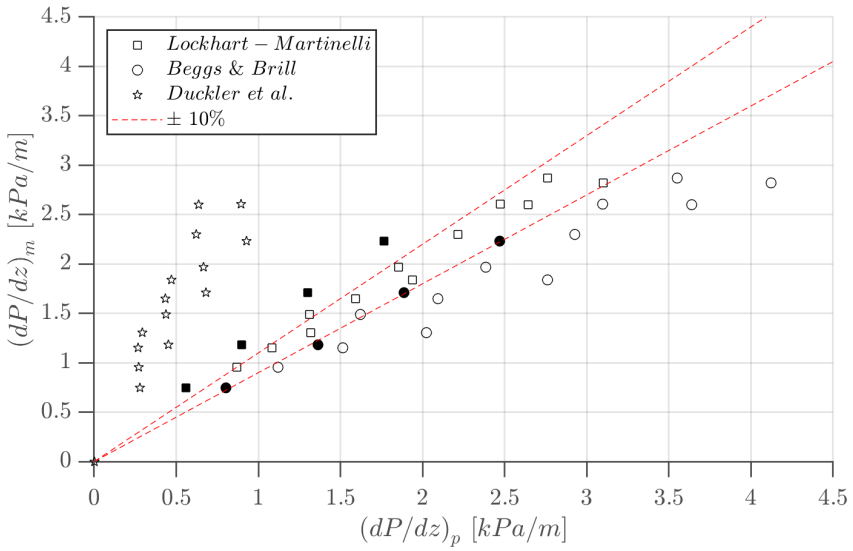

Figure 4.1: Performance of several frictional pressure gradient correlations against experimental data, filled symbols represent plug flow tests.

[2017]. The red dashed curve is the fitted curve for the present experimental data, and corresponds to a curve with $C = 21$. The average absolute disagreement of the experimental data for $C = 20$, $C = 25$ and $C = 21$ are 3.5, 4.4 and 3.2 % respectively as listed in table 4.2 together with the rest of the statistical parameters, defined in appendix B. It can be noted that for slug flow, larger values of the multiplier are obtained, this means that the increment of the gas flow rate has a big impact in the pressure drop. The two-phase pressure drop is calculated as the product of the multi-phase multiplier and the frictional pressure drop of the liquid phase, as indicated in eq. (4.1).

Table 4.2: Performance of tested correlations

FPG Correlation	APD [+ %]	APD [- %]	AAPD [%]	RMSPD [%]
Lockhart and Martinelli [1949]				
• $C = 20$	4.5	11.9	10.0	13
• $C = 21$	7.8	5.7	6.2	7.3
Beggs and Brill [1973]	25.7	-	25.7	29.5
Dukler et al. [1964]	-	69	69.1	69.4
$\Phi_f = 1 + C/X + 1/X$				
$C = 20$	2.2	4.0	3.5	4.0
$C = 25$	5.4	2.2	4.4	5.5
C =fitted	3.8	2.9	3.2	3.7

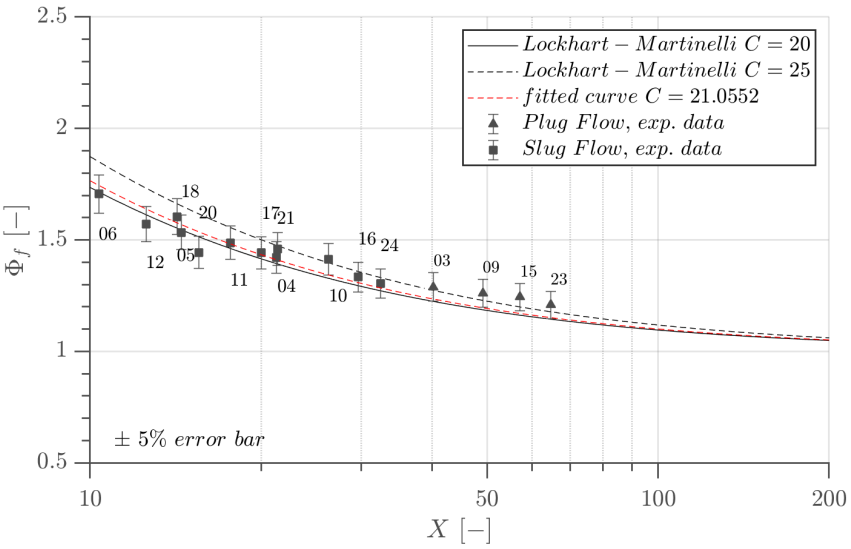

Figure 4.2: Multiphase mutltiplier against Lockhard-Martinelli parameter

4.2.2. Gas-liquid-solid three-phase flow

To calculate the frictional pressure drop the modified L-M correlation has been used. In this correlation the slurry (L/S) is treated as the 'liquid' phase, but correcting the physical properties of the slurry as proposed by the Saskatchewan Research Council's Pipe Flow Technology Centre. For this analysis 72 setting were tested, the summary of the measurements is presented in table A.2. Measurements of pressure drop for two and three-phase flows are plotted together in fig. 4.3 against the air superficial velocity (j_g). Circles stand for two-phase runs, triangles and squares for three-phase runs with 5 ($C_s = 0.05$) and 10% ($C_s = 0.1$) solid loading respectively. The continuous lines represent the predictions obtained by applying the L-M correlation for the different liquid superficial velocities, and the dotted lines are obtained by applying the modified L-M correlation for three-phase flows with 10% loading of solids. Finally, the colors of the curves and markers indicate the liquid (or slurry in 3-phase flows) superficial velocity, $j_f = 1.06$, $j_f = 1.41$ and $j_f = 1.69$ m/s are represented by blue, red and green colors respectively.

Note that the curves corresponding to the same liquid or slurry superficial velocities of two and three-phase ($C_s = 0.1$) flows are in close proximity, as a 10% load of solid particles, of such density, barley induces an effect on the frictional pressure drop. This is also noticeable by looking at the experimental data. Circles, triangles and squares fit the theoretical curves

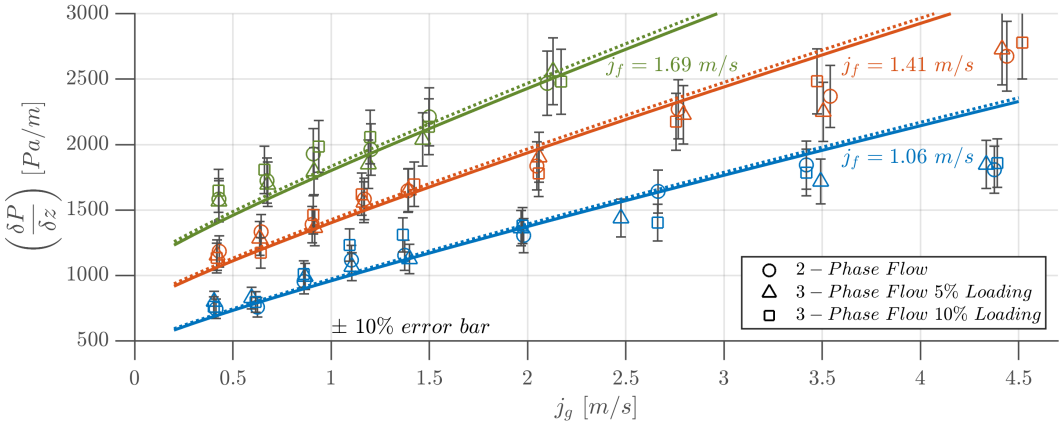

Figure 4.3: Performance of the Modified Lockhart-Martinelli correlation

quite well. Although the theoretical curves fit the experimental data relatively well, a general tendency to sub-estimate the pressure drop for lower values of superficial gas velocity (j_g) and over-estimate it for higher values of j_g is appreciable.

When applying the Chisholm [1967] simplification, the multi-phase multiplier can be plotted as a function of the L-M parameter, X. In two-phase flows, X is calculated with eq. (4.3) using the liquid and gas superficial velocities, while in three-phase flows the slurry and gas superficial velocities are used. This means that the difference for two and three-phase flows stands in how the liquid or slurry frictional pressure drops are calculated, and so, once X is calculated, both phases can be plotted together in a $\Phi(X)$ plot. This is shown in fig. 4.4, the experimental data is plotted together with the predicted values using two values of C. The shape of the markers indicate the flow regime of the run where triangles, diamonds and squares represent Plug, transition and Slug flows respectively. The color of the markers refers to the type of flow. In this way blue, red and green stands for two-phase, three-phase with 5% and 10% of solid concentration respectively. The black plotted curves are the predicted values of Φ by applying the Chisholm simplification, the continuous one is obtained with a value of $C = 20$ which is the original proposed value of C for mixtures flowing in a turbulent-turbulent regime. Using $C = 25$, a value proposed by some authors in the literature Talley et al. [2015], Kong and Kim [2017], results in the dashed line. Finally, the experimental data has also been fitted obtaining a value of $C = 19$. This denotes that the LM and modified-LM correlations perform well for both, two-phase and three-phase

flows respectively.

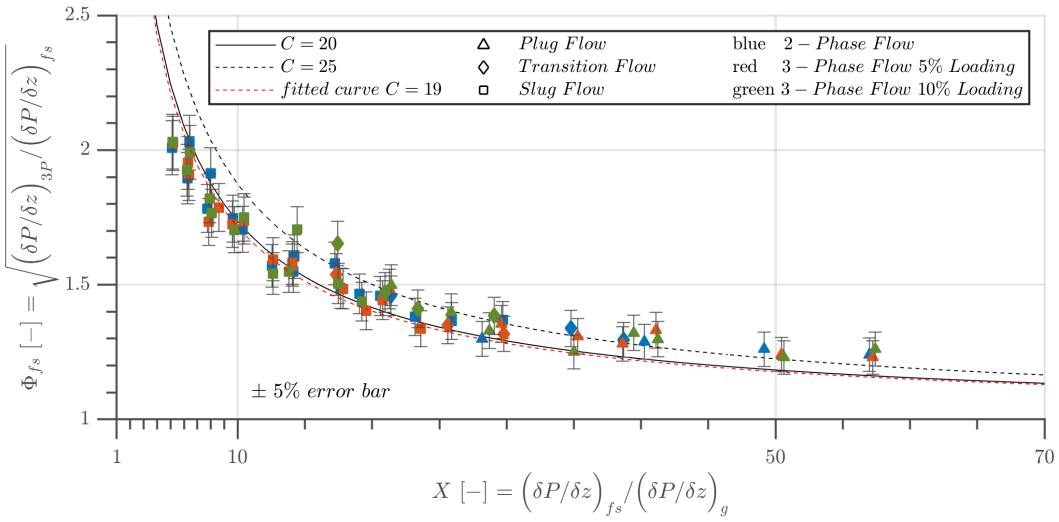

Figure 4.4: Multiphase mutltiplier against Lockhard-Martinelli parameter

The experimental data has also been fitted obtaining the red dashed line that corresponds to a value of $C = 19$. Finally, the average absolute difference of the experimental data with the curves in fig. 4.4 for $C = 20$, $C = 25$ and $C = 21$ are 4 %, 6 % and 4 % respectively This denotes that the LM and modified-LM correlations performs well for both, two-phase and three-phase flows respectively.

4.3. Bibliography

R.W. Lockhart and R.C. Martinelli. Proposed correlation of data for isothermal two-phase, two-component flow in pipes. *Chemical Engineering Progress*, 45(1):39–48, 1949. ISSN 03607275. doi: http://dx.doi.org/10.1016/0017-9310(67)90047-6.

A. E. Dukler, Moye Wicks, and R. G. Cleveland. Frictional pressure drop in two-phase flow: An approach through similarity analysis. *American Institute of Chemical Engineers Journal*, 10(1):44–51, 1964. ISSN 0001-1541. doi: 10.1002/aic.690100118. URL http://doi.wiley.com/10.1002/aic.690100118.

F. Mao, F. K. Desir, and M. A. Ebadian. Pressure drop measurment and

correlation for three-phase flow of simulated nuclear waste in a horizontal pipe. *International Journal of Multiphase Flow*, 23(2):397–402, 1997.

Plat Abduvayt, Norio Arihara, Ryo Manabe, and Kenji Ikeda. Experimental and modeling studies for gas-liquid two-phase flow at high pressure conditions. *Journal of the Japan Petroleum Institute*, 46(2):111–125, 2003. ISSN 13468804. doi: 10.1627/jpi.46.111. URL http://joi.jlc.jst.go.jp/JST.JSTAGE/jpi/46.111?from=CrossRef.

H. Dale Beggs and James P. Brill. A study of two-phase flow in inclined pipes. *Journal of Petroleum Technology*, 25(5):607–617, 1973.

D. Chisholm. A theoretical basis for the Lockhart-Martinelli correlation for two-phase flow. *International Journal of Heat and Mass Transfer*, 10:1767–1778, 1967.

R.G. Gillies, M.J. McKibben, and C. A. Shook. Pipeline Flow of Gas, Liquid and Sand Mixtures at Low Velocities. *Journal of Canadian Petroleum Technology*, 36(9), 1997.

R. G. Gillies and C. A. Shook. Modelling high concentration slurry flows. *Canadian Journal of Chemical Engineering*, 78(August):709–716, 2000. ISSN 00084034. doi: 10.1002/cjce.5450780413.

R. G. Gillies, C. A. Shook, and J. Xu. Modelling Heterogeneous Slurry Flows at High Velocities. *Canadian Journal of Chemical Engineering*, 82(October): 1060–1065, 2004. ISSN 00084034. doi: 10.1002/cjce.5450820523.

K C Wilson and A Sellgren. Interaction of Particles and Near-Wall Lift in Slurry Pipelines. *Journal of Hydraulic Engineering*, 129(January):73–76, 2003. ISSN 07339429. doi: 10.1061/(ASCE)0733-9429(2003)129:1(73).

B Stutz, P Reghem, and O Martinez. Flow of Slurries of Particles With Density Close To That of Water. In *Second Workshop on Ice Slurries of IIF/IIR*, pages 1–12, 2000.

Denis Edelin, Pierre Clement Czujko, Cathy Castelain, Christophe Josset, and Francine Fayolle. Experimental determination of the energy optimum for the transport of floating particles in pipes. *Experimental Thermal and Fluid Science*, 68:634–643, 2015. ISSN 08941777. doi: 10.

1016/j.expthermflusci.2015.06.018. URL http://dx.doi.org/10.1016/j.expthermflusci.2015.06.018.

M. A. Rahman, K. Freeman Adane, and R. Sean Sanders. An improved method for applying the Lockhart-Martinelli correlation to three-phase gas-liquid-solid horizontal pipeline flows. *Canadian Journal of Chemical Engineering*, 91(8):1372–1382, 2013. ISSN 00084034. doi: 10.1002/cjce.21843.

D. S. Scott and P. K. Rao. Transport of Solids by Gas-Liquid Mixtures in Horizontal Pipes. *Canadian Journal of Chemical Engineering*, 49:302–309, 1971. ISSN 0722-1819.

Yasuo Hatate, Hiroshi Nomura, Takanori Fujita, Shuichi Tajiri, and Atsushi Ikari. Gas Holdup and Pressure Drop in Three-Phase Horizontal Flows of Gas-Liquid-Fine Solid Particles System. *Journal of Chemical Engineering of Japan*, 19(4):330–335, 1986. ISSN 00219592. doi: 10.1252/jcej.19.330.

Justin D. Talley, Ted Worosz, and Seungjin Kim. Characterization of horizontal air–water two-phase flow in a round pipe part II: Measurement of local two-phase parameters in bubbly flow. *International Journal of Multiphase Flow*, 76:223–236, 2015. ISSN 03019322. doi: 10.1016/j.ijmultiphaseflow.2015.06.012. URL http://dx.doi.org/10.1016/j.ijmultiphaseflow.2015.06.012.

Ran Kong, Seungjin Kim, Stephen Bajorek, Kirk Tien, and Chris Hoxie. Experimental investigation of horizontal air–water bubbly-to-plug and bubbly-to-slug transition flows in a 3.81 cm ID pipe. *International Journal of Multiphase Flow*, 94:137–155, 2017. ISSN 03019322. doi: 10.1016/j.ijmultiphaseflow.2017.04.020. URL http://dx.doi.org/10.1016/j.ijmultiphaseflow.2017.04.020.

Ran Kong and Seungjin Kim. Characterization of horizontal air–water two-phase flow. *Nuclear Engineering and Design*, 312:266–276, 2017. ISSN 00295493. doi: 10.1016/j.nucengdes.2016.06.016. URL http://dx.doi.org/10.1016/j.nucengdes.2016.06.016.

Chapter 5

Void Fraction

The void fraction is a very important feature of multiphase flows, as it is directly related with the gas-liquid interface. There are mainly two different approaches available to predict the void fraction of GL two-phase flows, namely the two fluid (separate) flow model and the one dimensional drift flux model. According to Vijayan et al. [2000], the two fluid flow model can be divided in three groups. The first group is based on the the slip ratio, which uses empirical relations to predict the slippage between the phases, the second group uses a corrector factor to adjust homogeneous models, and the last is called miscellaneous correlations, these are empirical correlations that do not fit in any of the two previous groups.

5.1. Previous studies

In this study some of these correlations are chosen and then compared with the experimental data. From the two fluid flow model, the Lockhart and Martinelli, and Beggs and Brill correlations are chosen, while from the drift flux model four correlations have been selected.

5.1.1. Lockhart and Martinelli void fraction correlation

The Lockhart-Martinelli correlation for void fraction, eq. (5.1), is in the group of miscellaneous models, but it is very similar to the models based in the slip ratio model. The last ones being in the form of eq. (5.2), and each model specifies an empirical equation for the slip ratio, S.

$$\alpha = \left[1 + 0.28(1/x - 1)^{0.64} \left(\rho_g/\rho_l\right)^{0.36} \left(\mu_l/\mu_g\right)^{0.07}\right]^{-1} \tag{5.1}$$

$$\alpha = \left[1 + \{(1-x)/x\} \left(\rho_g/\rho_f\right) S\right]^{-1} \tag{5.2}$$

5.1.2. Beggs & Brill

The work of Beggs and Brill [1973] also includes correlations for predicting the liquid hold-up in two phase flows for all conditions and any inclination angle. eq. (5.3) determines the liquid Hold-up for a pipe inclined θ degrees, where $H_f(0)$, the liquid Hold-up for horizontal pipelines, and the coefficient C can be both calculated with equations from table 5.1.

$$H_f(\theta) = H_f(0) \cdot \left[1 + C \cdot \left[sin(1.8 \cdot \theta) - 1/3 \cdot sin^3(1.8 \cdot \theta)\right]\right] \tag{5.3}$$

Table 5.1: Equations for predicting liquid hold-up.

Flow pattern	Horizontal Hold-up	C (upward)	C (downward)
Segregated	$\frac{0.98 \cdot \lambda^{0.4846}}{Fr^{0.0868}}$	$(1-\lambda) \cdot ln\left[\frac{0.011 \cdot Lv^{3.539}}{\lambda^{3.768} \cdot Fr^{1.614}}\right]$	$(1-\lambda) \cdot ln\left[\frac{4.7 \cdot Lv^{0.1244}}{\lambda^{0.3692} \cdot Fr^{0.5056}}\right]$
Intermittent	$\frac{0.845 \cdot \lambda^{0.5351}}{Fr^{0.0173}}$	$(1-\lambda) \cdot ln\left[\frac{2.96 \cdot \lambda^{0.305} \cdot Fr^{0.0978}}{Lv^{0.4473}}\right]$	Same as segregated
Distributed	$\frac{1.065 \cdot \lambda^{0.5824}}{Fr^{0.0609}}$	0	Same as segregated

L_v - Liquid velocity number $= j_f \left(\rho_f/\rho_g\right)^{0.25}$
Fr - Froude number $= v_{gf}^2/gD$

5.1.3. One-dimensional drift-flux model

The drift flux model was first developed by Zuber and Findlay [1965], since then several authors have contributed to its development. The model is being very accepted for its simplicity and flexibility over the two fluid flow model, it is the prediction approach with more methods proposed to date. The drift flux model determines the void fraction as expressed in eq. (5.4)

$$\langle\alpha\rangle = \frac{\langle j_g\rangle}{C_o\left(\langle v_{gf}\rangle\right) + \langle\langle v_{gm}\rangle\rangle} \tag{5.4}$$

The distribution parameter C_o and the drift velocity v_{gm} are calculated using eqs. (5.5) and (5.6) respectively.

$$C_o = \frac{\langle \alpha \cdot v_{gf} \rangle}{\langle \alpha \rangle \langle v_{gf} \rangle} \tag{5.5}$$

$$\langle\langle v_{gm} \rangle\rangle = \frac{\langle \alpha \cdot v_{gm} \rangle}{\langle \alpha \rangle} = \frac{\langle \alpha \left(v_g - v_{gf} \right) \rangle}{\langle \alpha \rangle} \tag{5.6}$$

In eqs. (5.4) to (5.6) the angle-angle brackets indicate the cross sectional averaged flow properties and the double angle brackets stands for void weighted cross sectional area averaged flow properties. The distribution parameter accounts for the distribution of the gas phase across the pipe cross section, and the drift velocity is the relative velocity of the gas phase with respect to the two-phase mixture velocity v_{gf}. These parameters (C_o) and (v_{gm}) have been the focus of several authors in the literature as they are used to calculate the void fraction. Bhagwat and Ghajar [2014] analyzed several correlations for calculating the distribution parameter and the drift velocity and also proposed a new correlation, then they compared the performance of the correlations against 8255 experimental data points, where 3845 corresponded to air-water two-phase flow experiments. In table 5.2 are listed some of the correlations with the best performance in Bhagwat and Ghajar [2014].

According to eqs. (5.4) to (5.6), the one dimensional drift flux model predicts the cross sectional averaged void fraction. However, the equality between the cross sectional and volumetric void fraction is valid for two-component two-phase flow (non-boiling), as in this case the cross sectional distribution of the gas phase with respect to the liquid phase remains invariable over a relatively short length of pipe. Therefore, the void fraction can be expressed in both ways $\langle \alpha \rangle = \alpha$, and with similar arguments, it is applicable for the rest of the quantities in eqs. (5.4) to (5.6).

5.2. Experimental results

The void fraction measurements are also compared with the correlations of chapter 5, assuming that $\langle \alpha \rangle = \alpha$ for two-component two-phase flows. It can be seen in fig. 5.1 the performance of the predictions against the measured void fraction. The best agreement is achieved by the Lockhart-Martinelli

Table 5.2: Parameters of the drift flux analysis

Correlation	Distribution parameter	Drift velocity [m/s]
Bhagwat and Ghajar [2014] [a]	$\frac{2-(\rho_g/\rho_f)^2}{1+(Re_{gf}/1000)^2} + \frac{\left[\left(\sqrt{(1+(\rho_g/\rho_f)^2\cos\theta)/(1+\cos\theta)}\right)^{(1-\alpha)}\right]^{2/5}+C_{0,1}}{1+(1000/Re_{gf})^2}$ $C_{0,1}=\left(C_1-C_1\sqrt{\rho_g/\rho_f}\right)\left[(2.6-\beta)^{0.15}-\sqrt{f_{gf}}\right](1-x)^{1.5}$	$(0.35\sin\theta+0.45\cos\theta)\sqrt{\frac{gD\Delta\rho}{\rho_f}}(1-\alpha)^{0.5}C_2C_3C_4$ $C_2=\begin{cases}\left(\frac{0.434}{\log_{10}(\mu_f)0.001)}\right)^{0.15}, & \text{if } (\mu_f/0.001)>10\\ 1, & \text{if } (\mu_f/0.001)\le 10\end{cases}$ $C_3=\begin{cases}(La/0.025)^{0.9}, & \text{if } La<0.025\\ 1, & \text{if } La\ge 0.025\end{cases}$ $C_4=1$ or $C_4=-1$, if $(0^\circ>\theta\ge -50^\circ$ and $Fr_{sg}\le 0.1)$
Choi et al. [2012]	$\frac{2}{1+(Re_{gf}/1000)^2}+\frac{1.2-0.2\sqrt{\frac{\rho_g}{\rho_f}}\left(1-e^{(-18\alpha)}\right)}{1+(1000/Re_{gf})^2}$	$0.0246\cos\theta+1.606\left(g\sigma\Delta\rho/\rho_f^2\right)^{0.25}\sin\theta$
Hibiki and Ishii [2003] [b]	$(B)\quad 1.2-0.2\sqrt{\rho_g/\rho_f}(1-\exp(-18\alpha))$ $(S)\quad 1.2-0.2\sqrt{\rho_g/\rho_f}$ $(A)\quad 1+(1-\alpha)/\left(\alpha+4\sqrt{\rho_g/\rho_f}\right)$	$(B)\quad 1.41\left(g\sigma\Delta\rho/\rho_f^2\right)^{0.25}(1-\alpha)^{1.75}$ $(S)\quad 0.35\sqrt{gD\Delta\rho/\rho_f}$ $(A)\quad (1-\alpha)/\left(\alpha+4\frac{\sqrt{\rho_g/\rho_f}(\sqrt{gD\Delta\rho(1-\alpha)})}{0.015\rho_g}\right)$
Gomez L.E. and Chokshi [2000]	1.15	$1.53\left(g\sigma\Delta\rho/\rho_f^2\right)^{0.25}\sqrt{1-\alpha}\sin\theta$

[a] $C_1=0.2$ for circular and annular pipes, $C_1=0.4$ for rectangular pipes; $\beta=j_g/(j_g+j_f)$; $La=\sqrt{\sigma/(g\Delta\rho)}/D$.
[b] The letters $(S,B$ and $C)$ stands for Slug flow, Bubbly flow and Annular mist respectively.
$\Delta\rho=(\rho_f-\rho_g)$.

correlation. It can also be seen that the void fraction prediction methods of the drift flux analysis they all perform similarly, with slight differences between them.

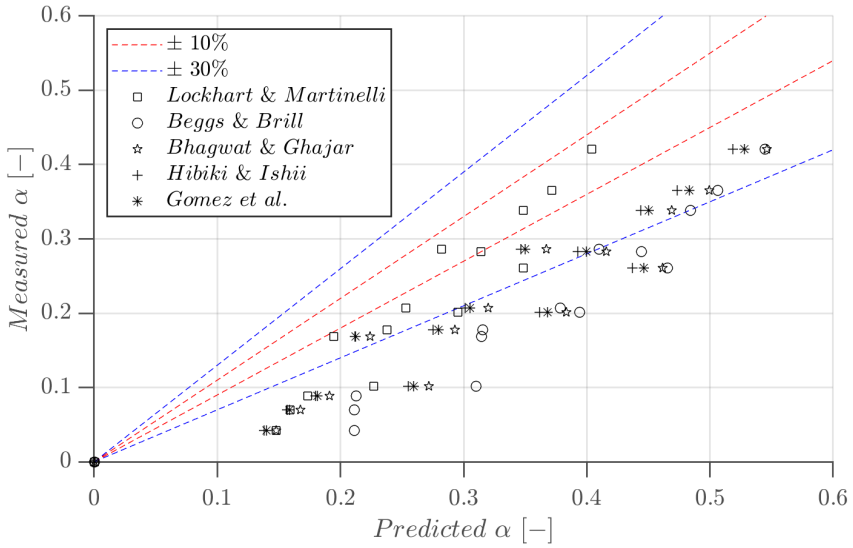

Figure 5.1: Performance of several void fraction correlations against experimental data.

5.3. Bibliography

P. K. Vijayan, A. P. Patil, D. S. Pilkhwal, D. Saha, and V. Venkat Raj. Assessment of pressure drop and void fraction correlations with data from two-phase natural circulation loops. *Heat and Mass Transfer/Waerme- und Stoffuebertragung*, 36(6):541–548, 2000. ISSN 09477411. doi: 10.1007/s002310000108.

H. Dale Beggs and James P. Brill. A study of two-phase flow in inclined pipes. *Journal of Petroleum Technology*, 25(5):607–617, 1973.

N. Zuber and J. Findlay. Average volumetric concentration in two phase systems. *Journal of Heat Transfer*, 87(4):453–468, 1965.

Swanand M. Bhagwat and Afshin J. Ghajar. A flow pattern independent drift flux model based void fraction correlation for a wide range of gas-liquid two phase flow. *International Journal of Multiphase Flow*, 59:186–205, 2014. ISSN 03019322. doi: 10.1016/j.ijmultiphaseflow.2013.11.001. URL http://dx.doi.org/10.1016/j.ijmultiphaseflow.2013.11.001.

Jinho Choi, Eduardo Pereyra, Cem Sarica, Changhyup Park, and Joe M. Kang. An efficient drift-flux closure relationship to estimate liquid holdups of gas-liquid two-phase flow in pipes. *Energies*, 5(12):5284–5306, 2012. ISSN 19961073. doi: 10.3390/en5125294.

Takashi Hibiki and Mamoru Ishii. One-dimensional drift-flux model and constitutive equations for relative motion between phases in various two-phase flow regimes. *International Journal of Heat and Mass Transfer*, 46 (25):4935–4948, 2003. ISSN 00179310. doi: 10.1016/S0017-9310(03)00322-3.

Schmidt Zelimir Gomez L.E., Shoham Ovadia and Tor Chokshi, R.N.; Northug. Unified mechanistic model for steady-state two-phase flow: Horizontal to vertical upward flow. *Society of Petroleum Engineers*, 5:339–350, 2000. doi: 10.2118/65705-PA.

Chapter 6

Slug frequency

The constant presence of intermittent flows can be destructive in the long term, due to the impact that it entails on the momentum and frictional pressure gradient, especially for long piping systems, where flow rates can fluctuate significantly. Moreover, the slug frequency (the number of unit slug cells that pass through a specific cross section in the pipe per unit time) could lead to resonance problems Thaker and Banerjee [2016a]. The study of intermittent flows entails great complexities, due to the inherent random nature of slug frequency Al-Safran [2016]. Several phenomena contribute to that randomness, such as slug initiation, break-up and coalescence of elongated bubbles, which are also random processes themselves. Further details on slug initiation and development can be found in Al-Safran [2009].

6.1. Previous studies

The prediction of slug frequency has been already addressed by several authors, and different measurement techniques have been developed for it. Counting slug units from video recordings is a widely used method, especially as a comparison tool due to its high fidelity. Also, the inference of the slug frequency from time signals has been the focus of several studies. Void fraction signals obtained from capacitance or impedance sensors, interface density functions obtained with probes (capacitance or optical) and differential pressure signals are some examples of the signals used in the literature. Furthermore, the approaches that are mostly used to obtain the frequency from the signals are (i) counting peaks above certain threshold and (ii) calculating

the power spectral density of the signal to obtain the dominant frequency. table 6.1 summarizes some relevant studies on slug frequency in horizontal pipelines, their corresponding experimental techniques and conditions during the measurements, as well as their main findings or proposed correlations.

Both counting and spectral methods provide precise results for relatively low velocities. However, when flow velocities increase, the slug frequency is no longer dominated by a single frequency, as several frequencies with similar power can be observed Bertola and Cafaro [2002], Al-Safran [2016]. Most of the correlations used for predicting the slug frequency are deterministic, as they provide one single value of frequency. Al-Safran [2016] has proposed a probabilistic model, using Poisson probability theory to take into account the random behaviour of the slug frequency and also the systematic errors derived from the use of experimental instruments.

Table 6.1: Previous studies on slug frequency in horizontal pipelines

Author	D[mm]	L/D	Superficial velocities [m/s]	Measurement technique	Correlation / findings
Gregory and Scott [1969]	19.1	-	$j_f = 0.6 - 2$ $j_g = 0.3 - 8$		$f_S = 0.0226 \left[\frac{j_f}{gD}\left(\frac{19.75}{U_M} + U_M\right)\right]^{1.2}$
Fetter [1988]	70 82	-	$j_f = 0.1 - 4$ $j_g = 0.5 - 20$	Signal processing from clamp-on acoustic two-phase flow-meter. Developed with two accelerometers clamped to the pipe wall (2 meters apart).	$f_S = 0.0175 \left[\frac{j_f}{gD}\left(\frac{21.3 + U_M^2}{U_M}\right)\right]^{1.37}$
Manolis et al. [1995]	78	363	$j_f = 0.5 - 1.25$ $j_g = 1 - 7$	Water hold-up from gamma densitometer at sampling frequency of 25 Hz, two conductivity probes (60 cm. separation) and high spreed video camera (50 FPS).	$f_S = 0.037 Fr_{mod}^{1.8}$, $Fr_{mod} = \frac{j_f}{gD}\left(\frac{U_{M,min}^2 + U_M^2}{U_M}\right)$
Bertola and Cafaro [2002]	80	96, 101, 104	$j_f = 0.6 - 2$ $j_g = 0.3 - 8$	Counting peaks above threshold and PSD of phase density function from optical probe at 2 kHz.	-
Fossa et al. [2003]	40 60	95, 148, 151, 255 33, 100, 160	$j_f = 0.6 - 3.0$ $j_g = 0.3 - 4.0$	Void probability density function from impedance meter (20 kHz) and comparison with slug residence time from fast camera.	$St_g = \frac{f_S D}{j_g} = \frac{0.044\lambda_f}{1 - 1.71\lambda_f + 0.7\lambda_f^2}$
Wang et al. [2007]	50	1157, 2609	$j_f = 0.16 - 1.5$ $j_g = 1 - 20$	Reciprocal of slug unit period, calculated with gas-liquid interface density function, from pairs of conductivity probes.	$St_g = \frac{0.05\lambda_f}{1 - 1.675\lambda_f + 0.768\lambda_f^2}$
Wilkens and Thomas [2008]	52	145 - 280	$j_f = 0.36 - 0.59$ $j_g = 1.5 - 10$	Counting peaks above threshold from differential pressure transducers signal.	Wilkens and Thomas method
Al-Safran [2009][a]	50.8 [b]	3898, 6920	$j_f = 0.06 - 1.2$ $j_g = 0.64 - 4.27$	Liquid hold-up from capacitance sensors.	$\ln(f_S) = 0.8 + 1.53\ln(U_f) + 0.27\left(\frac{U_{slip}}{U_M}\right) - 34.1D$ $U_L = \frac{j_f}{H_f}, \quad U_{slip} = \frac{j_g}{(1 - H_f)} - \frac{j_f}{H_f}$
Thaker and Banerjee [2015]	25	30, 60, 120, 190, 260	$j_f = 0.11 - 0.74$ $G_g = 0.13 - 2.6 g/s$	Time interval between slugs calculated from images taken at 1200 FPS.	$f_S' = 1.52 \times 10^{-8} \left(\frac{L}{D}\right)^{-0.14} (Re_f)^{1.45} (Re_g)^{0.28}$
Thaker and Banerjee [2016b]	25	-	$j_f = 0.02 - 1.14$ $j_g = 0.484–4.312$	Time interval between slugs calculated from fast camera images.	Erosion-corrosion map
Thaker and Banerjee [2016a]	-	-	$j_f = 0.194–0.971$ $j_g = 0.484–3.388$	Time interval between slugs calculated from images taken at 1600 FPS.	$St_M = \frac{0.036\lambda_f}{1 - 1.432\lambda_f + 0.739\lambda_f^2}$
Al-Safran [2016]	25 - 203	-	$j_f = 0.03 - 2.89$ $j_g = 0.06 - 16.5$	Data taken from experimental data bank.	$\ln(f_S) = 1.51 - 17.04D + 0.77\ln(j_f) - 0.181\ln(S)$ $S = \frac{U_g}{U_f} = 1 + 1.95\left(\frac{\mu_f}{\mu_0}\right)^{0.01}\left(\frac{j_g}{j_f}\right)^{1.5}$
Archibong-Eso et al. [2018][c]	25.4 76.4	190 220	$j_f = 0.03 - 0.31$ $j_g = 0.1 - 7.0$	Counting peaks above threshold of void fraction signals from electrical capacitance. Comparison with counts from visual observation with fast-camera and two gamma densitometers.	$\ln(f_S) = \beta \ln\left[\frac{\lambda}{\varphi^n}\right]$ $\varphi = \left[\frac{D^{3/2}\sqrt{\rho_f(\rho_f - \rho_g)\, g}}{\mu_f}\right]$ $(\beta, n) = \begin{cases} (0.75, 0.55) & \mathrm{Re}_{SG} \leq 2500 \\ (0.35, 1.02) & \mathrm{Re}_{SG} > 2500 \end{cases}$
Al-Alweet et al. [2020]	20 [b]	170	$j_f = 0–1.06$ $j_g = 0–5$	Frequency and statistical analysis of liquid hold-up signals from two-electrodes capacitance sensor.	Identification of flow patterns
Arabi et al. [2020a]	30	173.3 – 193.3	$j_f = 0.15–0.8$ $j_g = 0.4–3.6$	Comparison of counting slugs, Wilkens & Thomas and PSD methods using fast-camera images and differential pressure transducers signals.	$St_g = \frac{A\lambda_f}{1 + B\lambda_f + C\lambda_f^2}$ $A = 0.06327; 0.04071; 0.04234$ $B = -1.855; -3.105; -4.271$ $C = 1.163; 4.188; 13.860$
Arabi et al. [2020b]	25 - 76.3	-	$j_f = 0.03–2$ $j_g = 0.046–0.786$	Data taken from experimental data bank.	$St_g = \frac{0.03693\lambda_f}{1 - 1.865\lambda_f + 0.9118\lambda_f^2}$

[a] air/oil as working fluids. [b] Inclined orientations measurements are also reported. [c] air/water and air/oil as working fluids.

6.2. Methodology

6.2.1. Frequency measurement

The frequency of the slug units is measured by processing images from the fast camera. For this, the images obtained in the experimental campaign number 3 are used. The details on the measurements are presented in appendix A.3

In the time series image (TSI), whose construction method is detailed in appendix A.3.1, the elongated bubbles can be easily identified (noses and tails). The upper panel of fig. 6.1 shows an example of slug units location during the first second of the TSI of a two-phase flow run. The blue and red vertical lines correspond to the location of the noses and tails of the elongated bubbles respectively. In order to identify the noses and tails, the mean intensity of the image is calculated in the vertical axis, zero-meaned and filtered with a low pass filter (moving mean of the signal with a width of 20 samples). The filtered signal corresponding to the TSI is plotted in the bottom panel of fig. 6.1 for the same time interval. It can be seen that for this particular regime, the filtered signal in the presence of a bubble is less than zero and greater in the presence of a liquid slug. Thus, noses can be identified when the filtered signal cuts the zero downwards and tails when it cuts it upwards.

Since the horizontal axis of the TSI is a measure of time, the distance between two consecutive noses (two blue lines in fig. 6.1) is a measure of the residence time of a slug unit. This is nothing more than the period of an individual slug unit, and therefore its inverse is the frequency. It is then possible to calculate a frequency for each individual slug unit and plot a frequency histogram for each run. fig. 6.2 shows the histogram of slug unit frequencies for a two-phase flow with $j_f = 1.5\ m/s$ and $j_g = 0.58\ m/s$. In total, 555 slug units were identified in 75 seconds, representing an average frequency of 7.4 Hz (red line in fig. 6.2).

It can be seen that the histogram from fig. 6.2 is right skewed, and the blue dots correspond to the Poisson probability distribution. The distribution fits precisely the experimental data in the histogram. More details on the suitability of the distribution can be found in Al-Safran [2016], whose author proposed the distribution to characterize slug frequency.

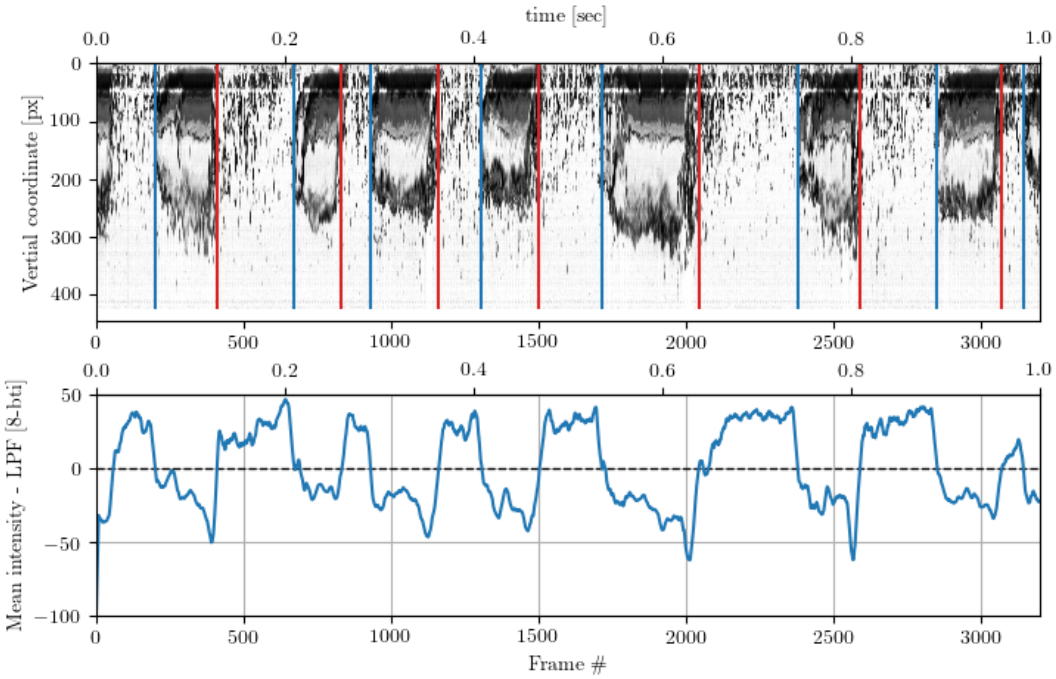

Figure 6.1: Elongated bubbles location for a two-phase flow run, $j_f = 1.5$ m/s and $j_g = 0.58$ m/s. a) Time series image (TSI) with noses and tails of bubbles located with blue and red lines respectively. Flow from right to left. b) Cero-mean intensity in vertical coordinate with low pass filter.

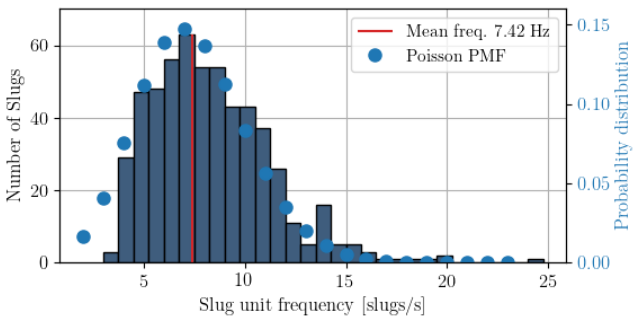

Figure 6.2: Slug unit frequency histogram and probability distribution, two-phase flow $j_f = 1.5\ m/s$ and $j_g = 0.58\ m/s$

6.2.2. Velocity and size measurement

Using the TSI described in appendix A.3.2, with full size frames, the nose and tails of the bubbles can be located as described above. Since full resolution images (640×320) were acquired for this analysis, it is possible to open the frames that contains the noses and tails of every bubble. Then, for each bubble an interrogation window including the nose or tail of the bubble is extracted and cross-correlated with an image taken a few milliseconds later. In this way a displacement can be calculated between the original position of the interrogation window and the new location, where the maximum correlation coefficient is obtained. fig. 6.3 shows the process for an example bubble of the $Ug = 1.02$ and $Uf = 1\ m/s$ run. In figs. 6.3a and 6.3b the interrogation windows enclosing the nose and tail are indicated with dashed lines respectively. figs. 6.3c and 6.3d correspond to tenth subsequent frames of figs. 6.3a and 6.3d respectively, and the red rectangles indicate where the maximum correlation coefficient is found between the interrogation window and the current frame. A sensitivity analysis of the velocity calculations is presented in appendix A.3.3.

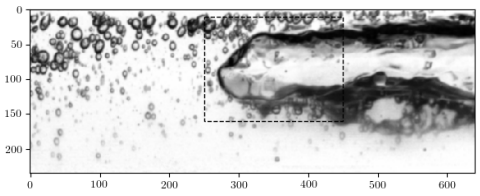

(a) Nose interrogation window.

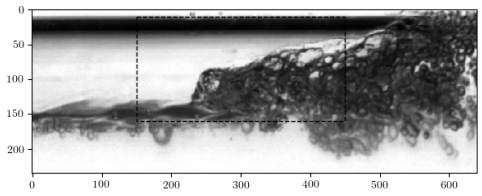

(b) Tail interrogation window.

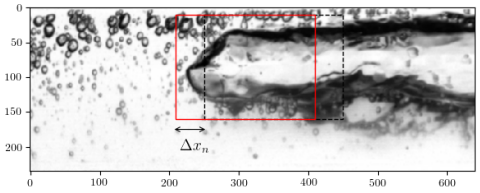

(c) Maximum correlation coefficient location at tenth following frame.

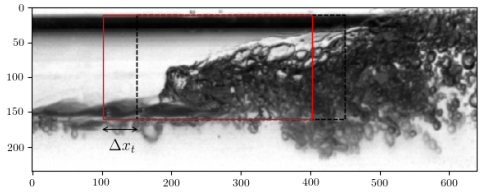

(d) Maximum correlation coefficient location at tenth following frame.

Figure 6.3: Example of cross-correlation applied to nose and tail of an elongated bubble to calculate velocity and size of bubble. Two-phase run with $j_f = 1.0\ m/s$ and $j_g = 1.02\ m/s$, flowing from right to left.

Finally, the length of the bubbles is determined in eq. (6.1), using the mean velocity of each bubble ($\bar{U_b}$) and the residence time of the corresponding bubble in the cross section ($t_1 - t_0$) of the TSI. Where t_0 is the instant of time in which the nose intersects the cross section, and t_1 when the tail intersects it. ($t_1 - t_0$)

corresponds to the distance in pixels between a blue line and the consecutive red line in the TSI (fig. 6.1) divided by the frame rate.

$$L_b = \bar{U}_b \cdot (t_1 - t_0) \tag{6.1}$$

6.3. Experimental results

Results are presented for two and three-phase flows, including volume concentrations of 10 and 20 % of solid. The summary of the experimental data used in this section is summarized in fig. A.4 (appendix A.3). First, the results regarding slug frequency are presented for all runs including mean frequency and frequency distributions. Then, the incidence of several parameters over the bubbles velocity are reported. Finally, the bubble length measurements are listed.

6.3.1. Slug frequency

The measured slug frequency for all the runs are presented in fig. 6.4, the slug frequency is plotted against the liquid superficial velocity. figs. 6.4a to 6.4c correspond to the measurements for two-phase flow and three-phase flow with 10% and 20% of solid loading respectively. The filling of the markers indicate the gas mass flow (note that as the liquid velocity increases so does the pressure of the system, and thus the gas velocity decreases for identical mass flow rate). The white, green, yellow and grey markers indicate a gas mass flow of 0.75, 1.25, 2.00 and 4.00 g/s respectively. The dashed lines connect the circles with the same gas mass flow.

In fig. 6.4 it can be noted the strong influence of the liquid superficial velocity on the slug frequency, which has been already identified and addressed by several authors. It can also be noted, that the influence of the gas superficial velocity becomes stronger at higher liquid superficial velocities. This is evidenced in the divergence of the dashed lines. At low liquid velocities the circles are close to each other and spread farther apart as the velocity increases. Finally, there is a modest influence of the solid phase on the slug frequency. When comparing figs. 6.4a and 6.4b, a slight decrease in the mean frequency is observed in the runs with solid particles, and when comparing the corresponding runs in figs. 6.4b and 6.4c, another small decrease

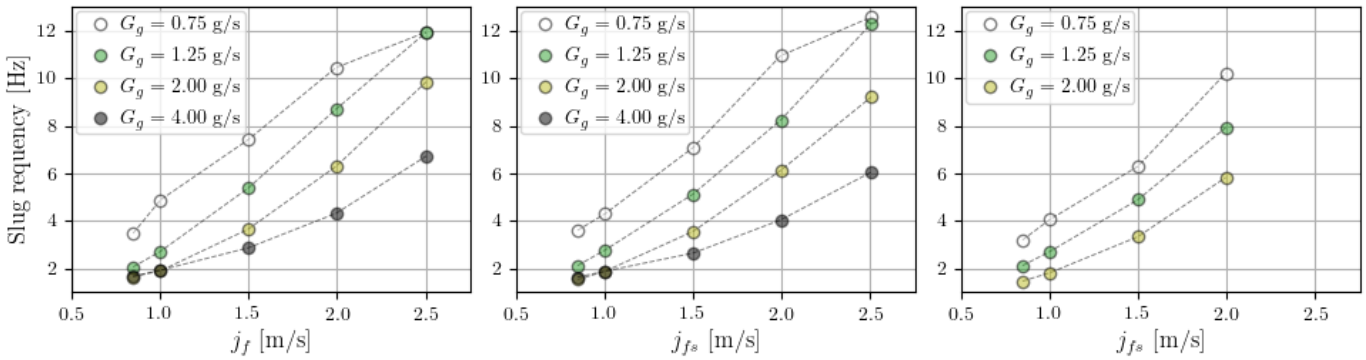

(a) Two-phase flow. **(b)** Three-phase flow 10% loading **(c)** Three-phase flow 20% loading

Figure 6.4: Slug frequency against liquid superficial velocity, parametric in gas mass flow.

is noted. These results suggest that, for increasing solid concentrations, there is a decrease on the slug frequency. This could be explained for the accumulation of solid particles in the tail of the elongated bubbles, which make it difficult to detach the bubbles from the tail, as reported in section 3.1. If the detachment of bubbles is reduced, the elongated bubbles will contain more air and therefore will be longer. Longer bubbles for the same setting of superficial velocities results in a lower frequency, as fewer slug units will be counted in the same time interval.

Note that the plotted frequencies in fig. 6.4 represent the mean frequencies. But the slugs are different in size and travel in a certain speed range. So, the slug frequency is not constant but follows a probabilistic distribution, which is well represented by a Poisson distribution (fig. 6.2). In figs. 6.5 to 6.7 the histograms of the inverse of the permanence time (frequency) of the slug units are illustrated for all the two and three-phase runs with 10% and 20% of solid loading respectively.

The vertical axes in the histograms of figs. 6.5 to 6.7 are not normalized, and so they indicate the number of slug units in the corresponding bin. The red vertical lines indicate the mean frequency, whose values are plotted on fig. 6.4. It can be seen that the regimes with lower mean frequencies have a very narrow frequency distribution, whereas the distributions with high mean frequencies are extended over a wide range of frequencies.

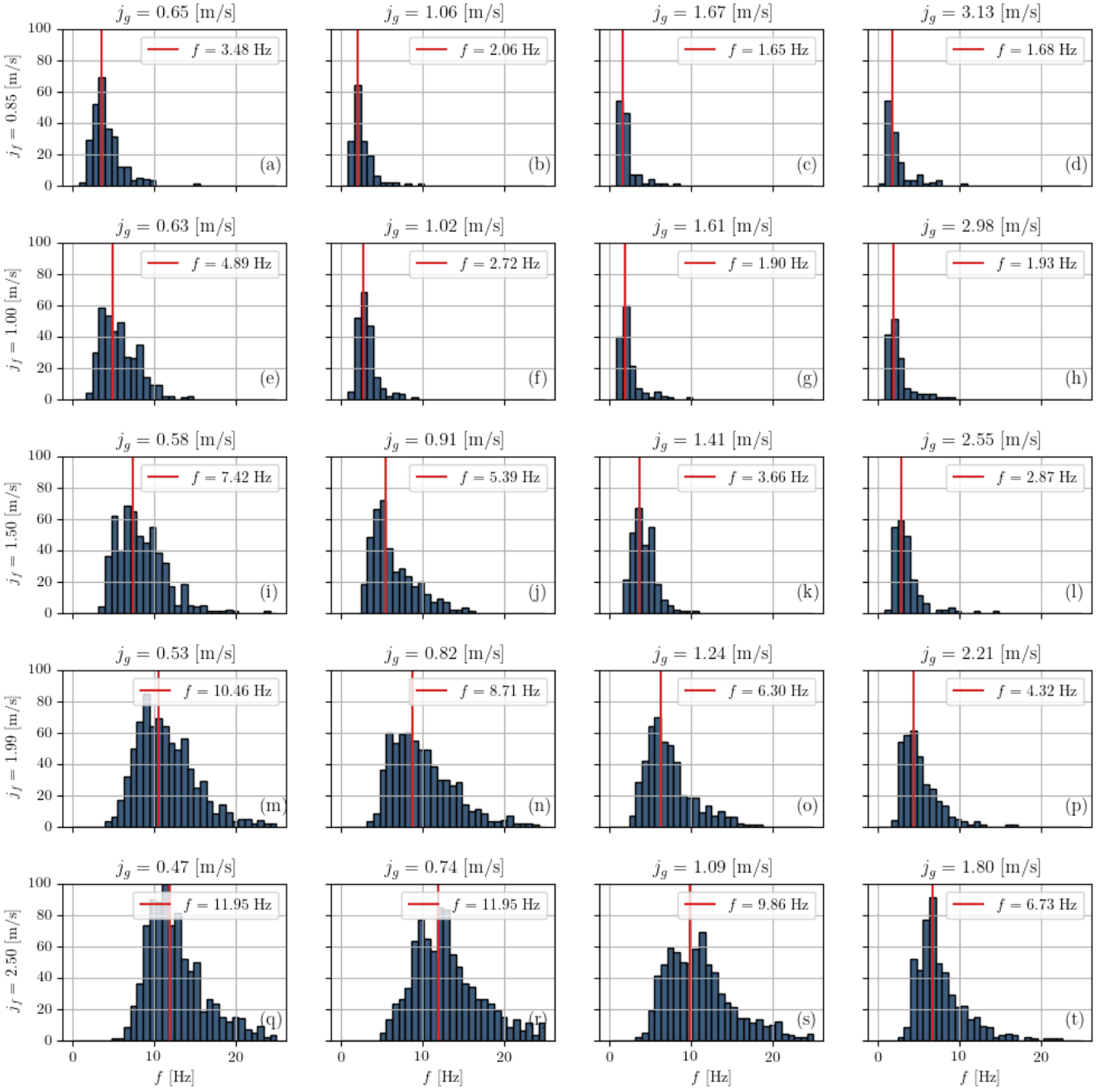

Figure 6.5: Histograms of measured slug frequencies for two-phase flow.

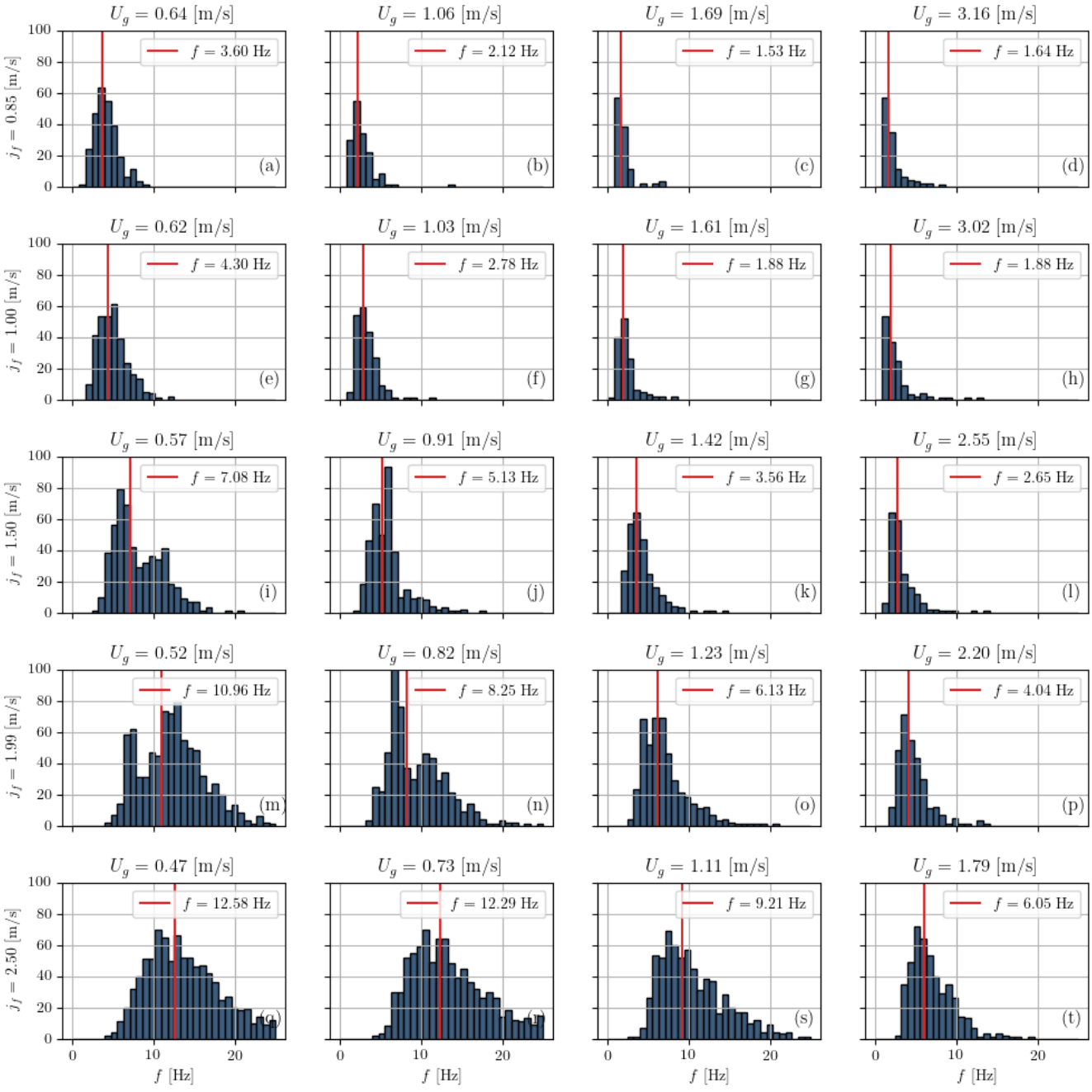

Figure 6.6: Histograms of measured slug frequencies for three-phase flows with 10% of solid concentration.

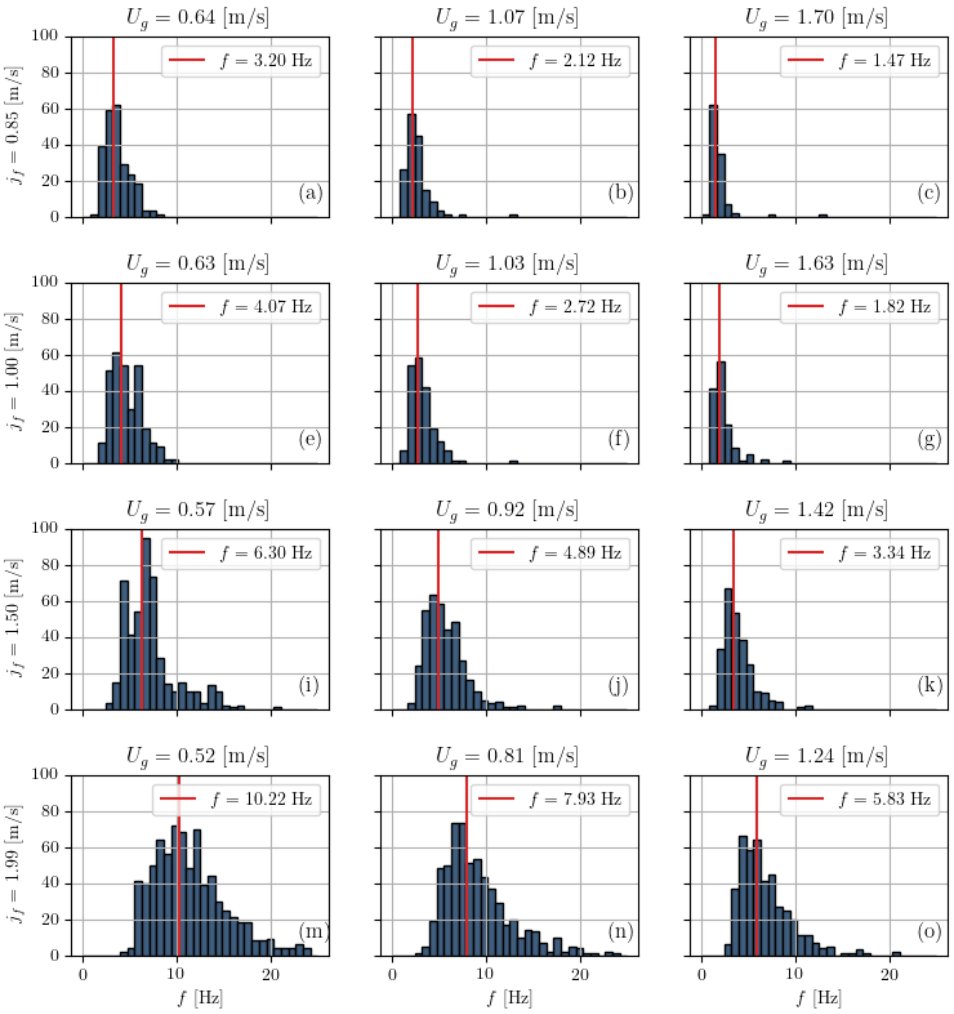

Figure 6.7: Histograms of measured slug frequencies for three-phase flows with 20% of solid concentration.

6.3.1.1. Correlations

The experimental data is compared with some of the correlations listed in table 6.1. It can be noted that different correlations provide very different results. Some correlations underestimate the slug frequency, while other overestimate it.

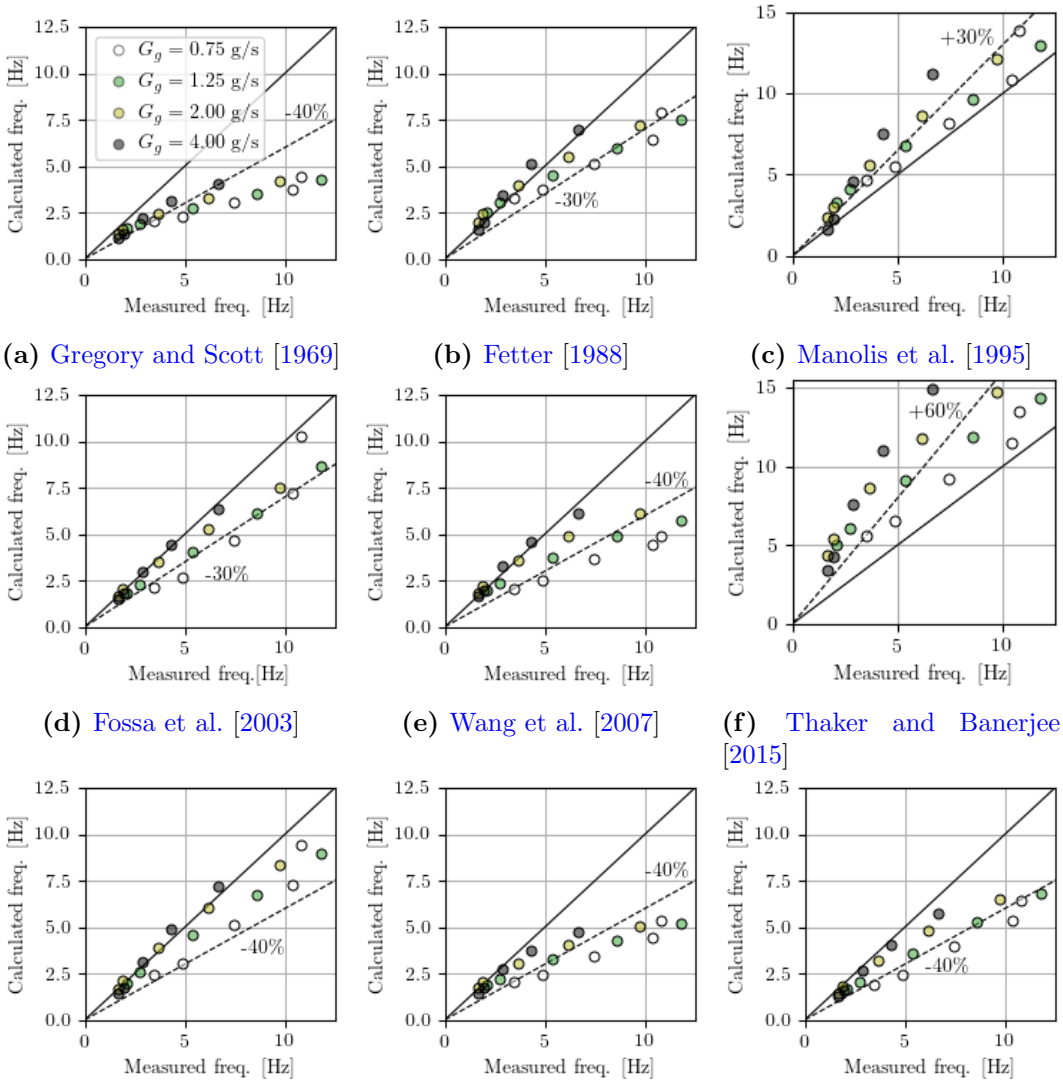

(a) Gregory and Scott [1969] **(b)** Fetter [1988] **(c)** Manolis et al. [1995]

(d) Fossa et al. [2003] **(e)** Wang et al. [2007] **(f)** Thaker and Banerjee [2015]

(g) Thaker and Banerjee [2016a] **(h)** Al-Safran [2016] **(i)** Arabi et al. [2020b]

Figure 6.8: Comparison of previous correlations

The mean squared error (MSE) between the measured frequency and the predicted values of frequency from the different correlation are presented in table 6.2. The best prediction is obtained with the correlation proposed by

Thaker and Banerjee [2016a], who relates the mixture Strouhal number (St_M) with the input liquid fraction λ_f.

Table 6.2: Performance of previous correlations with the experimental data.

Correlation	MSE
Gregory and Scott [1969]	13.8
Fetter [1988]	3.88
Manolis et al. [1995]	3.15
Fossa et al. [2003]	2.73
Wang et al. [2007]	8.99
Thaker and Banerjee [2015]	15.19
Thaker and Banerjee [2016a]	2.17
Al-Safran [2016]	10.3
Arabi et al. [2020b]	6.72

Finally, the experimental data is fitted to some of the proposed correlations in fig. 6.9. The experimental data collapse quite good in the proposed curves, only a pair of data points seem to be slightly displaced from the collapsing curves, corresponding to low rates of air and water. The performance of the fitted correlations is evaluated with the mean squared error for each of the three fitted curves in table 6.3. All the three correlations performed very well, with low values of the mean squared error. Yet, a slight improvement is achieved when calculating the gas Strouhal number (St_g) as a function of the liquid input fraction (λ_f).

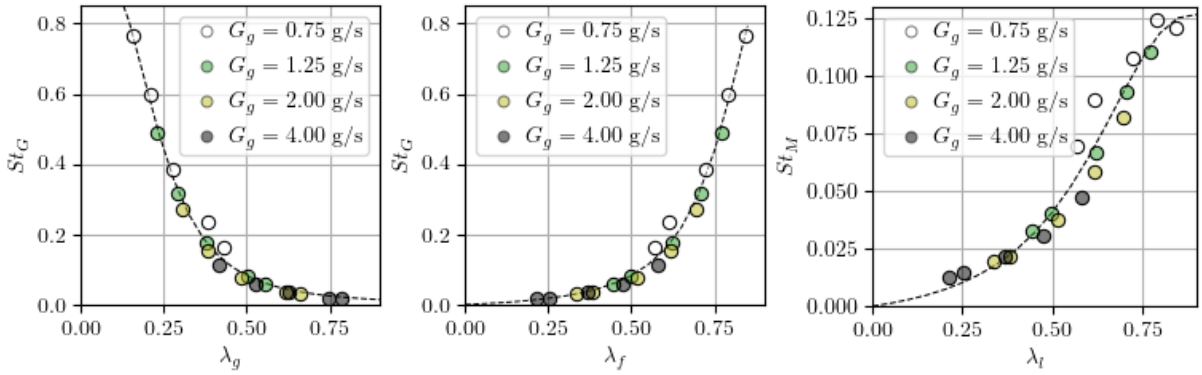

(a) St_g vs λ_g **(b)** St_g vs λ_f **(c)** St_M vs λ_f

Figure 6.9: Two-phase data collapsed in curves of non-dimensional parameters.

Table 6.3: Fitted parameters and performance of the correlations from fig. 6.9

Correlation	$St_g(\lambda_g)$	$St_g(\lambda_f)$	$St_M(\lambda_f)$
Equation	$St_g = \frac{A}{1+B\lambda_g^C}$	$St_g = \frac{A\lambda_f}{1+B\lambda_f+C\lambda_f^2}$	$St_M = \frac{A\lambda_f}{1+B\lambda_f+C\lambda_f^2}$
Fitted parameters	A = 0.99 B = 96.93 C = 3.14	A = 0.038 B = -2.130 C = 1.178	A = 0.023 B = -2.070 C = 1.267
MSE	0.47	0.45	0.52

6.3.2. Bubble velocity

Mean bubble velocity is calculated by averaging the nose and tail velocities of all bubbles captured by the camera during the 17 seconds of recording, which are calculated through the algorithm described in section 6.2.2. In fig. 6.10 the mean velocities of the bubbles are presented for the different runs versus the superficial mixture velocity (j_M). The colors of the markers indicate the gas mass flow, and the error bars represent the standard deviation of the samples. Moreover, depending on the size and speed of the bubbles, the number of bubbles visible in the time window varies in different runs. The size of the markers in Fig. 6.10 indicate the amount of bubbles used for averaging in the corresponding run, which in two-phase runs ranges from 25 to 189 bubbles.

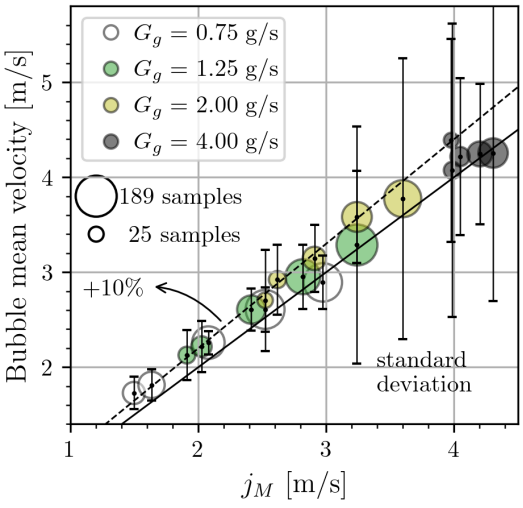

Figure 6.10: Bubbles mean velocity per run vs. mixture velocity, two-phase flow Color indicate gas mass flow, size indicate number of bubbles in run, and error bars indicate standard deviation of the bubbles velocity.

As j_M increases, the average velocity of the bubbles increases linearly by a

ratio in the order of 1.1 with the superficial mixture velocity, as indicated by the dashed line in fig. 6.10. Also, the variability of bubble velocity increases, which is evidenced by higher standard deviations (larger error bars) at higher j_M Thaker and Banerjee [2016a]. Equivalent plots are presented for three-phase flows in figs. 6.11a and 6.11b for 10 and 20% of solid loading respectively.

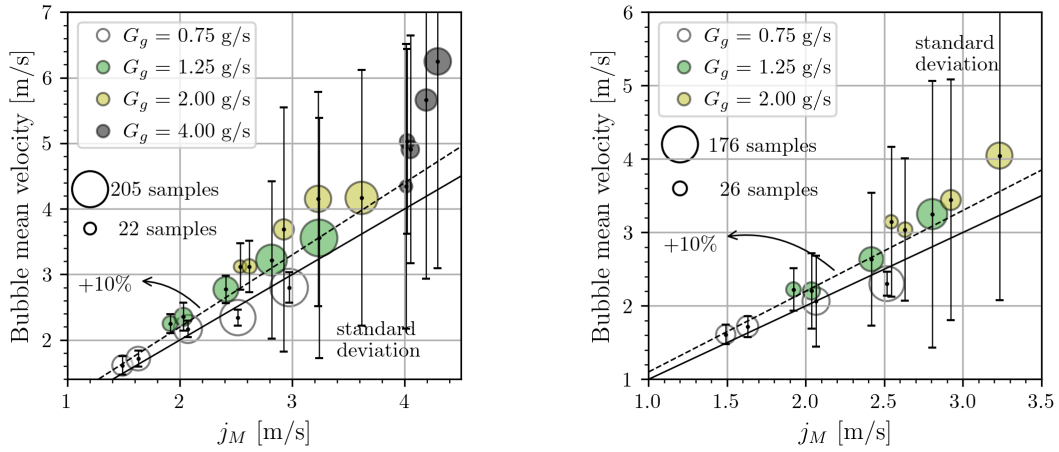

(a) 10% loading. **(b)** 20% loading.

Figure 6.11: Bubbles mean velocity per run vs. mixture velocity, three-phase flow Color indicate gas mass flow, size indicate number of bubbles in run, and error bars indicate standard deviation of the bubbles velocity.

From figs. 6.10 and 6.11 it can be seen that three-phase flows present more dispersion on the bubble velocity. In two-phase flows (fig. 6.10), the bubble velocity is mainly between 1 and 1.1 times the mixture velocity. For three-phase flows (fig. 6.11), the bubble velocity ranges from 1 up to 1.5 times the mixture velocity.

A more detailed analysis of the bubble velocities is given in fig. 6.12 for two-phase flows. It shows the incidence of the liquid superficial velocity and the air mass flow over the bubbles mean velocity fig. 6.12a, the nose and tail of velocities figs. 6.12b and 6.12d and the standard deviation fig. 6.12c. Again, the colors of the markers indicate the mass flow rate of air. Note that the gas velocity differs along runs with the same mass flow, because of the increment of pressure related to an increasing liquid superficial velocity. The mean bubble velocity (fig. 6.12a) is the average of the nose 6.12b and tail 6.12d mean velocities. As expected, by increasing any of both, either liquid or gas flow rates, the velocity of the bubbles also increase. However, for high rates of air flow (black dots), the increment of the bubble velocity due to increasing j_f

is not as strong as in the other runs.

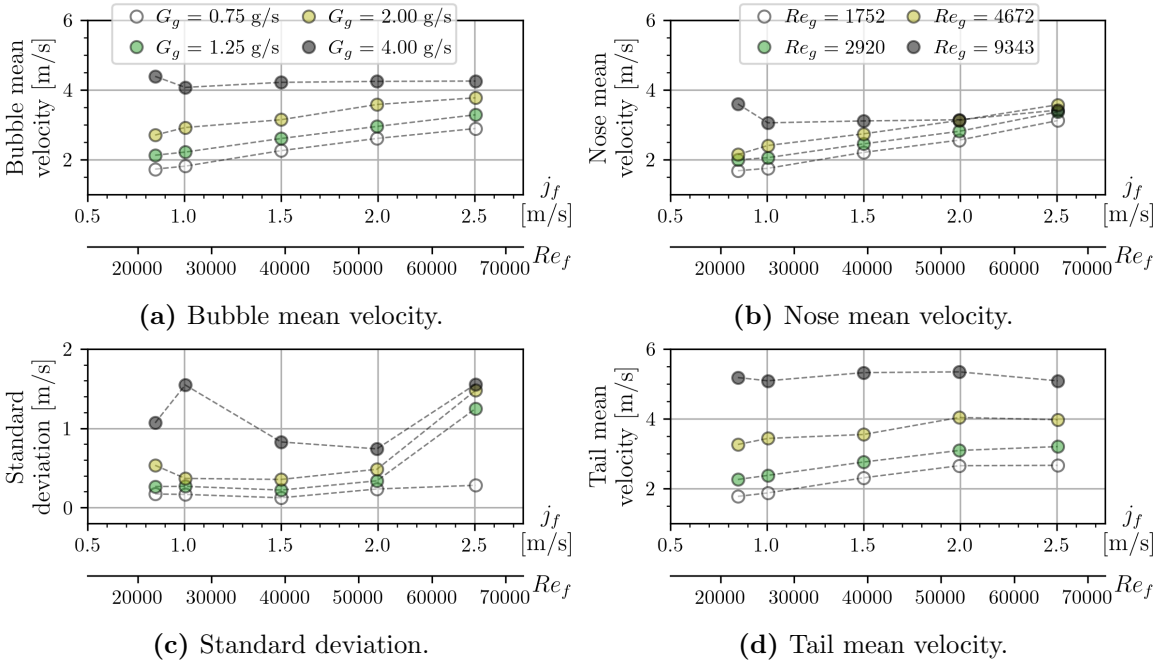

(a) Bubble mean velocity.

(b) Nose mean velocity.

(c) Standard deviation.

(d) Tail mean velocity.

Figure 6.12: Incidence of liquid superficial velocity and gas mass flow on bubbles velocity, two-phase flow.

Comparing the images in figs. 6.12b and 6.12d, who show the nose and tail mean velocities respectively, it can be noticed that the slope in the nose mean velocity is steeper than the slope of the tail velocity, and the markers corresponding to the different gas mass flow rates are closer in the nose velocity and further distant to each other on the tail graph. This means that the liquid superficial velocity has greater impact on the nose velocity than it has on the tail velocity, where the gas superficial velocity has a greater influence. Also, it can be noted that for higher rates of air, the upward trend in bubble velocity is inverted in the zone of low liquid superficial velocities. Similar conclusions were found in Thaker and Banerjee [2016b,a].

Moreover, it can be noted that tail velocity becomes more significant for higher rates of air. The white markers (low air rates) in figs. 6.12b and 6.12d are at comparable levels, but for higher air rates the tail velocity increases much higher than the nose velocity at fixed liquid superficial velocities. At high airflow regimes, aeration in front of liquid pockets increases along with turbulence. This high aeration near the tail of the bubble, together with the overcoming of the liquid film underneath the bubble (which moves much slower than the bubble and the liquid pocket), produce strong eddies in the tail of

the bubble which in turn generates the effect of a wave breaking at the tail of the bubble (see section 3.1), thus increasing the tail velocity.

In fig. 6.13 the same analysis is presented for three-phase flows with 10% of solid loading. In general, a similar behaviour is observed between 2P and 3P10 runs. In the mean velocity, very similar values and trends are obtained for the lower air flow rates. However for the grey dots (4.0 g/s of air) in 2P flow (fig. 6.12a) there seems to be low influence of the liquid superficial velocity, while in 3P flows a similar trend is observed for the four air rates (fig. 6.13a). For the nose velocity, similar slopes are identified, which indicate that the effect that induces the liquid superficial velocity is very similar in both cases. In the other hand, the effect of the air flow rate is more significant for 3P flows, as the markers are more spread apart in the vertical direction. Looking at the tail velocities in figs. 6.12d and 6.13d very similar values are seen for all the runs. Finally, when comparing the standard deviations of the mean velocity in figs. 6.12a and 6.13a, an increment on the variation is seen in 3P runs. At low values of superficial velocities the std value are similar, but a strong increment is noted for increasing superficial velocities.

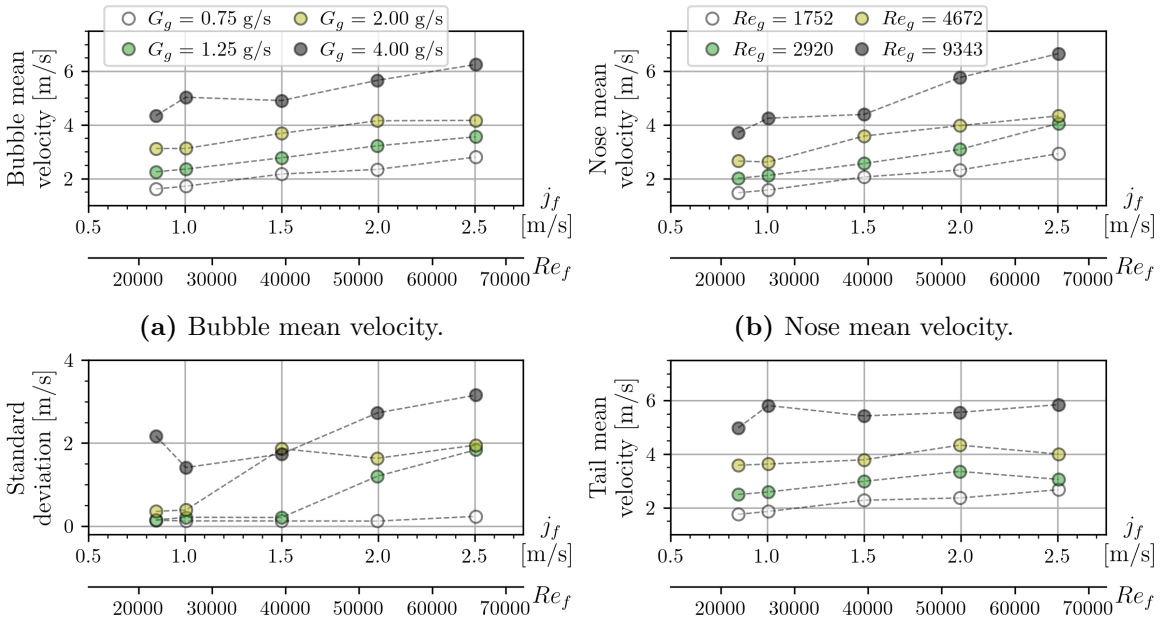

(a) Bubble mean velocity.

(b) Nose mean velocity.

(c) Standard deviation.

(d) Tail mean velocity.

Figure 6.13: Incidence of liquid superficial velocity and gas mass flow on bubbles velocity, three-phase flow 10% of solid loading.

To conclude with the bubble velocity analysis, results are presented for

the 12 runs of three-phase flows with 20% of solid concentration in fig. 6.14. The mean results are very similar to its corresponding ones with 10% of solid concentration from fig. 6.13. The main difference is seen in the standard deviations, which increase in value from even lower superficial velocities values bot of water and air.

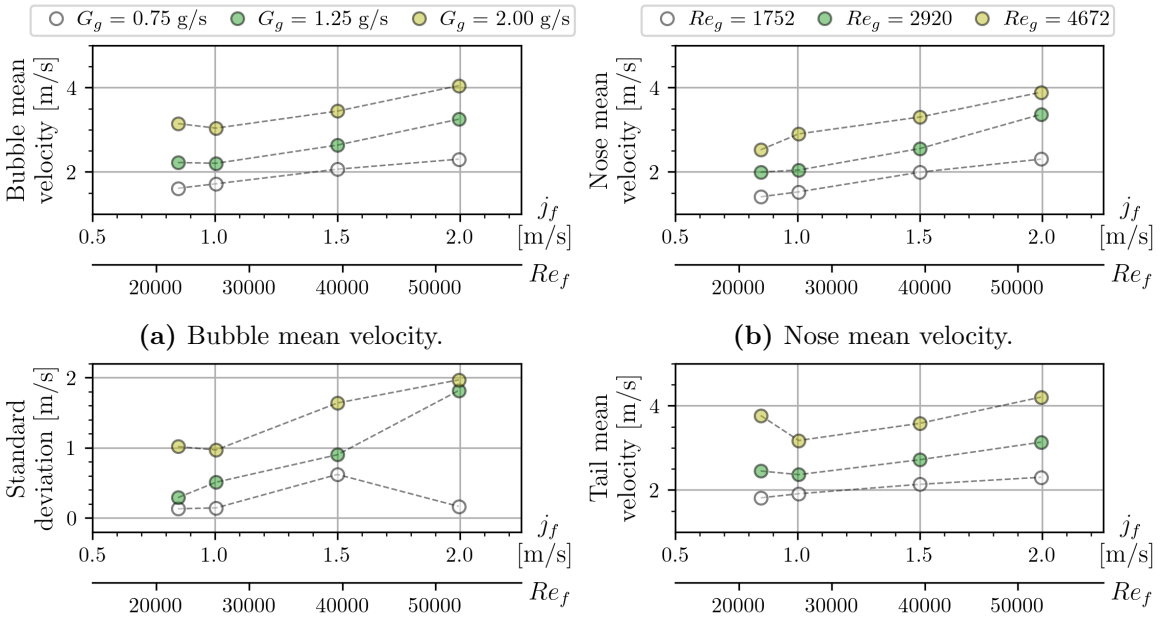

(a) Bubble mean velocity.

(b) Nose mean velocity.

(c) Standard deviation.

(d) Tail mean velocity.

Figure 6.14: Incidence of liquid superficial velocity and gas mass flow on bubbles velocity, three-phase flow 20% of solid loading.

6.3.3. Bubble length

Finally, the length of the bubbles is determined in eq. (6.2), using the mean velocity of each bubble ($\bar{U}_b$) and the residence time of the corresponding bubble in the cross section ($t_1 - t_0$) of the time series image. Where t_0 is the instant of time in which the nose intersects the cross section, and t_1 when the tail intersects it. ($t_1 - t_0$) corresponds to the distance in pixels between a blue line and the consecutive red line in the time series image (fig. 6.1) divided by the frame rate. The results are presented in fig. 6.15 for two and three phase flows.

$$L_b = \bar{U}_b \cdot (t_1 - t_0) \tag{6.2}$$

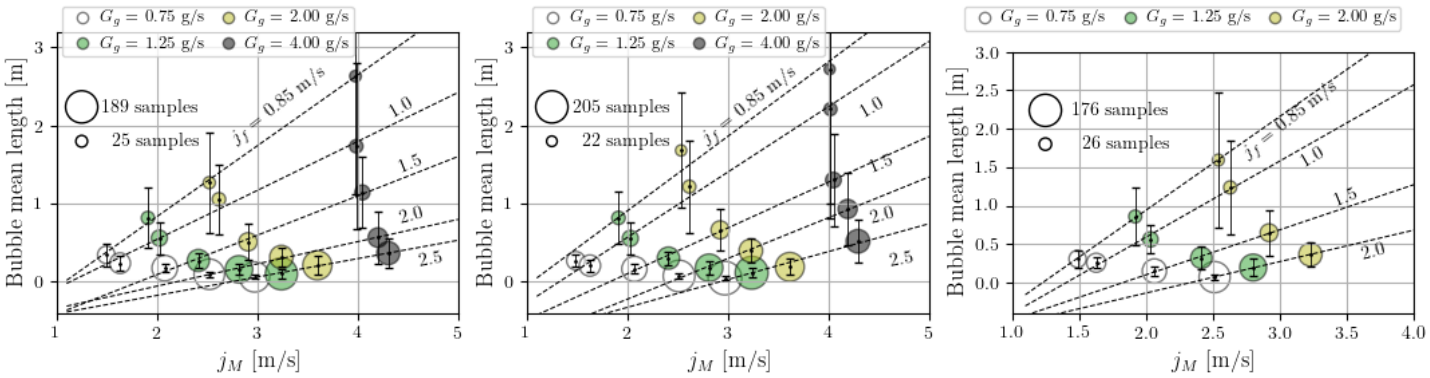

(a) St_g vs λ_g **(b)** St_g vs λ_f **(c)** St_M vs λ_f

Figure 6.15: Bubbles mean length per run vs. mixture velocity.

It can be seen that in general the length of the bubbles is increased due to the presence of the solid phase. Which is in concordance with the decrease on the slug frequency, since longer bubbles with the same mixture velocity will have longer residence times and therefore smaller frequencies.

6.4. Bibliography

Jignesh Thaker and Jyotirmay Banerjee. On intermittent flow characteristics of gas–liquid two-phase flow. *Nuclear Engineering and Design*, 310:363–377, 2016a. ISSN 00295493. doi: 10.1016/j.nucengdes.2016.10.020. URL http://dx.doi.org/10.1016/j.nucengdes.2016.10.020.

Eissa M. Al-Safran. Probabilistic modeling of slug frequency in gas/liquid pipe flow using the Poisson probability theory. *Journal of Petroleum Science and*

Engineering, 138:88–96, 2016. ISSN 09204105. doi: 10.1016/j.petrol.2015.12.008. URL http://dx.doi.org/10.1016/j.petrol.2015.12.008.

Eissa Al-Safran. Investigation and prediction of slug frequency in gas/liquid horizontal pipe flow. *Journal of Petroleum Science and Engineering*, 69(1-2):143–155, 2009. ISSN 09204105. doi: 10.1016/j.petrol.2009.08.009. URL http://dx.doi.org/10.1016/j.petrol.2009.08.009.

G A Gregory and D S Scott. Correlation of liquid slug velocity and frequency in horizontal cocurrent gas-liquid slug flow. *AIChE Journal*, 15(6):933–935, 1969. doi: https://doi.org/10.1002/aic.690150623. URL https://aiche.onlinelibrary.wiley.com/doi/abs/10.1002/aic.690150623.

C.P. Fetter. *Development of a clamp-on acoustic two-phase flowmeter*. Master thesis, Technical University Delft, 1988. URL http://resolver.tudelft.nl/uuid:a3e8c0c1-4f45-4399-b327-f11fb18db149.

I.G. Manolis, M.A. Mendes-Tatsis, and G.F. Hewitt. *The Effect of Pressure on Slug Frequency in Two-Phase Horizontal Flow*. Elsevier Science B.V., 1995. doi: 10.1016/b978-0-444-81811-9.50035-4. URL http://dx.doi.org/10.1016/B978-0-444-81811-9.50035-4.

V Bertola and E Cafaro. Slug Frequency Measurement Techniques in Horizontal Gas-Liquid Flow. *AIAA Journal*, 40(5):1010–1012, may 2002. ISSN 0001-1452. doi: 10.2514/2.1742. URL https://doi.org/10.2514/2.1742.

M. Fossa, G. Guglielmini, and A. Marchitto. Intermittent flow parameters from void fraction analysis. *Flow Measurement and Instrumentation*, 14 (4-5):161–168, 2003. ISSN 09555986. doi: 10.1016/S0955-5986(03)00021-9.

Xin Wang, Liejin Guo, and Ximin Zhang. An experimental study of the statistical parameters of gas-liquid two-phase slug flow in horizontal pipeline. *International Journal of Heat and Mass Transfer*, 50(11-12):2439–2443, 2007. ISSN 00179310. doi: 10.1016/j.ijheatmasstransfer.2006.12.011.

R J Wilkens and D K Thomas. A Simple Technique for Determining Slug Frequency Using Differential Pressure. *Journal of Energy Resources Technology*, 130(1), jan 2008. ISSN 0195-0738. doi: 10.1115/1.2824297. URL https://doi.org/10.1115/1.2824297.

Jignesh Thaker and Jyotirmay Banerjee. Characterization of two-phase slug flow sub-regimes using flow visualization. *Journal of Petroleum Science and Engineering*, 135:561–576, 2015. ISSN 09204105. doi: 10.1016/j.petrol.2015.10.018. URL http://dx.doi.org/10.1016/j.petrol.2015.10.018.

Jignesh Thaker and Jyotirmay Banerjee. Influence of intermittent flow sub-patterns on erosion-corrosion in horizontal pipe. *Journal of Petroleum Science and Engineering*, 145:298–320, 2016b. ISSN 09204105. doi: 10.1016/j.petrol.2016.05.006. URL http://dx.doi.org/10.1016/j.petrol.2016.05.006.

A. Archibong-Eso, Y. Baba, A. Aliyu, Y. Zhao, W. Yan, and H. Yeung. On slug frequency in concurrent high viscosity liquid and gas flow. *Journal of Petroleum Science and Engineering*, 163(September 2017):600–610, 2018. ISSN 09204105. doi: 10.1016/j.petrol.2017.12.071. URL https://doi.org/10.1016/j.petrol.2017.12.071.

Fayez M. Al-Alweet, Artur J. Jaworski, Yusif A. Alghamdi, Zeyad Almutairi, and Jerzy Kołłątaj. Systematic frequency and statistical analysis approach to identify different gas-liquid flow patterns using two electrodes capacitance sensor: Experimental evaluations. *Energies*, 13(11), 2020. ISSN 19961073. doi: 10.3390/en13112932.

A. Arabi, Y. Salhi, Y. Zenati, E. K. Si-Ahmed, and J. Legrand. On gas-liquid intermittent flow in a horizontal pipe: Influence of sub-regime on slug frequency. *Chemical Engineering Science*, 211:115251, 2020a. ISSN 00092509. doi: 10.1016/j.ces.2019.115251. URL https://doi.org/10.1016/j.ces.2019.115251.

Abderraouf Arabi, Karim Ragui, Yacine Salhi, and Abdelkader Filali. Slug frequency for a gas-liquid plug flow: Review and development of a new correlation. *International Communications in Heat and Mass Transfer*, 118:104841, 2020b. ISSN 07351933. doi: 10.1016/j.icheatmasstransfer.2020.104841. URL https://doi.org/10.1016/j.icheatmasstransfer.2020.104841.

Chapter 7

Conclusions

The proposed LESLIE flow loop, a new experimental facility, was designed and set up for the analysis of multiphase flows, including mixtures of gas, liquid and solid phases. Instrumentation equipment for measuring the relevant parameters of multiphase flows were included, such as the flow regime, frictional pressure gradient and void fraction. For this reason, LESLIE turns out to be a very useful and reliable tool to measure and integrate all relevant parameters into a unified working model, that will both serve as a validation or benchmark reference for numerical models, and as a valuable tool in design processes of multiphase facilities.

Once the facility was assembled, tests were carried out to verify the overall precision of the measurements. In this sense, one-phase measurements have been made to calculate the FPG of water inside pipelines, where the pressure loss curve has been reproduced. Measurements have also been made for air-water two-phase flows in order to compare them with results and correlations available in the literature, and in all cases a great deal of agreement has been verified, even considering the oscillations presented by the measurements due to the very random nature of multiphase flows. Thus, it is concluded that very reliable and useful results can be obtained and applied both for the design of facilities and for characterizing multiphase flows.

In order to characterize GL two-phase flows, several measurements were performed, including capturing the movement of the flow with a high speed camera, so as to identify the flow regimes. Also, differential and gauge pressures, void fraction, droplet distributions and slug frequency were precisely measured and correlated through the use of specific measuring tools. Once

two phase regimes were studied, some specific experiments were run in order to measure the influence of the solid phase (GLS three-phase flows) over the frictional pressure drop, flow regimes and slug frequency and the results of those experiments were analyzed in relation to the results of two-phase flow experiments.

Three correlations for predicting the frictional pressure drop of two-phase flows were used and their respective performance was compared. It was found that the Lockhart and Martinelli correlation provides the best prediction rate with an average absolute percentage difference (AAPD) of 6.2 %. The modified Lockhart-Martinelli correlation, incorporating the SRC Pipe Flow model for slurries (Gillies et al. [2004]), was used for predicting the FPG of three-phase flows. Both correlations performed adequately as the predicted values of the pressure drop were generally in concordance with the experimental data. It has been noted that for solid concentrations of 5 and 10 % there is a rather small (almost null) effect on the pressure drop, and according to the theoretical model (modified LM) it is not expected to obtain meaningful increments in pressure drops until reaching more than 30 % of solid concentrations.

In order to predict the void fraction, several correlations were performed and compared, including the one-dimensional drift flux analysis, using correlations to the models proposed by some authors for calculating the drift flux parameters. It was found that the drift flux analysis tends to overestimate the predicted void fraction, obtaining similar results for different correlations. The best prediction was achieved by the Lockhart and Martinelli void fraction correlation, which is based on a two-fluid model approach.

The flow regimes for 62 different test conditions were thoroughly analysed by capturing high speed camera videos, so as to be able to identify the transition boundary between plug and slug flows regimes. The transition for two-phase flow matched quite well with the flow regime map proposed by Kong and Kim [2017], and also a strong dependency of the boundary with the solid concentration was found for three-phase flows. Due to the accumulation of solid particles in the tail of Taylor bubbles, higher shear stresses are required to detach small bubbles. Thus, for a specific slurry velocity (j_{fs}), higher flow rates of the gas phase are needed to reach the plug-to-slug transition when solid concentration increases.

In a similar way, the influence of the solid phase on the slug frequency was also analysed. Initially, two-phase flow slug frequencies were measured,

and correlations with available literature were tested. A wide spectrum of behaviours were found, where some correlations overestimate significantly the slug frequency while others underestimate it. Good predictions were obtained with the Thaker and Banerjee correlation, who relates the mixture Strouhal number (St_M) to the input liquid fraction λ_f. However, when trying to fit the experimental data to collapsing curves, the best performance was found when relating the gas Strouhal number (St_g) with the input liquid fraction. Finally, it was found that increasing the solid concentration induces a slight decrease in slug frequency. Which could be explained for the accumulation of solid particles in the tail of the elongated bubbles, and its obstruction on the detachment of bubbles.

Although some rather interesting results have been obtained when adding polypropylene particles, in order to make firm conclusions it is necessary to have measurements carried out when dealing with a wider range of solids. For example, new experiments could explore the consequences of involving in the flow solids of different densities or sizes, and also covering a greater range of concentrations. In this way, correlations could be obtained that take into account the effect of solid particles. So the proposed experimental rig could be used to analyse a more diverse group of interactions, using the same systems and theoretical tools, opening the door for new researchers to widen the field in the future. Furthermore, the use of the same techniques in the vertical test sections already implemented in the facility, could offer great opportunities to enrich the scope of the research, adding new variables that can be found in real industrial contexts.

7.1. Bibliography

R.W. Lockhart and R.C. Martinelli. Proposed correlation of data for isothermal two-phase, two-component flow in pipes. *Chemical Engineering Progress*, 45(1):39–48, 1949. ISSN 03607275. doi: http://dx.doi.org/10.1016/0017-9310(67)90047-6.

R. G. Gillies, C. A. Shook, and J. Xu. Modelling Heterogeneous Slurry Flows at High Velocities. *Canadian Journal of Chemical Engineering*, 82(October): 1060–1065, 2004. ISSN 00084034. doi: 10.1002/cjce.5450820523.

Ran Kong and Seungjin Kim. Characterization of horizontal air–water two-

phase flow. *Nuclear Engineering and Design*, 312:266–276, 2017. ISSN 00295493. doi: 10.1016/j.nucengdes.2016.06.016. URL http://dx.doi.org/10.1016/j.nucengdes.2016.06.016.

Jignesh Thaker and Jyotirmay Banerjee. On intermittent flow characteristics of gas–liquid two-phase flow. *Nuclear Engineering and Design*, 310:363–377, 2016. ISSN 00295493. doi: 10.1016/j.nucengdes.2016.10.020. URL http://dx.doi.org/10.1016/j.nucengdes.2016.10.020.

APPENDICES

UNIVERSITAT ROVIRA I VIRGILI
EXPERIMENTAL ANALYSIS OF MULTIPHASE FLOWS. DESIGN AND SETUP OF AN EXPERIMENTAL FACILITY
Paolo Juan Sassi Arobba

Appendix A

Measurements Campaigns

A.1. First campaign

In this experimental campaign experiments for 25 test conditions are performed at LESLIE flow loop to verify that the measured data is consistent with the literature. The test condition for the 25 runs are summarized in table A.1.

As a first instance, the frictional pressure drop of 9 water one-phase flow rates are measured and compared with the Darcy-Weisbach equation, listed in table A.1 and identified as 1-phase in the "Flow Regime" column. Very good agreement is observed among the measurements, an average percent difference of $\pm$ 4.5 % is obtained. In fig. A.1 the measured data is plotted together with the Darcy-Weisbach curve for frictional pressure drop in an horizontal 30 mm ID smooth pipeline.

The two-phase flow analysis consists of 16 test conditions with measurements of frictional pressure drop, system pressure, void fraction and fast camera flow visualization.

To verify the complete development of the flow 5 pressure taps are used to measure pressure drop and plotted in fig. A.2. As it can be seen the last three measurements are almost perfectly aligned, as expected, and thus is concluded that the flow is completely developed in the test section. The increment of both water and gas flow rates, produces an increment on both the system pressure and the slope, this last being the frictional pressure drop. This shows that plug and slug flow regimes are not influenced by one phase, but the two phases contribute to the pressure change.

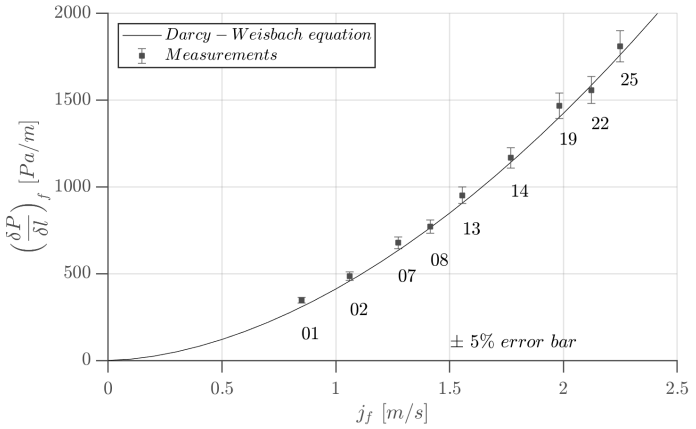

Figure A.1: Comparison of frictional pressure drop measured and calculated with Darcy-Weisbach equation

Table A.1: Data set # 1–Summary of experimental data

Run no.	$j_f[m/s]$	$j_g[m/s]$	Flow regime	$(dP/dz)_{fg}$ $[kPa/m]$	Void Fraction [-]
1	0.84	0	1-phase	-	-
2	1.06	0	1-phase	-	-
3	1.06	0.41	plug	0.74	0.17
4	1.06	0.86	slug	0.95	0.29
5	1.06	1.37	slug	1.15	0.34
6	1.06	1.98	slug	1.30	0.42
7	1.27	0	1-phase	-	-
8	1.41	0	1-phase	-	-
9	1.41	0.43	plug	1.18	0.09
10	1.41	0.88	slug	1.49	0.21
11	1.41	1.39	slug	1.65	0.28
12	1.41	2.05	slug	1.84	0.37
13	1.56	0	1-phase	-	-
14	1.77	0	1-phase	-	-
15	1.77	0.44	plug	1.71	0.07
16	1.77	0.95	slug	1.97	0.18
17	1.77	1.47	slug	2.30	0.20
18	1.77	2.10	slug	2.60	0.26
19	1.98	0	1-phase	-	-
20	1.77	2.11	slug	2.82	-
21	2.04	1.53	slug	2.87	-
22	2.12	0	1-phase	-	-
23	2.12	0.45	plug	2.23	0.04
24	2.12	1.00	slug	2.60	0.10
25	2.25	0	1-phase	-	-

The void fraction measurements are done by measuring the liquid volume fraction trapped between fast-closing ball valves. As the two phase flow in

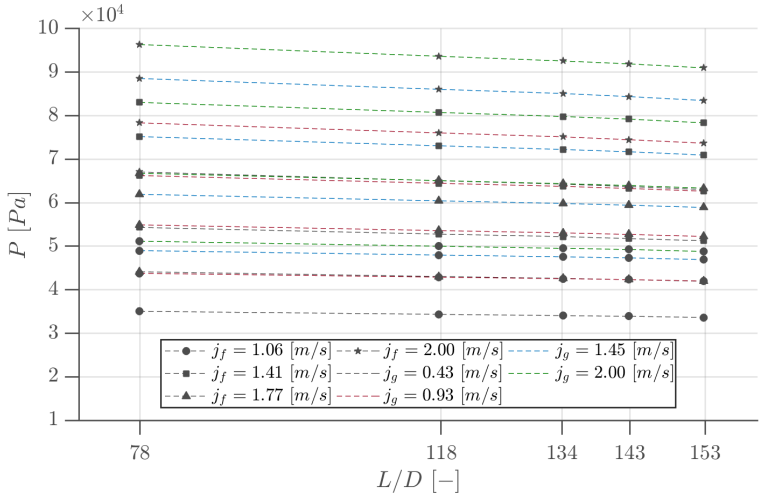

Figure A.2: Gauge pressure along the horizontal pipeline.

plug and slug flow regimes is not homogeneous, at least ten measurements are done for each test condition until a normal distribution of liquid hold-up is obtained. The mean value is then assigned as the void fraction of the test condition.

To identify the flow regime each test condition is visualized with the fast camera. The nose and tail of the long bubbles are analysed to determine if they correspond to plug or slug bubbles.

A.2. Second campaign

In order to ensure the accurate estimation of the average pressure at the corresponding sections, single-phase water flow measurements were performed and compared with the theoretical curve of the Darcy-Weisbach equation (eq. (A.1)). The Darcy-Weisbah friction factor, f, is calculated with the Colebrook-White relation (eq. (A.2)). fig. A.3 shows the comparison. The mean deviation of the twelve performed measurements is 4%.

$$\left(\frac{\delta P}{\delta z}\right)_f = f \cdot \frac{\rho}{2} \cdot \frac{j_f^2}{D} \tag{A.1}$$

$$\frac{1}{\sqrt{f}} = -2\log_{10}\left(\frac{k/D}{3,7} + \frac{2,51}{Re\sqrt{f}}\right) \tag{A.2}$$

A total of 134 test conditions were measured in the experimental facility.

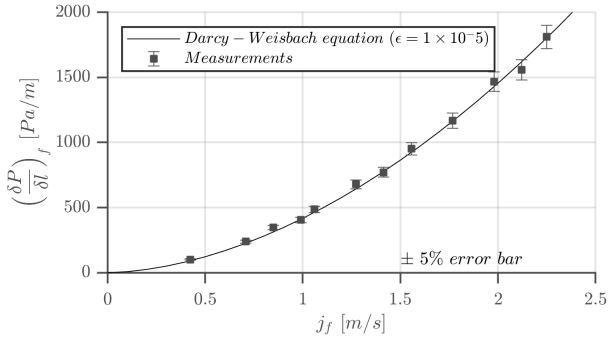

Figure A.3: Comparison of experimental frictional pressure gradient for water flow and Darcy-Weisbach theoretical curve with $\epsilon = 1.0 \times 10^{-5}$ m. (thermoplastics)

62 were specifically chosen to analyse the transition between plug and slug flow regimes. Here, the gas and slurry velocities were set according to the flow visualization to determine precisely the flow transition. For the analysis of the FPG, 24 different operating conditions were selected for the three mixtures (two-phase and, 5% and 10% of solid loading), adding a total of 72 measurements. A summary of the performed measurements is shown in table A.2.

Table A.2: Data set # 2–Summary of experimental data

Objective	**Solid %**	$j_g[m/s]$	$j_{fs}[m/s]$	**# points**
Flow	2P	0.4 – 1.2	0.6 – 2	25
Transition	5 %	0.7 – 1.5	0.6 – 2	19
(Visualization)	10 %	0.7 – 1.5	0.6 – 2	18
Sub-total				62
		0.4		
		0.6	1	
		0.8	1.4	(3x6x3)
Frictional	2P	1.2	1.7	54
Pressure	5 %	1.4		
Gradient	10 %	2		
		2.5	1	(3x3x2)
		3.5	1.4	18
		4.5		
Sub-total				72
Total				**134**

A.3. Third campaing

In this experimental campaign measurements are reported for two and three-phase flows including plug and slug flow regimes with relatively high liquid superficial velocities (or slurry in the case of three-phase flows), which ranges from 0.85 to 2.5 m/s. The gas superficial velocity ranges between 0.5 and 4.0 m/s. The summary of the runs can be seen and compared with the regime map from fig. 3.17 in fig. A.4. 20 runs of two-phase flows are indicated with circle markers while three phase flows with 10% and 20% of volumetric solid loading are signaled with black X's and red crosses markers respectively. Note that equivalent sets have been used for two and three-phase flows with 10% of solid loading and only 12 runs are reported with 20% of loading (red crosses). Each flow regime is carefully identified using fast camera recordings and all of them are consistent with the flow regime map limits.

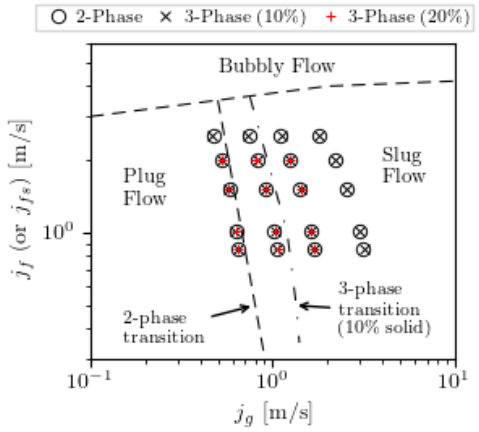

Figure A.4: Summary of experimental runs of dataset # 3 in the regime map.

The gas superficial velocity is calculated locally, at the test section, with eqs. (2.3) and (2.4).

A.3.1. Images for frequency calculation

Two batches of images were acquired for the 52 runs summarized in fig. A.4. The first batch consists of images with a resolution of (8×640) pixels in the axial and vertical directions respectively. 75 seconds of images were taken, for a total of 240,000 frames per run. Each image has been pre-processed with background subtraction and histogram stretching to enhance contrast. A time series image is made by placing one column of pixels from every pre-processed

image next-to each other. A schematic representation of the construction of the time series image for a two-phase flow is shown in fig. A.5. Two example frames (number 120 and 250) are shown in the top of the figure, one column of pixels (always at horizontal position 350) is taken from every frame and they are all grouped together into one large image (bottom image). This way, a $(240,000 \times 640)$ image is obtained where the vertical coordinate of the resulting image corresponds to the vertical axis of the pipe, and the horizontal axis is the evolution in time of the flow state as it passes through the selected cross section (during 75 seconds).

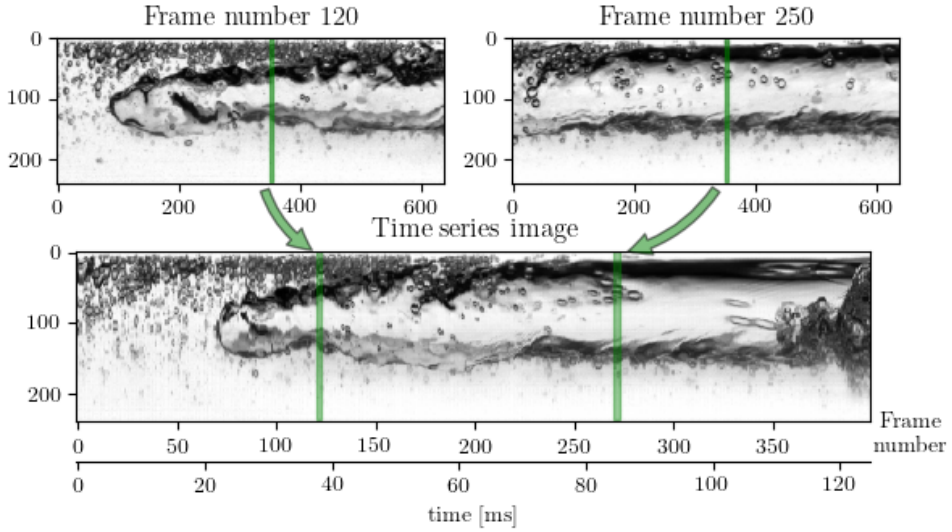

Figure A.5: Construction of time series image.

Note that the images acquired to perform the frequency analysis are very thin images (8x640 pixels). The full frames presented in fig. A.5 are example images to illustrate the process, but these images correspond to the ones described in the following sub-section.

A.3.2. Images for velocity and size calculation

In addition to the images described above, full resolution frames (640×320 pixels) were recorded in order to calculate the size and velocity of the elongated bubbles. With this resolution at 3,200 FPS a maximum of 17 seconds can be recorded, this implies 54,400 frames per run. Again, background subtraction and histogram stretching is performed, and the time series image is constructed to identify nose and tail locations.

A.3.3. Velocity sensitivity analysis

As digital images are made up of pixels, the distance between the black and red rectangles in fig. 6.3 (section 6.2.2) is measured in whole units of pixels. Therefore, the measure of displacement of the nose or tail of the bubble is obtained in a discrete domain. The sensitivity analysis of the nose and tail velocities as a function of the jump (number of frames between the two images) are presented in figs. A.6a and A.6b, respectively. The black dots indicate the velocity of the nose (or tail) calculated at the corresponding jump (x axis), and the blue dots indicate the correlation factor between the interrogation window and subsequent frames. As the jump increases the similarity between the original interrogation window and all subsequent frames decreases, so does the correlation factor (blue dots), as expected.

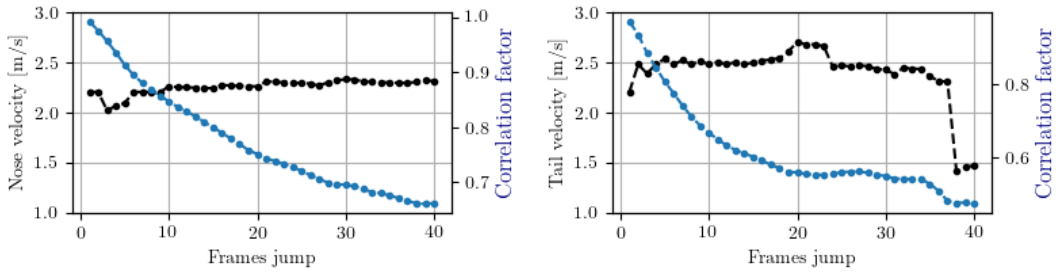

(a) Nose velocity. **(b)** Tail velocity.

Figure A.6: Sensitivity analysis of velocity calculation with cross-correlation between image n and $n + jump$. Two-phase run with $j_f = 1.0\ m/s$ and $j_g = 1.02\ m/s$ (same bubble than fig. 6.3)

For lower values of frame jumps (between 1 and 6) the velocities show some oscillations. This is expected, because the interrogation window is displaced one pixel at a time while the captured bubble is moving in real domain, and so in subsequent frames the displacement can actually correspond to fractions of pixels. In both images of fig. A.6, the velocity becomes quite stable at jumps of about 10 frames. However, for bigger jumps, of more than 20 frames, the bubbles may adopt shapes that are different than the one in the interrogation window and higher oscillations can be found, especially at the tail, where several bubbles get detached from the tail of the bubble and the shape may then vary significantly. Using a jump value of 10 frames, the velocity becomes quite stable, both at the nose and tail, with correlation factors of 0.85 and 0.66 respectively. The correlation factor for the tail images drops much faster than in the nose images. This is due to the presence of several drops detaching

from the tail, which changes the shapes in the image more rapidly.

A.3.3.1. Validation and pixel calibration

Furthermore, the images for the velocity analysis were taken with a ruler attached to the pipe. This allows to calibrate the pixel size, and to manually compare the velocity calculations using the automated algorithm. fig. A.7 shows two images taken with the ruler attached to the pipe as a reference.

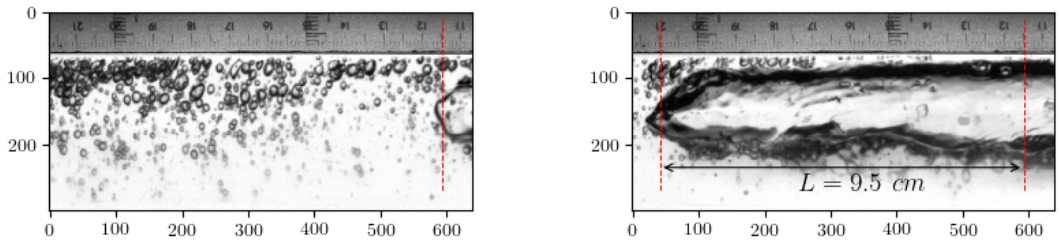

(a) **(b)**

Figure A.7: Pixel calibration and pixel size measurement. Two-phase run with $j_f = 1.0\ m/s$ and $j_g = 1.02\ m/s$ (same bubble than fig. 6.3), flowing from right to left.

In fig. A.7a the axial position of the nose of an elongated bubble is marked with a red dashed line at 11.5 cm in the ruler. In fig. A.7b the same bubble is marked 133 frames later at 21 cm in the ruler. This way it is possible to calculate the velocity of the nose with eqs. (A.3) and (A.4) where Δx represents the distance between the red lines in meters, measured with the ruler. The velocity obtained applying the algorithm for the corresponding nose is 2.26 m/s, with a relative error of about 6%.

$$\Delta t = \frac{N_{frames}}{FPS} = \frac{126}{3200} \tag{A.3}$$

$$V_{nose} = \frac{\Delta x}{\Delta t} = \frac{0.095}{0.0394} = 2.41 m/s \tag{A.4}$$

This calculation has been done manually for several noses and tails chosen at random, and the average relative error is about 5 %.

In order to establish the pixel size, the quotient between the amount of pixels between the red lines (551) and the corresponding distance (0.095 m) is calculated, obtaining a pixel size of 0.1724 mm/px. This is calculated for

every setting of the camera, whose position may vary a few millimetres between measurements.

Appendix B

Statistical parameters

To evaluate the performance of the different correlations three statistical parameters are used and defined in this section. The averaged percentage difference (APD) between the predicted and measured frictional pressure gradient is defined in eq. (B.1), but it is also applicable to others parameters.

$$APD = \frac{1}{n}\sum_{k=1}^{n}\left[\frac{(\delta p/\delta z)_{gf,pred} - (\delta p/\delta z)_{gf,\exp}}{(\delta p/\delta z)_{gf,exp}}\right] \times 100 \tag{B.1}$$

With eq. (B.1) the over-estimated and under-estimated can be cancelled out, thus, the average percentage difference is divided into APD(+%) and APD(-%) for over and under estimated predictions respectively. Together with the APD, the averaged absolute percentage difference (AAPD) and the root mean square porcentage difference (RMSPD), are also used, defined by eqs. (B.2) and (B.3).

$$AAPD = \frac{1}{n}\sum_{k=1}^{n}\left|\frac{(\delta p/\delta z)_{gf,pred} - (\delta p/\delta z)_{gf,exp}}{(\delta p/\delta z)_{gf,exp}}\right| \times 100 \tag{B.2}$$

$$RMSPD = \sqrt{\frac{1}{n}\sum_{k=1}^{n}\left[\frac{(\delta p/\delta z)_{gf,pred} - (\delta p/\delta z)_{gf,exp}}{(\delta p/\delta z) f_{gf,exp}}\right]^2} \times 100 \tag{B.3}$$

Appendix C

Image processing algorithm for droplet size distribution of annular flows

In this section an image processing algorithm to calculate size distribution of droplets travelling in the gas core of annular flows is presented. The algorithm is written in Python using the scikit-image package library, it essentially consists of three steps. In appendix C.1 the pre-processing of the images in order to enhance image information is described. Then, the object identification algorithm together with the control parameters is described in sub-section C.2, here two object detectors were tested and are compared. Finally in appendix C.3 the calculation of the equivalent diameter of the drops is presented.

C.1. Pre-processing

Because the images are square and the visualization rod is circular (fig. C.1a), the first step of the pre-processing is to create a mask of the region of interest (ROI), to avoid unnecessary effort outside this region, which is completely dark. As there are 8000 images for each batch, a mean image is calculated from the top 5% brighter images, see fig. C.1b. Then, the brighter pixels are identified above certain threshold (fig. C.1c), determined using the triangle algorithm, already included in the library (Zack et al. [1977]). Finally a 95% confidence ellipse of the bright pixels is calculated and the mask is done

from this ellipse, fig. C.1d.

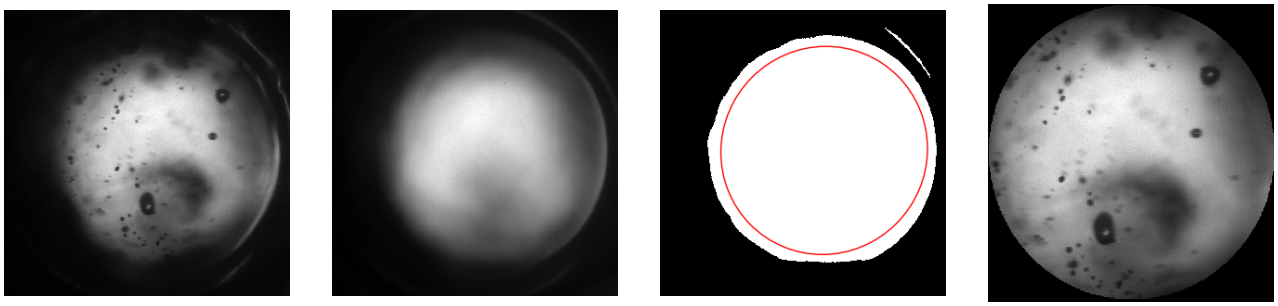

(a) Example frame - raw (640 × 640 pixels).

(b) Mean image from 5% brighter frames.

(c) Confidence ellipse of bright pixels.

(d) Masked frame (456 × 472).

Figure C.1: Masking process

Although the flow regime from the configurations described in the previous sections are all air-water annular flow, their topology change between the different configurations. Furthermore, although the images have been taken with the same measurement port, camera, lenses and lighting equipment, and also using the same three focus planes (α, β and γ), when changing between configurations it is necessary to disassemble and reassemble certain parts of the facility. This implies that the lighting and its distortions may change between the different operating conditions tested, this is, between different batches of images. So, the pre-processing algorithm is applied at one batch at a time.

Due to the deposition of drops in the visualization rod (as explained in section 3.2.2), waves higher than the rod, or even waves created because of the intrusiveness of the measurement technique, some of the obtained images are completely dark or contain some very big structures that do not allow the drops to be seen. Therefore, these ones should be discarded, as no drops can be distinguish in them. For comparable results across settings, the 1000 darkest images in each batch are discarded. Next, in order to facilitate the automated drop detection, background subtraction and histogram stretching are performed for each batch separately. In the next steps the pre-processing algorithm is described, where k is the index for the number of image in the batch, m and n are the number of pixels in the vertical and horizontal direction of the image, with the corresponding indexes i and j respectively.

1. Calculate mean gray value of every image of the batch.

$$\hat{I}_k = \frac{\sum_{i=1}^{m}\sum_{j=1}^{n} I_k(i,j)}{m \cdot n} \tag{C.1}$$

2. Generate $\bar{I}^*$, mean image from 5% brighter images.

$$\bar{I}^*(i,j) = \sum_{k_b} I_{k_b}(i,j) \tag{C.2}$$

Here k_b is the index for the number of images belonging to the top 5% brighter images. Note that brighter images are those with fewer liquid structures, therefore light distortion and background effects (to be subtracted) are more visible in these images.

3. Adjust average brightness based on $\bar{I}*$ (mean image).

$$N = max(\bar{I}^*) \,/\, 255 \tag{C.3}$$

4. Divide every image by the adjusted mean image and normalize the intensity.

$$I_k^* = I_k \,/\, \bar{I}^* \cdot N \tag{C.4}$$

5. Expand and displace the histogram. Here the contrast between drops and background is enhanced with the vector c_{lim}.

$$I_{pp} = \frac{I_k^* - c_1}{c_2 - c_1} \cdot 255 \tag{C.5}$$

$$I_{pp}(I_{pp} < 0) = 0 \tag{C.6}$$

$$I_{pp}(I_{pp} > 255) = 255 \tag{C.7}$$

As there are images with very different intensity profiles, using fixed parameters would be suitable for some images but would displace or expand too much the rest of the images. For this reason a first approach is calculated with minimum and maximum value of the image to be processed.

- $c_{lim} = [c_1, c_2] = [min(I_k), max(I_k)] \,/\, 255$

Note that a positive c_1 displaces the histogram to the left (darker image) and the difference expand the histogram if $c_2 - c_1 < 1$. If the resultant image has too much clipping the parameters are adjusted, either to displace or contract the histogram, in order to keep the majority of pixels inside the 8-bit range.

Raw images have quite compact gray-scale histograms, see fig. C.2. Pixels

are not scattered along the full scale of the 8-bit image. This show that the contrast between the drops and the background can be enhanced, which would save resources during the drop detection.

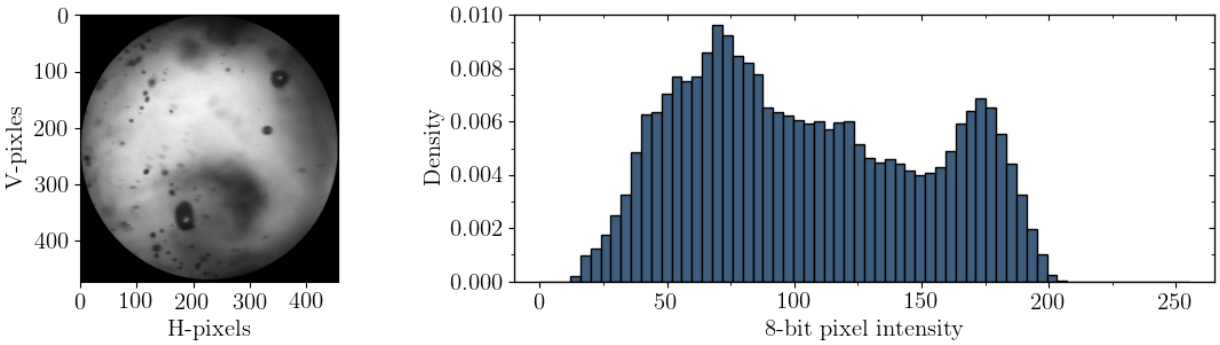

(a) **(b)**

Figure C.2: Raw image masked (a) and its corresponding histogram of pixel intensity inside the mask (b).

Once applied the pre-processing, the images have no background, the light is balanced in the focus plane and the drops are high in contrast, which facilitates the object detection in the following steps. Fig. C.3 shows a pre-processed image (C.3a) with its corresponding histogram of gray values (C.3b). It can be seen how the majority of the pixels are displaced to the right (bright pixels), which correspond to the background, and the whole scale of the image is now occupied by the pixels. Pixels on the left side correspond to drops in the focus plane, which are high in contrast. Pixels belonging to liquid structures away from the focus plane remain scattered across the center of the scale (gray shadows).

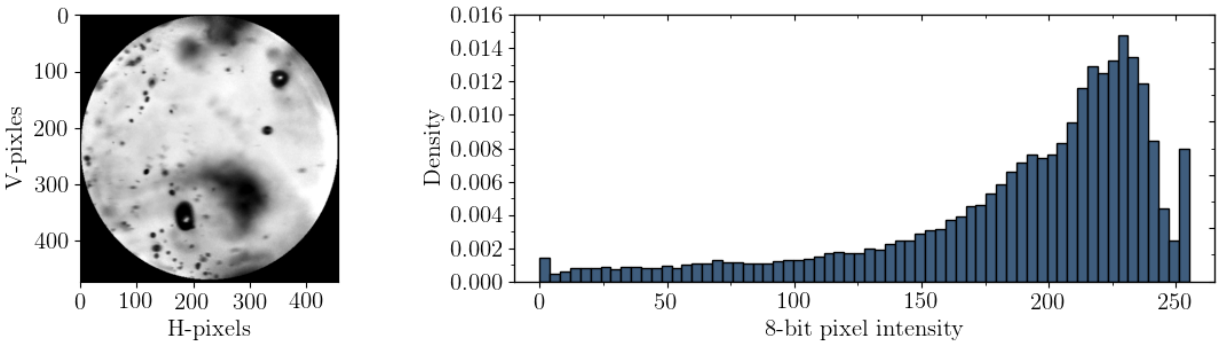

(a) **(b)**

Figure C.3: Pre-processed image masked (a) and its corresponding histogram of pixel intensity inside the mask (b).

C.2. Object detection

The algorithm for detecting the drops in the gas core starts with the Canny edge detector applied to the pre-processed images, [Canny, 1986]. The output image is, as explained above, a binary image with one-pixel wide edges, where pixels with a value of one correspond to edges. Several steps complete the algorithm to finally obtain a binary image where zeros correspond to the background pixels (black) and ones to pixels belonging to a drop (white). The complete algorithm consist of the following steps:

1. Apply Canny edge detector, fig. C.4b. Here the low and high thresholds are chosen to be relative small values, in order to identify several objects, even with low gradient values. The objects identified in this first instance, will then be subjected to further analysis where they will be reclassified (steps 3, 5, 6 and 7).
2. Closing contours. If drops do not have enough gradient at the edges, contours might not be closed contours. The closing is performed using a (3×3) kernel. A bigger kernel will close more contours, but it will also merge separate drops.
3. Clear border. Objects that are touching the edges are discarded.
4. Fill holes, fig. C.4c. Closed contours in the binary image are filled.
5. Remove remaining noise, this is edges that do not belong to closed contours and very small objects (one-pixel width elements).
6. Remove bright spots. Due to accumulation of drops or the presence of waves above the observation rod, sections of the bright background shows up in between dark areas and are identified as closed contours.
7. Apply thresholds, fig. C.4d.
   - Solidity threshold. Very concave objects are discarded.
   - Eccentricity threshold. Used to discard long filaments.
   - Mean intensity threshold. Identified objects with higher mean intensity than the threshold are discarded. These are out of focus drops whose size may be very distorted.

In fig. C.4 a summary of the drop detection process is illustrated. fig. C.4a is an example of a pre-processed image, fig. C.4b is the output of applying the canny edge detector to the pre-processed image. In fig. C.4c the closed

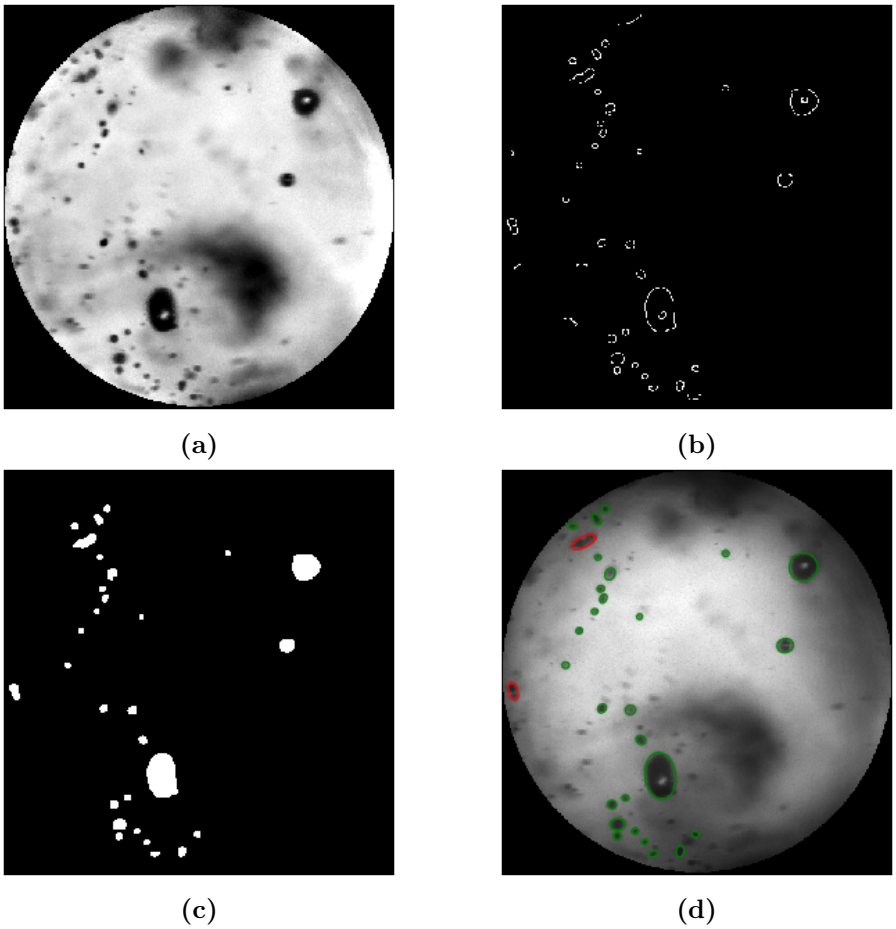

Figure C.4: Droplet identification process.

contours are filled and the noise is discarded, here only possible drops are identified with white pixels. However, there might also be unsought elements as out of focus drops, overlapping drops, bright spots or filaments and other fluid structures. So, additional classifications must be performed to discard such elements. In fig. C.4d correspond to the raw image where the edges of the elements from fig. C.4c are coloured in green if correspond to a desirable drop, or red if it has been discarded in steps 6 and 7 of the algorithm.

C.3. Equivalent sphere diameter

The size of the drops is represented with the equivalent sphere diameter. It is calculated as proposed by Ziegenhein and Lucas [2017]. For this, the volume of the drop is calculated and then the diameter is determined as if the volume corresponds to a perfect sphere. First, the major axis is defined

as the longest distance between two points of the projected object, and then the minor axis is defined as the longest distance perpendicular to the major axis. fig. C.5a shows an identified droplet with the major and minor axes draw as slashed lines, where C_0 is the centroid of the droplet. Then the droplet is divided in two across the minor axis, see fig. C.5b. A_1 and A_2 are the areas of the white and the gray areas respectively, C_1 and C_2 are the corresponding centroids, and Δl_1 and Δl_2 are the distances from the centroids to the minor axis. Finally, the droplet volume (V_d) is calculated by rotating each area 180 degrees around the minor axis, and the equivalent sphere diameter is inferred from its volume.

$$V_d = (A_1 \cdot \Delta l_1 + A_2 \cdot \Delta l_2)\pi \tag{C.8}$$

$$d_{eq} = 2\sqrt[3]{V_d \cdot 3/4 \cdot \pi} \tag{C.9}$$

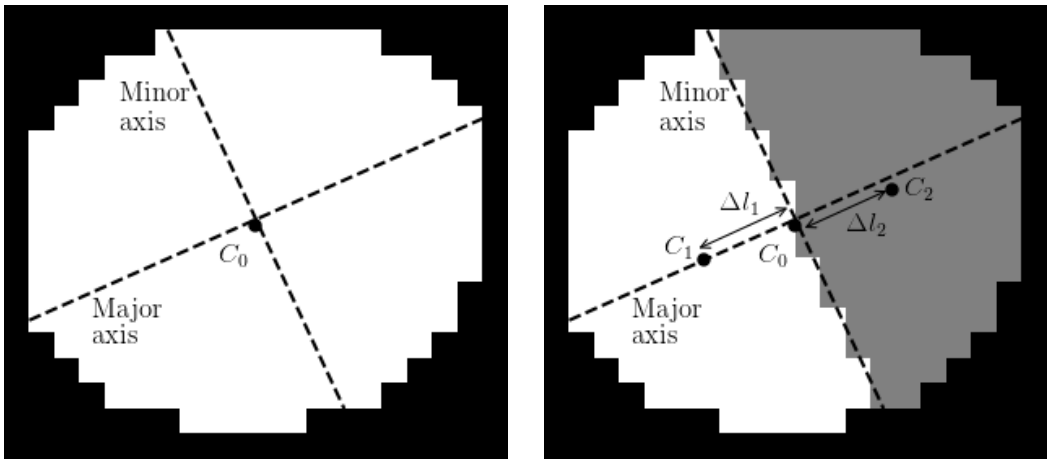

(a) **(b)**

Figure C.5: Identification of the parameters to calculate the equivalent sphere diameter of a droplet.

C.4. Validation

The validation of the measurement technique has been performed with a gas-solid two-phase flow in the same facility. Air was used as the gas phase and 50 micrometers particles were seeded into the airflow. Images of the particles were taken in the same conditions and processed with the same set of

parameters as for the annular flow images. fig. C.6 shows the size distribution of the captured particles.

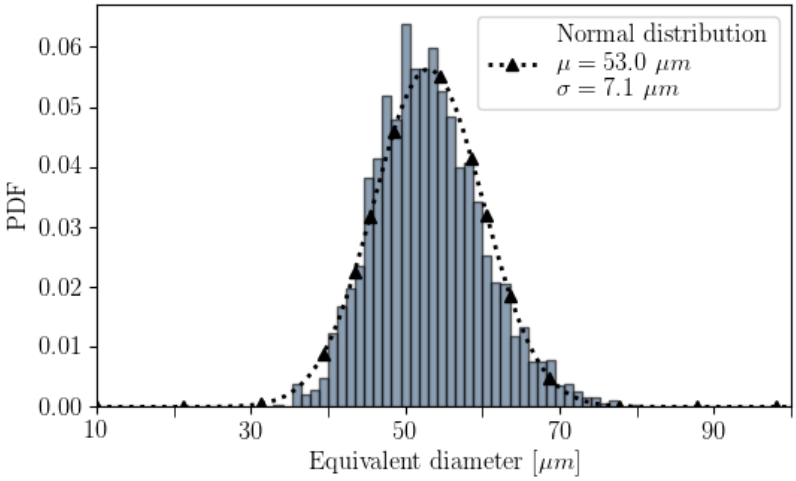

Figure C.6: Histogram and probability density function of particles size distribution.

A total of 3991 particles have been identified and analysed with the image processing technique in a series of 8000 images. Overlapped and out of focus particles were discarded. The seeded particles diameters are normally distributed with a mean value of 53 μm and a standard deviation of 7.1 μm. It can be notice that a 3 μm deviation towards larger diameters is obtained in the mean diameter. However, the slight divergence from the reference value is within the standard error, and is in a reasonable range, considered acceptable. It is also in concordance with the results from Bowen and Davies [1951], who stated that for the amount of measured particles (3991) an accuracy within 6% shall be expected.

The calibration of the pixel size was performed with a 1951 USAF resolution test chart. Images of the chart were obtained with the camera setting described in section 3.2.2.

C.5. Bibliography

G . W. Zack, W. E. Rogers, and S. A. Latt. Automatic Measurement of Sister Chromatid Exchange Frequency. *The Journal of Histochemistry and Cytochemistry*, 25(7):741–753, 1977.

John Canny. A Computational Approach to Edge Detection. *IEEE*

Transactions on Pattern Analysis and Machine Intelligence, PAMI-8(6): 679–698, 1986. ISSN 21627541. doi: 0162-8828/86/1100-0679$01.00.

T. Ziegenhein and D. Lucas. Observations on bubble shapes in bubble columns under different flow conditions. *Experimental Thermal and Fluid Science*, 85:248–256, 2017.

I. G. Bowen and G. P. Davies. Particle size distribution and the estimation of sauter mean diameter. In *Shell Technical Report No. ICT/28*, 1951.